



저작자표시-비영리-변경금지 2.0 대한민국

이용자는 아래의 조건을 따르는 경우에 한하여 자유롭게

- 이 저작물을 복제, 배포, 전송, 전시, 공연 및 방송할 수 있습니다.

다음과 같은 조건을 따라야 합니다:



저작자표시. 귀하는 원저작자를 표시하여야 합니다.



비영리. 귀하는 이 저작물을 영리 목적으로 이용할 수 없습니다.



변경금지. 귀하는 이 저작물을 개작, 변형 또는 가공할 수 없습니다.

- 귀하는, 이 저작물의 재이용이나 배포의 경우, 이 저작물에 적용된 이용허락조건을 명확하게 나타내어야 합니다.
- 저작권자로부터 별도의 허가를 받으면 이러한 조건들은 적용되지 않습니다.

저작권법에 따른 이용자의 권리는 위의 내용에 의하여 영향을 받지 않습니다.

이것은 [이용허락규약\(Legal Code\)](#)을 이해하기 쉽게 요약한 것입니다.

[Disclaimer](#)

이학박사 학위논문

**Studies on Magnon-Phonon Coupling in
HoMnO₃ and Cd₂Os₂O₇**

HoMnO₃ 와 Cd₂Os₂O₇ 에 대한 마그논-포논 결합
연구

2021 년 2 월

서울대학교 대학원

물리천문학부 물리학전공

김 태 훈

Studies on Magnon-Phonon Coupling in HoMnO₃ and Cd₂Os₂O₇

Taehun Kim

Supervised by
Professor Je-Geun Park

A Dissertation submitted to the Faculty of Seoul National
University in Partial Fulfillment of the Requirements for the
Degree of Doctor of Philosophy

February 2021

*Department of Physics and Astronomy
Graduate School
Seoul National University*

**Studies on Magnon-Phonon Coupling
in HoMnO₃ and Cd₂Os₂O₇**

HoMnO₃ 와 Cd₂Os₂O₇ 에 대한 마그논-포논 결합 연구

지도교수 박 제 근

이 논문을 이학박사 학위논문으로 제출함

2021 년 2 월

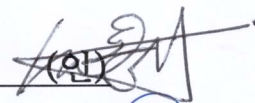
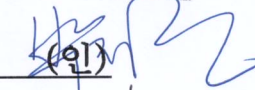
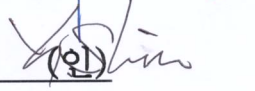


서울대학교 대학원

물리천문학부

김 태 훈

김태훈의 이학박사 학위논문을 인준함

2020 년 12 월

위원장	민 홍 기	(인) 
부위원장	박 제 근	(인) 
위원	신 용 일	(인) 
위원	김 도 현	(인) 
위원	Pengcheng Dai	(인) 

Abstract

Interactions between fundamental degrees of freedom in solids are essential in the modern condensed matter physics field. Since such interactions exist in most cases, it is crucial to determine the interaction mechanism's consequence. Spin-lattice coupling is a type of these interactions in which interactions occur between the spin and lattice degrees of freedom. Although it is an old concept already appearing in literature in the 1950s, a complete understanding of the spin-lattice coupling is still lacking.

For example, magnon–phonon coupling, the dynamical aspect of spin-lattice coupling, has been recently studied in hexagonal manganite and delafossite chromates by taking advantage of the state-of-the-art neutron and X-ray instruments. Both are noncollinear magnets with a triangular lattice. Because of the noncollinearity, the interaction between magnon and phonon or magnon is expected to exist theoretically. Although studies have successfully explained several features that arise from the couplings, they are limited to quantifying two different interactions. The inelastic neutron scattering study on HoMnO_3 can reveal the anomalous features in magnon dispersions and which is the dominant interaction. The simple linear spin-wave theory cannot reproduce the measured magnon spectra, the energy renormalization of overall magnons, and the unexpected dispersion shape. Using models including magnon–magnon interaction and magnon–phonon coupling, we can demonstrate that the dominant interaction in HoMnO_3 is the magnon–phonon coupling that originates through the exchange-striction mechanism.

The exchange-striction model is the usual candidate to explain the spin-lattice coupling that appeared in magnetic materials. However, unconventional spin-phonon (SP) coupling occurs in the $5d$ transition metal oxide $\text{Cd}_2\text{Os}_2\text{O}_7$. The phonons obtained by the infra-red optical spectroscopy study show that strong energy renormalization occurs through spin ordering. The main driving factor for the SP coupling has been known to be single-ion anisotropy. Since phonons measured by optical spectroscopy is limited to a long-wavelength limit, more comprehensive investigations of the phonons are highly desirable to shed light on the spin-phonon coupling. We studied the phonon mode and momentum dependence of the SP coupling using inelastic X-ray scattering experiments. Our first-principle calculations considering spin-orbit coupling (SOC) and noncollinear magnetic structure are in good agreement with the phonons at the coupled phase, suggesting that our theoretical model captures the SP coupling physics without invoking any other factors. By controlling the SOC strength, we can reproduce the observed phonon mode dependency and temperature dependence of the SP coupling. As a result, SOC is assumed to be the primary factor for SP coupling.

Keywords: spin-lattice coupling, magnon-phonon coupling, spin-phonon coupling, inelastic neutron scattering, inelastic x-ray scattering, hexagonal manganite, pyrochlore oxide.

Student Number: 2015-20325

Abstract	i
List of Tables	vi
List of Figures	vii
1 Introduction	1
1.1 Coupling between spin and lattice	1
1.1.1 Magnon-phonon coupling in a noncollinear magnet	2
1.1.2 Spin-phonon coupling in 5d transition metal oxide.....	7
1.2 Outline of the thesis	9
2 Theoretical backgrounds	14
2.1 Linear spin-wave theory	14
2.1.1 Spin Hamiltonian for triangular antiferromagnet	14
2.1.2 Holstein-Primakoff transformation	16
2.2 Magnon-magnon interaction	19
2.2.1 Three-magnon interaction term	20
2.3 Magnon-phonon coupling	23
2.3.1 Exchange-striction model	24
2.3.2 Einstein site phonon model	26
2.4 Phonon Hamiltonian	28

3	Experimental techniques	36
3.1	Inelastic neutron and X-ray scattering	36
3.1.1	Basic principles	37
3.1.2	INS experiment at 4SEASONS in J-PARC	40
3.1.3	IXS experiment at BL43LXU in SPring-8	45
 4	 Renormalization of spin-excitations in triangular lattice antiferromagnet	
	HoMnO₃	50
4.1	Hexagonal rare-earth manganites (<i>h</i> -RMnO ₃).....	50
4.1.1	An ideal platform to study noncollinear magnetism	51
4.1.2	Magnon-magnon interaction	53
4.1.3	Magnon-phonon coupling	54
4.2	Spin-excitations in HoMnO ₃	55
4.2.1	INS data and fitting by using LSWT	55
4.2.2	Anomalous features in magnon dispersion	57
4.3	Model fitting using quasiparticle interactions	59
4.3.1	XXZ+1/S expansion: magnon-magnon interaction	59
4.3.2	ESP model: magnon-phonon coupling	59
4.4	Discussion and summary	62
4.4.1	Dominant interaction in HoMnO ₃	62
4.4.2	Summary	64

5	Spin-orbit coupling effect on spin-phonon coupling in $\text{Cd}_2\text{Os}_2\text{O}_7$	67
5.1	<i>5d</i> pyrochlore oxide $\text{Cd}_2\text{Os}_2\text{O}_7$	67
5.1.1	Properties related to spin-orbit coupling	67
5.1.2	Unconventional spin-phonon coupling	70
5.2	IXS experiments and DFT calculations	71
5.2.1	Renormalization of phonons	71
5.2.2	SOC effect on the phonons	77
5.3	Discussion and summary	80
5.3.1	A common features of temperature and SOC effect	80
5.3.2	Summary	81
6	Summary and Outlook	85
6.1	Summary	85
6.2	Outlook	87
	Appendix:	90
	Publication lists	99
	국문 초록 (Abstract in Korean)	101
	감사의 글 (Acknowledgement)	104

List of Tables

2.1	Exchange-striction coefficients α for selected oxides	24
6.1	Summary table for the experimentally investigated triangular lattice antiferromagnet materials having magnon-phonon and magnon-magnon interaction	24
6.2	Summary table for spin Hamiltonian parameters and main mechanism of spin-phonon coupling for $5d$ transition metal oxides	24

List of Figures

1.1 Inelastic neutron scattering (INS) spectra for (Y, Lu)MnO₃. (a) A comparison between the observed spectra and calculated results from linear spin-wave theory. The red boxes denote the region where the anomalous features appear. (b) The INS spectra along the $\Gamma MM'$ direction. The top panel shows the full-width at half-maximum (FWHM) of the magnons and calculated decay rate from the magnon–phonon coupling Hamiltonian. The middle and bottom panels show the experimental data and calculations from the magnon–phonon coupling Hamiltonian, respectively. The left panel is for YMnO₃ and the right panel is for LuMnO₃. The figure is reprinted from [Ref. 1.15], adapted from [Ref. 1.12]

1.2 Mn positions x in the unit cell according to the neutron diffraction measurement. The figures are reprinted from [Ref. 1.9], and the data are adapted from [Ref. 1.8, Ref. 1.19]

2.1 The 120° ordering state in a triangular lattice

2.2 (a) The calculated magnon dispersion and (b) the decay rate for the triangular lattice with $S=1/2$. The dashed line indicates the LSWT calculation results, and the solid line indicates the results with $1/S$ corrections. The shaded area shows the width of the spectral peaks due to decay. (c) The shaded area is the region in which the decay process occurs. When the anisotropy Δ decreases, the decay region also shrinks. The calculated dynamical structure factor from the $1/S$ corrections are plotted in case of (d) $S=1/2$ and (e) $S=3/2$. The

figures are reprinted from [Ref. 2.14], adapted from [Ref. 2.7,Ref. 2.13]

2.3 Zero-field phase diagram of the triangular lattice calculated by the ESP model. Filled and empty circles mean the direction of the spins (up or down). The figure is adapted from [Ref. 2.44]

2.4 The calculated phonon dispersion relations of $\text{Cd}_2\text{Os}_2\text{O}_7$.

3.1 The magnetic form factor of Mn^{3+}

3.2 The schematics of the 4SEASONS spectrometer at J-PARC

3.3 The schematics for describing the time-of-flight neutron scattering method

3.4 ToF diagram explaining the RRM method adapted from [Ref. 3.4]

3.5 A photograph of the mounted HoMnO_3 sample at 4SEASONS

3.6 The Laue scattering patterns of HoMnO_3 . (Top) The [220] plane. (Bottom) The [002] plane

3.7 (Top) A schematic for the instrument. (Bottom) A photograph of the spectrometer arms, the analyzers, and the sample stage. The figure is adapted from [Ref. 3.7]

3.8 The measured Si (11 11 11) reflections at each detector, which describe the instrumental resolution of 1.5 meV

3.9 A photograph of (left) the sample stage and (right) the mounted sample. The surface of the sample shown in the figure is associated with the [1 1 1] plane. The size of the sample is $0.7 \times 0.45 \times 0.5 \text{ mm}^3$ with a mass of about 0.9 mg

3.10 The IXS data set of $\text{Cd}_2\text{Os}_2\text{O}_7$ measured at BL43LXU spectrometer

- 4.1 Magnetic structures in h -RMnO₃, adapted from [Ref. 4.2]
- 4.2 (a) Crystal and (b) magnetic structure of HoMnO₃. Open (filled) arrows indicate the ordered magnetic moment at $z = 0$ ($z = 0.5$) plane. x indicates the Mn position
- 4.3 INS data for HoMnO₃ taken at 4 K. The energy of the incident neutron is 30 meV. Three model calculations are presented to compare the experimental data. We used the Heisenberg model, and XXZ model with $1/S$ expansions, and the ESP model. (Details about models are described in the text) Black circles are fitted positions from INS spectra at each Q position. The inset indicates the Brillouin zones and the labels for the momentum positions
- 4.4 Comparing results between the simple Heisenberg model and the model adding (left) exchange anisotropy or (right) next nearest-neighbor exchange interactions. None of them explain the downward curvature along the AB direction
- 4.5 (Left) INS data taken at 4 K. The energy of the incident neutron is 60 meV. The momentum positions are the same as Fig. 4.3. The red box indicates the integration range for constant E cut. (Right) The integrated intensity of energy ranges from 24 to 26 meV
- 4.6 (Left) INS spectra along the AB direction. The calculated magnon energies using three different models are plotted. Blue circles indicate the fitted peak positions of each spectrum
- 4.7 (Left) INS spectrum at the B point and the calculated intensity using three different models. The gray shaded area indicates the fitted magnon peaks without background signals. (Right) The integrated intensity along the high symmetric path in momentum space. The calculated intensity from three models is compared with the experimental data

- 5.1 (a) The crystal and magnetic structures of $\text{Cd}_2\text{Os}_2\text{O}_7$. The arrows indicate the magnetic moment ordering. (b) The first Brillouin zone of the pyrochlore lattice.
- 5.2 (a) The photograph of the single crystal used in the IXS experiment. The white scale bar indicates a length of 100 μm . (b) The magnetic susceptibility of $\text{Cd}_2\text{Os}_2\text{O}_7$ single crystal as a function of temperature. (c) The single-crystal X-ray diffraction result for the $[HOL]$ plane.
- 5.3 (a–d) The IXS spectra taken at four Q positions as labeled. All spectra were obtained at 100 K. The black dashed line is the instrumental resolution profile of the elastic peak. (e) Phonon dispersions obtained using IXS and the DFT calculations. Red circles and squares represent the observed phonons from Raman and IR spectroscopies, adapted from [Ref. 5.13] and [Ref. 5.14].
- 5.4 (a, d) The IXS spectra taken at 282 and 100 K at $Q = W$ (6.50 6.00 7.00) and near K (6.60 5.95 6.60). The vertical bars under the spectra indicate the fitted peak positions. (b, e) The calculated IXS spectra that are based on DFT calculations by varying the strength of SOC. (c, f) The calculated IXS spectra that are based on the DFT calculations by varying U values.
- 5.5 (a) Energy renormalization of three IR-active phonons adapted from [Ref. 5.14]. The calculated energy renormalization for the three phonons from the DFT calculations matches the temperature dependence of three phonons simultaneously. (b) The nearly linear relationship between SOC and temperature obtained from the best fit in Fig. 5.5(a).

Chapter 1

Introduction

1.1 Coupling between spin and lattice

There are four fundamental degrees of freedom in solids—spin, lattice, charge, and orbital. The basic physical properties of a solid are determined by how these degrees of freedom work inside solids. Each degree of freedom has its distinct characteristic features; they can couple with each other and exhibit a distinct behavior that deviates from the normal states. One type of coupling that I will focus on in this thesis is the spin-lattice, sometimes called a magnon-phonon, coupling. The spin-lattice coupling usually appears when spins in magnetic materials order. The atomic positions change abruptly from their equilibrium positions resulting in different crystal symmetries or increasing/decreasing lattice constants. Consequently, lattice changes also induce changes in other properties such as ferroelectricity, resistivity, elastic constant, and thermal conductivity.

The spin-lattice coupling also appears in the form of magnon–phonon coupling. Magnons and phonons are the collective excitations of spin and lattice vibrations. They can get coupled to one another when they are close enough to interact in the momentum and energy space. As a result, the phonon and magnon energies are renormalized, or a new hybridized excitation (called electromagnon or magneto-elastic excitation) emerges. A lattice change is not necessary for the magnon–phonon coupling. The interaction strength and the energy difference between magnons and phonons are critical factors for the magnon-phonon coupling.

Although the magnon–phonon coupling concept has been developed since the 1950s by none other than C. Kittel in his seminal paper, it is still an important topic to study more. However, the full investigation of the coupling over a broader range of energy and momentum space is not yet done extensively. And the phase diagram for such coupling strength needs to be investigated experimentally. The phase diagram might be challenging to be confirmed experimentally because it is hard to control coupling strength as an external parameter, for example, pressure, magnetic field, or doping level. Nevertheless, it would be exciting to investigate such a phase diagram since several theories estimate a large change in ground state and excitations.

Throughout my thesis, I will discuss the change in magnons or phonons due to the magnon–phonon or spin–phonon coupling in two materials, hexagonal manganite HoMnO_3 and $5d$ pyrochlore oxide $\text{Cd}_2\text{Os}_2\text{O}_7$.

1.1.1 Magnon-phonon coupling in a noncollinear magnet

Magnons and phonons are quasiparticles that arise from magnetic and crystalline ordering in solids. Both obey the Bose-Einstein statistics; therefore, they are considered as bosons. The concept of magnon–phonon coupling was already studied in the 1950s by C. Kittel, who developed the theoretical treatment of magnon–phonon coupling in a ferromagnet [Ref. 1.1]. Many experimental observations and theoretical confirmations have since followed. For example, a gap opening between acoustic phonon and magnon due to the magnon–phonon coupling in iron halides, a collinear magnet, was examined in [Refs. 1.2–1.5]. The same physics in rare-earth metals was also examined by several

studies [Refs. 1.6 & 1.7].

Materials having a large spin-lattice coupling are expected to exhibit magnon–phonon coupling as well. One of the spin-lattice-coupled compounds, hexagonal manganite h - RMnO_3 [Refs. 1.8 & 1.9] can be a promising candidate to study the magnon–phonon coupling. The hexagonal manganites' multiferroic behavior indicates that the magnetic and ferroelectric ordering coexist in the same phase [Ref. 1.10]. This functionality is highly desirable for possible applications in magnetic memory and data-storage technologies.

From a fundamental viewpoint, magnon–phonon coupling is an important topic that enables us to understand how elementary quasiparticles interact and highlight features from the coupling. The recent works on hexagonal manganite h - RMnO_3 revealed several anomalous features arising from the magnon–phonon coupling [Ref. 1.11–Ref. 1.14]. J. Oh, et al. conducted an inelastic neutron scattering (INS) experiment to study magnons in (Y, Lu) MnO_3 and found some anomalies in magnon dispersion and magnon energies, as shown in Fig. 1.1 [Ref. 1.12].

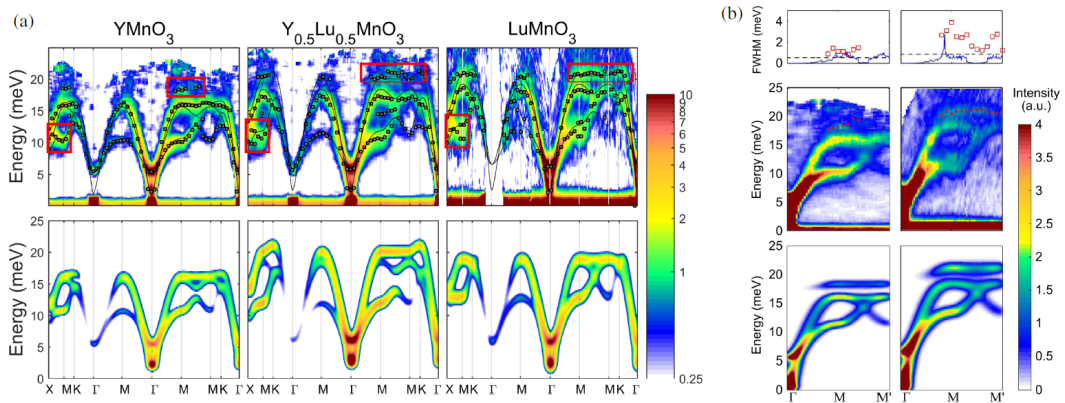


Figure 1.1 Inelastic neutron scattering (INS) spectra for (Y,Lu) MnO_3 . (a) A comparison between the observed spectra and calculated results from linear spin-

wave theory. The red boxes denote the region where the anomalous features appear. (b) The INS spectra along the $\Gamma MM'$ direction. The top panel shows the full-width at half-maximum (FWHM) of the magnons and calculated decay rate from the magnon–phonon coupling Hamiltonian. The middle and bottom panels show the experimental data and calculations from the magnon–phonon coupling Hamiltonian. The left panel is for YMnO_3 and the right panel is for LuMnO_3 . Part of the figures is reprinted from [Ref. 1.15] and adapted from [Ref. 1.12].

In their study, J. Oh, et al. found the negative slope of the magnon branch, which is not in agreement with the theoretical expectation from linear spin-wave theory (LSWT). Second, the lower magnon branch was found flattened at the M point. Third, they observed a non-negligible signal at an energy transfer of approximately 17 meV, which was also not predicted by the LSWT calculations. Finally, the broadening of magnon was much larger than that obtained experimentally; moreover, it is momentum-dependent. The simple Heisenberg model does not explain all the features within the LSWT formalism. Instead, adding a magnon–phonon coupling term to the spin Hamiltonian can explain those features. Subsequently, an additional mode at 17 meV was obtained and subsequently identified as a magneto-elastic excitation or an electromagnon. An electromagnon is a new hybridized quasiparticle that exhibits both magnon and phonon characteristics. This will be introduced in Chapters 2 and 4 later.

One of the primary conditions for this magnon–phonon coupling is a noncollinear magnetic structure. The hexagonal manganite has a 120° ordering state. In principle, this noncollinearity allows, otherwise forbidden, a linear coupling between the one-magnon

operator and the phonon operators in the magnon–phonon coupling Hamiltonian. This will be discussed in detail in Chap. 2. Some delafossite $ACrO_2$ compounds [Refs. 1.16 & 1.17] have features similar to those of the hexagonal manganite. This compound also has a nearly 120° ordering state with a helix structure. The similar features found in both compounds are as follows: (1) magneto-elastic excitations and (2) local minimum at the M point is observed in both inelastic neutron and X-ray scattering experiments. Interestingly, the magneto-elastic excitations in $YMnO_3$ [Ref. 1.14] and $LiCrO_2$ [Ref. 1.16] was observed by the inelastic X-ray scattering (IXS). Since the IXS cannot detect magnetic signals, observing magneto-elastic excitations through IXS provides evidence of duality in the magneto-elastic excitations.

Although the studies on magnon–phonon coupling in hexagonal manganite are well established, there is a limitation in obtaining a perfect triangular lattice in $(Y, Lu)MnO_3$ because of the trimerization problem [Refs. 1.9 & 1.18], which makes it difficult to compare experimental data and theoretical calculations directly. In contrast, $HoMnO_3$ provides an ideal platform to study this topic because it forms a nearly perfect triangular lattice at low temperatures. According to the neutron diffraction measurements [Refs. 1.8 & 1.19], the Mn position x of $HoMnO_3$ is almost $1/3$, as shown in Fig. 1.2.

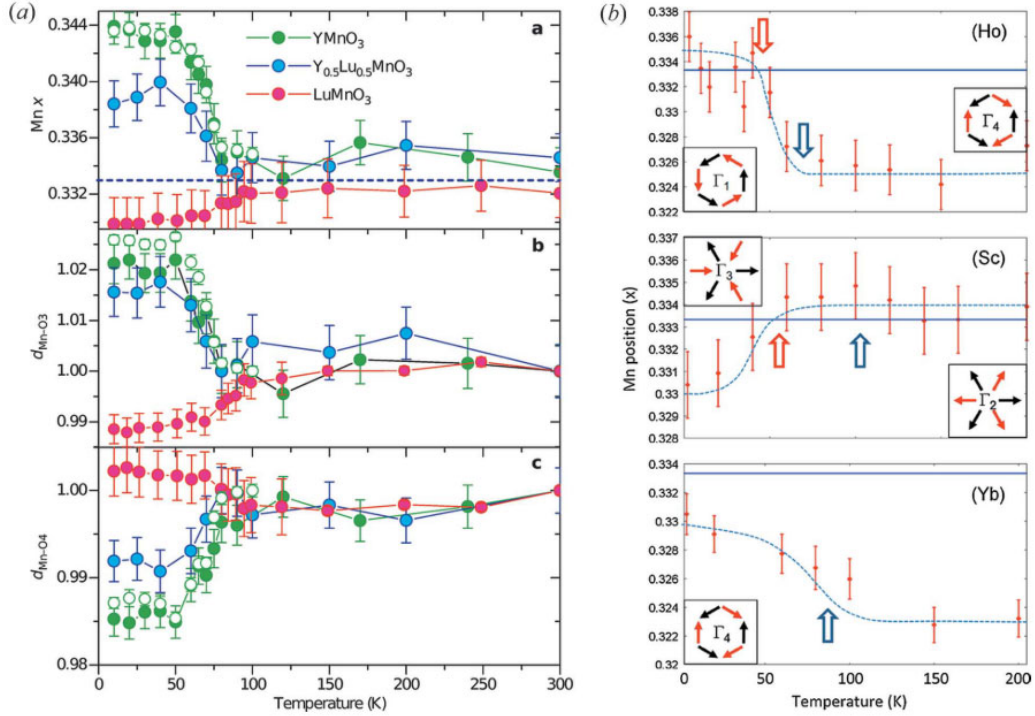


Figure 1.2 Mn positions x in the unit cell according to the neutron diffraction measurement. The figures are reprinted from [Ref. 1.9], and the data are adapted from [Refs. 1.8 & 1.19].

A direct comparison between theory and experiment is desirable in HoMnO_3 . Therefore, we conducted an INS experiment to measure the magnons in HoMnO_3 . Moreover, based on the magnon broadening observed in LuMnO_3 [Refs. 1.11 & 1.12], magnon–magnon interactions (or higher-order interactions) are expected to exist in hexagonal manganites. Therefore, we could quantify magnon's strength–phonon coupling and magnon–magnon interaction in HoMnO_3 . The study on HoMnO_3 has been discussed later in Chap. 4.

1.1.2 Spin-phonon coupling in 5d transition metal oxide

The primary mechanism of magnon–phonon coupling in hexagonal manganites is the exchange-striction model. The basic description of this model is that the modulation of atomic positions perturbs the exchange interaction between magnetic atoms. Some works suggest different mechanisms, such as single-ion anisotropy [Refs. 1.2, 1.20–1.22] or Dzyaloshinskii-Moriya (DM) interaction [Ref. 1.23]. Both the single-ion anisotropy and the DM interaction are originated from the spin-orbit coupling in the magnetic materials. So, the main mechanism of spin-phonon (SP) coupling in 5d transition metal oxide is considered as strong spin-orbit coupling.

One of the examples for spin-orbit coupling induced SP coupling was discovered in 5d transition metal oxides $\text{Cd}_2\text{Os}_2\text{O}_7$. In $\text{Cd}_2\text{Os}_2\text{O}_7$, the phonon energy changes abruptly during spin ordering at $T_N = 227$ K, as shown in Fig. 1.3 [Ref. 1.24]. It is explained not just by the temperature effect, such as the Grüneisen parameter. C. H. Sohn et al. found that the main origin of this phonon change is large single-ion anisotropy. They also mentioned that the modulation of atomic positions induces a change in the crystal field around the OsO_6 octahedra and renormalizes phonons. Therefore, one could think that a strong SOC is important to explain the observed SP coupling mechanism in $\text{Cd}_2\text{Os}_2\text{O}_7$ because a large SOC affects the anisotropy in a material.

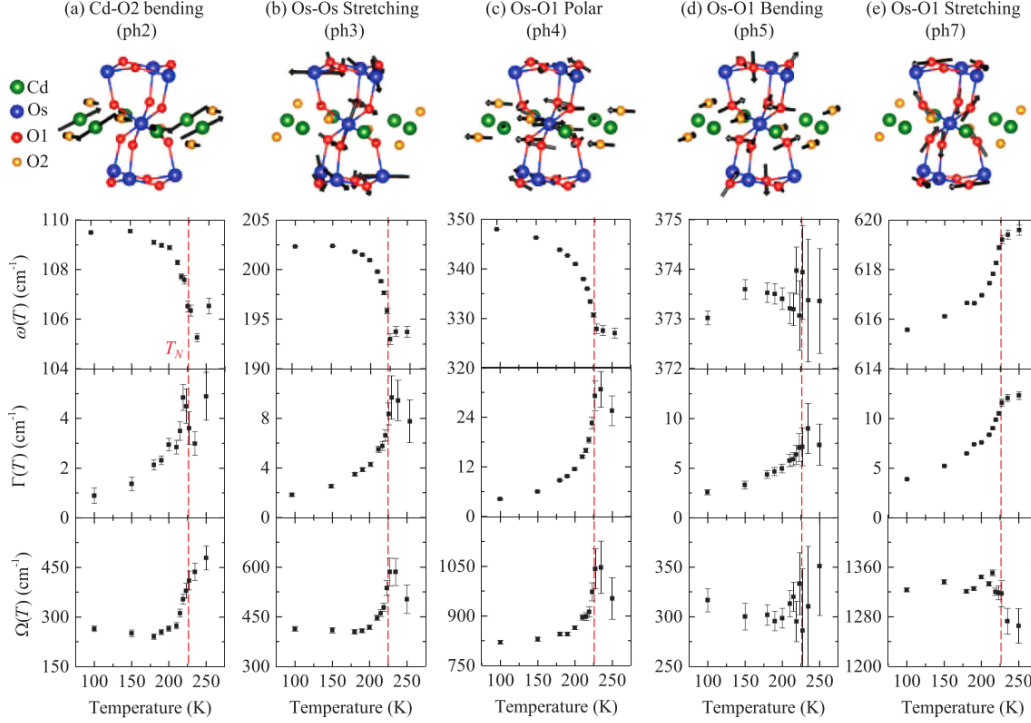


Figure 1.3 Infra-red optical spectroscopy results on $\text{Cd}_2\text{Os}_2\text{O}_7$. The temperature dependence of the phonon energy $\omega(T)$, linewidth $\Gamma(T)$, and phonon plasma frequency $\Omega(T)$ are shown. The figure is adapted from [Ref. 1.24].

$\text{Cd}_2\text{Os}_2\text{O}_7$ also exhibits another exciting property, metal-insulator transition (MIT). A. W. Sleight et al. reported MIT in 1974 [Ref. 1.25], and many researchers since then have attempted to understand MIT's mechanism. It was first suggested that the primary mechanism should be Slater-type transition [Ref. 1.26]. After some debates, peoples' opinions narrowed down to Lifshitz-type transition [Ref. 1.27]. Interestingly, this MIT occurs at the same temperature as magnetic ordering, $T_{\text{MIT}} = 227$ K. Therefore, the possibility of electron-phonon coupling exists. This issue was already considered in a

previous infra-red study; electron-phonon coupling is weaker than the SP coupling [Ref. 1.24].

The other example of spin-orbit coupling induced SP coupling is $\text{Y}_2\text{Ir}_2\text{O}_7$. In this compound, the O-Ir-O bond change from vibration induces the variation of DM interaction. According to the stress tensor of the spin part, the phonon energy change can be induced by the deviation of DM interaction. J. Son et al. [Ref. 1.28] found that the large phonon energy renormalization of O-Ir-O bond bending mode by using optical spectroscopy. Also, in their calculation, the DM interaction is sensitive to the O-Ir-O bond angle. And the phonon mode, which affects the bond angle when they vibrate, has a similar dependency with the calculations.

Although both examples show the importance of spin-orbit coupling in SP coupling, we still think that a complete understanding of SP coupling is required. Because the information obtained from optical spectroscopy is restricted to phonons in the long-wavelength limit, only detecting few IR active phonons. From our perspective, to thoroughly investigate the phonons in $\text{Cd}_2\text{Os}_2\text{O}_7$, the phonons should be measured in a wide range of momentum and energy space using IXS. If there is a possibility of magnon-phonon coupling, similar to the HoMnO_3 case, we need to obtain phonon dispersions. The results of $\text{Cd}_2\text{Os}_2\text{O}_7$ are discussed in detail in Chap. 5.

1.2 Outline of the thesis

In this section, I will briefly introduce the outline of the thesis. In Chap. 2, I will explain the theoretical backgrounds used in the study on the magnon-phonon coupling.

Furthermore, the basic principles of the LSWT and the formalism of the magnons and phonons are discussed. In detail, I also introduce a way for understanding the higher-order interaction, such as magnon–magnon interaction.

In Chap. 3, I will focus on the experimental tools that I used at the large facilities for the inelastic neutron and X-ray scatterings. The basic principles of each scattering experiments and methods are presented in this chapter. Moreover, the formalism of the scattering cross-sections that are directly observed from the experiments is described. Some details of experimental techniques are also included.

In Chap. 4, I will discuss the INS results on HoMnO_3 single crystal. The main experimental findings are summarized in this chapter. Furthermore, a theoretical approach using three different models, such as magnon–magnon interaction and magnon–phonon coupling, are explained. Finally, this chapter will be concluded by a discussion on determining the dominant interaction in HoMnO_3 .

In Chap. 5, I will summarize the results of the IXS experiment performed on $\text{Cd}_2\text{OS}_2\text{O}_7$. Based on the observed phonon dispersion and spectra, I confirmed several anomalous features from the SP coupling. The direct comparison between the observation and the calculated phonon spectra using the density-functional theory revealed an excellent agreement.

References

- [Ref. 1.1] C. Kittel, Phys. Rev. **110**, 836 (1958).
- [Ref. 1.2] S. W. Lovesey, J. Phys. C Solid State Phys. **5**, 2769 (1972).
- [Ref. 1.3] G. Laurence and D. Petitgrand, Phys. Rev. B **8**, 2130 (1973).
- [Ref. 1.4] H. Montgomery and A. P. Cracknell, J. Phys. C Solid State Phys. **6**, 3156 (1973).
- [Ref. 1.5] U. Balucani and A. Stasch, Phys. Rev. B **32**, 182 (1985).
- [Ref. 1.6] J. Jensen and J. G. Houmann, Phys. Rev. B **12**, 320 (1975).
- [Ref. 1.7] J. Jensen, J. Phys. C Solid State Phys. **9**, 111 (1976).
- [Ref. 1.8] S. Lee, A. Pirogov, M. Kang, K.-H. Jang, M. Yonemura, T. Kamiyama, S.-W. Cheong, F. Gozzo, N. Shin, H. Kimura, Y. Noda, and J.-G. Park, Nature **451**, 805 (2008).
- [Ref. 1.9] H. Sim, J. Oh, J. Jeong, M. D. Le, and J.-G. Park, Acta Crystallogr. Sect. B Struct. Sci. Cryst. Eng. Mater. **72**, 3 (2016).
- [Ref. 1.10] M. Fiebig, T. Lottermoser, D. Meier, and M. Trassin, Nat. Rev. Mater. **1**, 16046 (2016).
- [Ref. 1.11] J. Oh, M. D. Le, J. Jeong, J. Lee, H. Woo, W.-Y. Song, T. G. Perring, W. J. L. Buyers, S.-W. Cheong, and J.-G. Park, Phys. Rev. Lett. **111**, 257202 (2013).
- [Ref. 1.12] J. Oh, M. D. Le, H.-H. Nahm, H. Sim, J. Jeong, T. G. Perring, H. Woo, K. Nakajima, S. Ohira-Kawamura, Z. Yamani, Y. Yoshida, H. Eisaki, S. W. Cheong, A. L. Chernyshev, and J.-G. Park, Nat. Commun. **7**, 13146 (2016).

- [Ref. 1.13] T. Kim, J. C. Leiner, K. Park, J. Oh, H. Sim, K. Iida, K. Kamazawa, and J.-G. Park, *Phys. Rev. B* **97**, 201113 (2018).
- [Ref. 1.14] K. Park, J. Oh, K. H. Lee, J. C. Leiner, H. Sim, H. Nahm, T. Kim, J. Jeong, D. Ishikawa, A. Q. R. Baron, and J. Park, *Phys. Rev. B* **102**, 085110 (2020).
- [Ref. 1.15] T. Kim, K. Park, J. C. Leiner, and J.-G. Park, *J. Phys. Soc. Japan* **88**, 81003 (2019).
- [Ref. 1.16] S. Tóth, B. Wehinger, K. Rolfs, T. Birol, U. Stuhr, H. Takatsu, K. Kimura, T. Kimura, H. M. Rønnow, and C. Rüegg, *Nat. Commun.* **7**, 13547 (2016).
- [Ref. 1.17] K. Park, J. Oh, J. C. Leiner, J. Jeong, K. C. Rule, M. D. Le, and J.-G. Park, *Phys. Rev. B* **94**, 104421 (2016).
- [Ref. 1.18] S. Choi, H. Sim, S. Kang, K.-Y. Choi, and J.-G. Park, *J. Phys. Condens. Matter* **29**, 095602 (2017).
- [Ref. 1.19] X. Fabrèges, S. Petit, I. Mirebeau, S. Pailhès, L. Pinsard, A. Forget, M. T. Fernandez-Diaz, and F. Porcher, *Phys. Rev. Lett.* **103**, 067204 (2009).
- [Ref. 1.20] E. R. Callen and H. B. Callen, *Phys. Rev.* **129**, 578 (1963).
- [Ref. 1.21] E. Callen and H. B. Callen, *Phys. Rev.* **139**, A455 (1965).
- [Ref. 1.22] S. L. Holm, A. Kreisel, T. K. Schäffer, A. Bakke, M. Bertelsen, U. B. Hansen, M. Retuerto, J. Larsen, D. Prabhakaran, P. P. Deen, Z. Yamani, J. O. Birk, U. Stuhr, C. Niedermayer, A. L. Fennell, B. M. Andersen, and K. Lefmann, *Phys. Rev. B* **97**, 134304 (2018).

- [Ref. 1.23] S. Pailhès, X. Fabrèges, L. P. Régnault, L. Pinsard-Godart, I. Mirebeau, F. Moussa, M. Hennion, and S. Petit, *Phys. Rev. B* **79**, 134409 (2009).
- [Ref. 1.24] C. H. Sohn, C. H. Kim, L. J. Sandilands, N. T. M. Hien, S. Y. Kim, H. J. Park, K. W. Kim, S. J. Moon, J. Yamaura, Z. Hiroi, and T. W. Noh, *Phys. Rev. Lett.* **118**, 117201 (2017).
- [Ref. 1.25] A. W. Sleight, J. L. Gillson, J. F. Weiher, and W. Bindloss, *Solid State Commun.* **14**, 357 (1974).
- [Ref. 1.26] D. Mandrus, J. R. Thompson, R. Gaal, L. Forro, J. C. Bryan, B. C. Chakoumakos, L. M. Woods, B. C. Sales, R. S. Fishman, and V. Keppens, *Phys. Rev. B* **63**, 195104 (2001).
- [Ref. 1.27] Z. Hiroi, J. Yamaura, T. Hirose, I. Nagashima, and Y. Okamoto, *APL Mater.* **3**, 41501 (2015).
- [Ref. 1.28] J. Son, B. C. Park, C. H. Kim, H. Cho, S. Y. Kim, L. J. Sandilands, C. Sohn, J.-G. Park, S. J. Moon, and T. W. Noh, *npj Quantum Mater.* **4**, 17 (2019).

Chapter 2

Theoretical backgrounds

2.1 Linear spin-wave theory

In this chapter, I would like to introduce the linear spin-wave theory (LSWT) briefly. It is a primary method to explain the interaction between spins. We can use the LSWT to interpret spin-waves usually observed in inelastic neutron scattering (INS). Spin-waves are one kind of collective excitations in magnetic compounds. If the spins are ordered at a specific temperature, the continuous symmetry is spontaneously breaking. Based on the Goldstone theorem, it forces the emergence of the gapless excitations. As spin-waves are also called magnons in the viewpoint of quasiparticles, their dispersion relations can also be analyzed using the LSWT. Here, I would explain some well-known formulas adapted from several references [Refs. 2.1–2.7].

2.1.1 Spin Hamiltonian for triangular antiferromagnet

The simplest spin Hamiltonian for the magnetic material can be described by the nearest-neighbor Heisenberg exchange interaction J_{ij} and the atoms' spin \mathbf{S}_i and \mathbf{S}_j .

$$H_{ex} = \sum_{\langle ij \rangle} J_{ij} \mathbf{S}_i \cdot \mathbf{S}_j$$

A type of exchange interaction can be determined by a sign of J . If $J < 0$, spins have a ferromagnetic exchange interaction, whereas if $J > 0$, spins have an antiferromagnetic exchange interaction. Depending on the crystal and magnetic structure, we need to add

further-nearest neighbor exchange interaction to describe the spin dynamics fully.

In case the materials having an anisotropy, the spin Hamiltonian should include the anisotropy term.

$$H_{aniso} = D \sum_i (\mathbf{S}_i \cdot \mathbf{n}_i)^2$$

D is a single-ion anisotropy, and \mathbf{n}_i is a unit vector that explains the local anisotropy direction. If $D > 0$, it is called an easy-plane type anisotropy so that spins tend to align within a specific plane. If $D < 0$, it is an easy-axis type anisotropy, and spins are aligned parallel to \mathbf{n}_i direction.

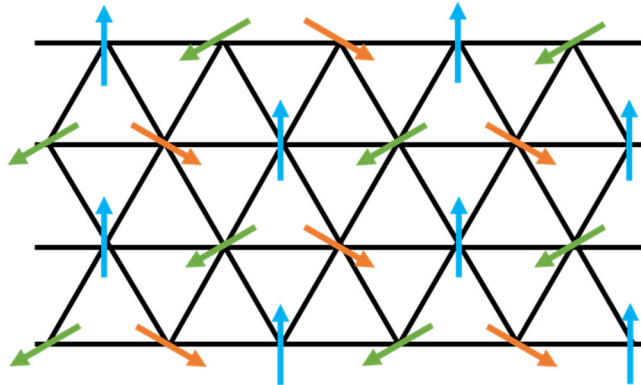


Figure 2.1 The 120° ordering state in a triangular lattice.

Here, I would like to focus on describing the spin Hamiltonian for the two-dimensional triangular lattice antiferromagnet. All natural triangular magnetic systems have nonzero D , and the magnetic ground state when $D > 0$ shows that spins are confined to the ab plane. If $D < 0$, the magnetic ground state is that spins are aligned perpendicular to the ab plane. In h - RMnO_3 , the usual magnetic ground state in zero fields is the 120° ordered state, as shown in Fig. 2.1. To solve the Hamiltonian, we need to figure out the

number of bases in the magnetic unit cell. For the case of triangular systems, we need three bases to interpret the spin Hamiltonian as follows. Based on the transformation from the laboratory coordinates (x_0, y_0, z_0) to the local coordinates (x, y, z) , the spin operator can be formulated as follows,

$$\mathbf{S}_i = \begin{pmatrix} S_i^{x_0} \\ S_i^{y_0} \\ S_i^{z_0} \end{pmatrix}_{lab} = \begin{pmatrix} 1 & 0 & 0 \\ 0 & \cos\varphi_i & -\sin\varphi_i \\ 0 & \sin\varphi_i & \cos\varphi_i \end{pmatrix} \begin{pmatrix} S_i^x \\ S_i^y \\ S_i^z \end{pmatrix}_{local}, i = 1,2,3$$

The 120° ordering state, i.e., the noncollinear magnetic structure, has a unique effect in the spin excitations different from the collinear magnetic structure. By using the above transformation, we can re-write the spin Hamiltonian H_{ex} .

$$H_{ex} = J \sum_{\langle ij \rangle} \mathbf{S}_i \cdot \mathbf{S}_j = J \sum_{\langle ij \rangle} \left[S_i^x S_j^x + \cos\varphi_{ij} (S_i^y S_j^y + S_i^z S_j^z) + \sin\varphi_{ij} (S_i^z S_j^y - S_i^y S_j^z) \right]$$

Here, we assume that the spins lie in the xz plane. φ_{ij} indicates the angle difference between spin \mathbf{S}_i and \mathbf{S}_j . In the 120° ordering state, it is a constant of $2\pi/3$.

2.1.2 Holstein-Primakoff transformation

The local spin operators can be transformed into bosonic forms by the Holstein-Primakoff transformation [Ref. 2.8], as formulated below,

$$S_i^+ = \sqrt{2S} \left(1 - \frac{a_i^\dagger a_i}{2S} \right)^{\frac{1}{2}} a_i = \sqrt{2S} \left(1 - \frac{1}{2} \frac{a_i^\dagger a_i}{2S} + \dots \right) a_i$$

$$S_i^- = \sqrt{2S} a_i^\dagger \left(1 - \frac{a_i^\dagger a_i}{2S} \right)^{1/2} = \sqrt{2S} a_i^\dagger \left(1 - \frac{1}{2} \frac{a_i^\dagger a_i}{2S} + \dots \right)$$

$$S_i^z = S - a_i^\dagger a_i$$

, where $S_i^\pm = S_i^x \pm iS_i^y$. a_i is a magnon operator and satisfies the relation of $[a_i, a_j^\dagger] = \delta_{ij}$. As shown in the above formula, the spin operator S_i^\pm can be expressed by Taylor expansion. In the classical limit, we can assume $a_i^\dagger a_i \ll S_i$ so that we can neglect the $(a_i^\dagger a_i/2S)^n$ terms. It makes a linear approximation of the spin operators, and each operator can be simplified as,

$$S_i^x \approx \sqrt{\frac{S}{2}}(a_i + a_i^\dagger), \quad S_i^y \approx -i\sqrt{\frac{S}{2}}(a_i - a_i^\dagger), \quad S_i^z = S - a_i^\dagger a_i.$$

Based on these formulations, we can re-write the H_{ex} in magnon operators forms.

$$H_{ex} = H_0 + H_1 + H_2 + H_3 + H_{n>3}.$$

$$H_0 = JS^2 \sum_{\langle ij \rangle} \cos\varphi_{ij}$$

$$H_1 = iJS \sqrt{\frac{S}{2}} \sum_{\langle ij \rangle} \sin\varphi_{ij} (a_i - a_i^\dagger - a_j + a_j^\dagger)$$

$$H_2 = \frac{JS}{2} \sum_{\langle ij \rangle} [(1 - \cos\varphi_{ij})(a_i a_j + a_i^\dagger a_j^\dagger) + (1 + \cos\varphi_{ij})(a_i^\dagger a_j + a_i a_j^\dagger) - 2\cos\varphi_{ij}(a_i^\dagger a_i + a_j^\dagger a_j)]$$

$$H_3 = ij \sqrt{\frac{S}{2}} \sum_{\langle ij \rangle} \sin\varphi_{ij} (a_i^\dagger a_i (a_j - a_j^\dagger) - (a_i - a_i^\dagger) a_j^\dagger a_j)$$

Here, H_n indicates the Hamiltonian including n -th powers of the magnon operators so that

it has an order of $(\frac{1}{S})^{\frac{1}{2}n-2}$. I neglect H_n terms for the $n > 3$ cases. Because H_n value

decreases as n increases. H_1 vanishes automatically because the 120° spin structure corresponds to a minimum of the classical energy [Ref. 2.7]. The quadratic term H_2 is the lowest-order terms and we usually consider H_2 in the LSWT to describe spin-waves. H_3 term includes three magnon operators, and if this term is large, an anharmonic behavior appears in magnon dispersion. The H_3 term will be discussed later in Sect. 2.2.

In order to explain magnon dispersion relations based on the spin Hamiltonian, we need to do a Fourier transformation from real space to momentum space. I adapted formulas from [Ref. 2.7].

$$a_i = \frac{1}{\sqrt{N}} \sum_{\mathbf{k}} e^{i\mathbf{k}\cdot\mathbf{r}_i} a_{\mathbf{k}}, \quad a_i^\dagger = \frac{1}{\sqrt{N}} \sum_{\mathbf{k}} e^{-i\mathbf{k}\cdot\mathbf{r}_i} a_{\mathbf{k}}^\dagger$$

Substituting the above equations to H_2 corresponds to below,

$$H_2(\mathbf{k}) = \sum_{\mathbf{k}} \left[A_{\mathbf{k}} a_{\mathbf{k}}^\dagger a_{\mathbf{k}} - \frac{1}{2} B_{\mathbf{k}} (a_{\mathbf{k}}^\dagger a_{-\mathbf{k}}^\dagger + a_{-\mathbf{k}} a_{\mathbf{k}}) \right].$$

$$A_{\mathbf{k}} = 3JS \left(1 + \frac{1}{2} \gamma_{\mathbf{k}} \right), \quad B_{\mathbf{k}} = \frac{9}{2} JS \gamma_{\mathbf{k}}$$

$$\gamma_{\mathbf{k}} = \frac{1}{6} \sum_{\mathbf{v}} e^{i\mathbf{k}\cdot\mathbf{v}} = \frac{1}{6} \sum_{n=1}^6 e^{i(k_x, k_y) \cdot (\cos(\frac{n\pi}{3}), \sin(\frac{n\pi}{3}))} = \frac{1}{3} \left(\cos k_x + 2 \cos \frac{k_x}{2} \cos \frac{\sqrt{3}}{2} k_y \right)$$

To diagonalize $H_2(\mathbf{k})$, we could use the Bogolyubov transformation as follows,

$$a_{\mathbf{k}} = u_{\mathbf{k}} b_{\mathbf{k}} + v_{\mathbf{k}} b_{-\mathbf{k}}^\dagger, \quad a_{-\mathbf{k}}^\dagger = v_{\mathbf{k}} b_{\mathbf{k}} + u_{\mathbf{k}} b_{-\mathbf{k}}^\dagger$$

$$\text{where,} \quad u_{\mathbf{k}}^2 - v_{\mathbf{k}}^2 = 1, \quad u_{\mathbf{k}}^2 + v_{\mathbf{k}}^2 = \frac{A_{\mathbf{k}}}{\sqrt{A_{\mathbf{k}}^2 - B_{\mathbf{k}}^2}}, \quad 2u_{\mathbf{k}}v_{\mathbf{k}} = \frac{B_{\mathbf{k}}}{\sqrt{A_{\mathbf{k}}^2 - B_{\mathbf{k}}^2}}$$

Considering up to quadratic terms of the spin Hamiltonian, we can get the final spin-wave Hamiltonian as below,

$$H_{ex}(\mathbf{k}) = H_0(\mathbf{k}) + H_2(\mathbf{k}) = -\frac{3}{2}NJS(S+1) + \sum_{\mathbf{k}} \varepsilon_{\mathbf{k}} \left(b_{\mathbf{k}}^{\dagger} b_{\mathbf{k}} + \frac{1}{2} \right),$$

$$\varepsilon_{\mathbf{k}} = \sqrt{A_{\mathbf{k}}^2 - B_{\mathbf{k}}^2} = 3JS\omega_{\mathbf{k}} = 3JS\sqrt{(1-\gamma_{\mathbf{k}})(1+2\gamma_{\mathbf{k}})}.$$

2.2 Magnon-magnon interaction

As one might notice, H_{ex} includes $\cos\varphi_{ij}$ and $\sin\varphi_{ij}$ terms. In collinear magnets, the $\sin\varphi_{ij}$ term vanishes, whereas the $\sin\varphi_{ij}$ term survives in noncollinear magnets. As a result, H_3 , which contains three magnon operators or cubic terms, does not vanish, and acts as a perturbation in the LSWT. It is usually small to be neglected, but it is possible to have a sizable magnon-magnon interaction in $S = 1/2$ case. A. V. Chubukov et al. demonstrated that the first-order correction in the $1/S$ expansion could be non-negligible for the $S = 1/2$ case [Ref. 2.9]. Later, A. L. Chernyshev and M. E. Zhitomirsky et al. conducted a comprehensive theoretical study on the quantum corrections to the spin-wave dispersion and the magnon lifetime in triangular lattice antiferromagnet [Refs. 2.7, 2.10, and 2.11]. W. Zheng et al. performed a quantum Monte-Carlo simulation and found the effects of the magnon-magnon interaction on the magnon dispersion and energy [Ref. 2.12]. M. Mourigal et al. provided the dynamical structure factor's detailed calculation results, including the magnon-magnon interaction [Ref. 2.13]. In this section, I would like to show some characteristic features of the magnon-magnon interaction effects.

2.2.1 Three-magnon interaction term

Using the Holstein-Primakoff transformation, the spin Hamiltonian for the three-magnon interaction term H_3 can be re-written as below [Ref. 2.7],

$$H_3 = \frac{1}{2!} \sum_{\mathbf{q}, \mathbf{k}} \Gamma_1(\mathbf{q}, \mathbf{k} - \mathbf{q}; \mathbf{k}) (a_{\mathbf{k}-\mathbf{q}}^\dagger a_{\mathbf{q}}^\dagger a_{\mathbf{k}} + h.c.) \\ + \frac{1}{3!} \sum_{\mathbf{q}, \mathbf{k}} \Gamma_2(\mathbf{q}, -\mathbf{k} - \mathbf{q}, \mathbf{k}) (a_{\mathbf{q}}^\dagger a_{-\mathbf{k}-\mathbf{q}}^\dagger a_{\mathbf{k}}^\dagger + h.c.).$$

Here, $\Gamma_1(\mathbf{q}, \mathbf{k} - \mathbf{q}; \mathbf{k})$ is the vertex function that describes the decay of one-magnon into the two-magnon states. We called this term magnon-magnon interaction here. $\Gamma_2(\mathbf{q}, -\mathbf{k} - \mathbf{q}, \mathbf{k})$ indicates the creation of three magnons. The cubic terms' effects appear in both the magnon energy and the lifetime due to the induced decay process. Using the standard Green's function method, the lowest-order normal self-energies from the cubic vertexes can be expressed in the following formulae [Ref. 2.7],

$$\Sigma_1(\mathbf{k}, \omega) = \frac{1}{2} \sum_{\mathbf{q}} \frac{|\Gamma_1(\mathbf{q}; \mathbf{k})|^2}{\omega - \varepsilon_{\mathbf{q}} - \varepsilon_{\mathbf{k}-\mathbf{q}} + i0}, \\ \Sigma_2(\mathbf{k}, \omega) = -\frac{1}{2} \sum_{\mathbf{q}} \frac{|\Gamma_2(\mathbf{q}; \mathbf{k})|^2}{\omega + \varepsilon_{\mathbf{q}} + \varepsilon_{\mathbf{k}+\mathbf{q}} + i0}.$$

Here, some explicit expressions are not explained, and one can find those in [Ref. 2.7].

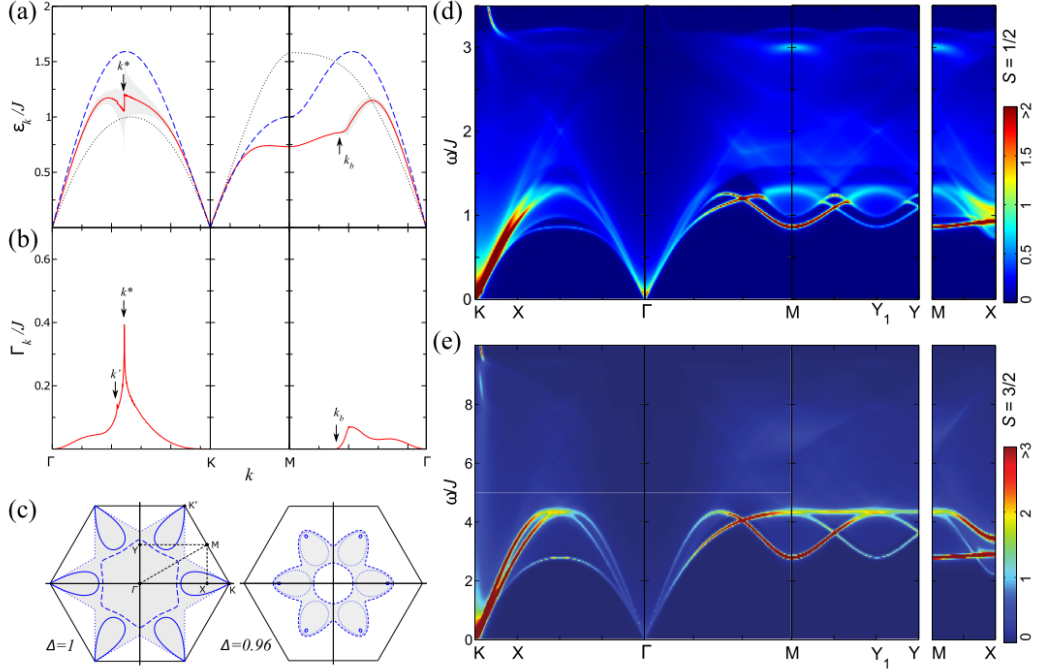


Figure 2.2 (a) The calculated magnon dispersion and (b) the decay rate for the triangular lattice with $S=1/2$. The dashed line indicates the LSWT calculation results, and the solid line indicates the results with $1/S$ corrections. The shaded area shows the width of the spectral peaks due to decay. (c) The shaded area is the region in which the decay process occurs. When the anisotropy Δ decreases, the decay region also shrinks. The calculated dynamical structure factor from the $1/S$ corrections is plotted in (d) $S=1/2$ and (e) $S=3/2$. The figures are reprinted from [Ref. 2.1], adapted from [Refs. 2.7 & 2.13].

The main features observed in actual experiments such as INS are strong renormalization of magnons, shortening of magnon lifetime, and momentum dependence.

As shown in Fig. 2.2(a), a local minimum of the magnon exists at the M point and flattened magnon energy around the M point. The local minimum is sometimes called a roton-like minimum since the local minimum feature is similar to a roton excitation feature in ^4He .

Not only the magnon energy but also the decay rate is strongly dependent on the momentum. And the strong dampening of the magnons and the broad continuum state are expected due to the decay. The decay process should satisfy some conditions: (1) $\Gamma_1(\mathbf{q}; \mathbf{k})$ is nonzero, and (2) the kinematic conditions of momentum and energy conservation are satisfied. The decay rate $\Gamma_{\mathbf{k}}$ is directly related to the magnon lifetime, which is approximately determined as below,

$$\Gamma_{\mathbf{k}} = \frac{\pi}{2} \sum_{\mathbf{q}} |\Gamma_1(\mathbf{q}; \mathbf{k})|^2 \delta(\varepsilon_{\mathbf{k}} - \varepsilon_{\mathbf{q}} - \varepsilon_{\mathbf{k}-\mathbf{q}}).$$

The decay rate in the $S=1/2$ triangular lattice case is shown in Fig. 2.2(b). The decay rate abruptly increases in the middle of Γ and K point, which is a similar behavior with the magnon energy renormalization. As expected, the dynamical structure factor calculation revealed that the broadening of the magnons and the diffuse intensity of the magnon continuum above the one-magnon exist, as shown in Fig. 2.2(d). The effect of magnon-magnon interaction is somewhat suppressed in the case of $S=3/2$, as plotted in Fig. 2.2(e). The reason for this suppression is that the large S would reduce the magnon-magnon interaction. Also, the quantum fluctuation would decrease the interaction as well.

2.3 Magnon-phonon coupling

A magnon-phonon coupling can be considered one type of spin-lattice coupling, or sometimes called magneto-elastic coupling. The concept of magneto-elastic coupling was started a long time ago, and it is extensively studied. For example, h - $RMnO_3$ is a famous compound that has strong spin-lattice coupling. The coupling causes a change of atomic positions accompanied by a magnetic order, and it induces the electric polarization in the materials [Ref. 2.14], well-known as the magneto-electric coupling. The applicability of the magneto-electric coupling attracts many researchers to study it as well as the spin-lattice coupling. Various experimental tools observed abrupt changes through the magnetic transition appeared in fundamental properties, for example, X-ray/neutron diffraction [Refs. 2.14–2.18], infra-red (IR) or Raman spectroscopy [Refs. 2.19–2.26], thermal conductivity [Refs. 2.27 & 2.28], elastic moduli [Refs. 2.29 & 2.30], and thermal expansion [Refs. 2.31 & 2.32] measurements.

Although the spin-lattice coupling is essential to determine the fundamental and static properties, it also affects some of the dynamical properties. When the phonons and magnons are close to each other, they can interact and repel each other. Or, they can hybridize and form a magneto-elastic excitation [Ref. 2.33]. These magneto-elastic excitations have both phonon and magnon characters so that we can probe the excitations using both x-ray and neutron scattering. For example, in $YMnO_3$, the magneto-elastic excitations were observed in INS and IXS [Refs. 2.33 & 2.34]. The similar magneto-elastic excitations in $LiCrO_2$ are also discovered using both INS and IXS [Ref. 2.35]. There are several scenarios to explain how the magneto-elastic excitations emerge. Here, I would like

to introduce one of the mechanisms, called exchange-striction.

2.3.1 Exchange-striction model

In this section, I would like to introduce the exchange-striction model. The primary mechanism is that the modulation of atomic positions due to lattice vibration induces the exchange interaction between atoms. Because the exchange interaction J depends on the bond length $r_{ij} = |\mathbf{r}_j - \mathbf{r}_i|$ between site i and j . Using Taylor expansions, the exchange interaction can be expressed as below,

$$\begin{aligned} J_{ij}(\mathbf{r}_i, \mathbf{r}_j) &= J_{ij}(\mathbf{R}_i, \mathbf{R}_j) + (\mathbf{u}_i \cdot \nabla_{\mathbf{r}_i} + \mathbf{u}_j \cdot \nabla_{\mathbf{r}_j}) J_{ij} + \frac{1}{2!} (\mathbf{u}_i \cdot \nabla_{\mathbf{r}_i} + \mathbf{u}_j \cdot \nabla_{\mathbf{r}_j})^2 J_{ij} + \dots \\ &\approx J_0 \left(1 - \frac{1}{J_0} \frac{\partial J}{\partial r} \mathbf{e}_{ij} \cdot (\mathbf{u}_j - \mathbf{u}_i) \right) \end{aligned}$$

where $\mathbf{r}_i = \mathbf{R}_i + \mathbf{u}_i$ is the position of atom i and \mathbf{R}_i and \mathbf{u}_i are the equilibrium position and the atomic displacement of atom i . The second quantization form of the atomic displacement (or phonon displacement) is as follow,

$$\mathbf{u}_i = \sum_{\mathbf{k}, \lambda} \sqrt{\frac{\hbar}{2Nm_i\omega_{\mathbf{k},\lambda}}} e_{\mathbf{k},\lambda} (b_{\mathbf{k},\lambda} + b_{-\mathbf{k},\lambda}^\dagger) e^{i\mathbf{k}\cdot\mathbf{R}_i}.$$

\mathbf{u}_i contains a linear term of phonon creation and annihilation operators. In noncollinear magnets, H_{ex} contains one-magnon terms in the Hamiltonian. As a result, if we substitute the atomic displacement \mathbf{u}_i and the exchange interaction $J_{ij}(\mathbf{r}_i, \mathbf{r}_j)$ into the H_{ex} , we can get the magnon-phonon coupling Hamiltonian [Ref. 2.1], which have a linear coupling between magnon and phonon operators,

$$H_{mp} = \sum_k g_{k,\lambda} (a_k^\dagger - a_{-k}) b_{k,\lambda} + h.c.,$$

$$g_{k,\lambda} = -i \frac{3}{4} \alpha \sqrt{\frac{S^3 \hbar}{M \omega_{k,\lambda}}} e_{k,\lambda} \cdot f_k,$$

where $\alpha = \frac{d}{J} \frac{\partial J}{\partial r}$ (d is a bond length between the site i and j) is a dimensionless unit of the exchange-striction coefficient, and $f_k = \sum_{\mathbf{v}} \sin(\mathbf{Q} \cdot \mathbf{v}) [\cos(\mathbf{k} \cdot \mathbf{v}) - 1] \mathbf{v}$ is a geometrical factor. So, the total Hamiltonian H_{tot} including all the Hamiltonian of phonon H_{ph} , magnon H_{mag} , and magnon-phonon coupling term H_{mp} can be re-write using the basis of phonon and magnon operators. The magnon-phonon coupling term H_{mp} contributes to the off-diagonal component of the H_{tot} [Refs. 2.3 & 2.4].

Table 2.1 Exchange-striction coefficients α for selected oxides

Materials	α	Refs.
CuGeO ₃	3.5	[Ref. 2.36]
La ₂ CuO ₄	2-7	[Refs. 2.37 & 2.38]
(Y,Lu)MnO ₃	8-10	[Ref. 2.33]
HoMnO ₃	12.8	[Ref. 2.39]
LiCrO ₂ & CuCrO ₂	15.7 & 15.8	[Refs. 2.35 & 2.40]

The exchange-striction coefficient α is an indicator of the magnon-phonon coupling strength. It can be directly extracted from the observed magnon dispersion. Alternatively, one can estimate α from the measurement of Néel temperature and the bond

length as a function of pressure with the following formula [Ref. 2.33],

$$\alpha = \frac{d(P_0) \partial T_N(P) / \partial P}{T_N(P_0) (\partial d(P) / \partial P)}$$

Some of the exchange-striction coefficients are summarized in Table 2.1.

2.3.2 Einstein site phonon model

The Einstein site phonon (ESP) model [Ref. 2.41, Ref. 2.42] is the more straightforward and approximate version of the magnon-phonon coupling Hamiltonian mentioned above. Based on the crystal symmetry and the number of atoms in the unit cell, the number of the basis for the phonons is sometimes large. This makes it somewhat difficult to calculate magnon-phonon coupling Hamiltonian. Also, if the overlap between magnon and phonon is large, the expected coupling constants should be small enough to ignore it. The ESP model concept is that we choose an optimal optical phonon branch and integrate out the site Einstein phonons. This is equivalent to simply minimizing the Hamiltonian with respect to the set of \mathbf{u}_i . By doing this, we can have two advantages: (1) it requires only one control parameter of the coupling constant, and (2) it mimics a richness of phase diagram successfully.

Turn back to the magnon-phonon coupling Hamiltonian H_{mp} , we can add the phonon Hamiltonian to describe all the magnons and phonons in the system as below,

$$H_{tot} = J \sum_{\langle ij \rangle} \left(1 - \alpha \frac{(\mathbf{u}_i - \mathbf{u}_j) \cdot \mathbf{e}_{ij}}{d} \right) \mathbf{S}_i \cdot \mathbf{S}_j + H_{pho}(\{\mathbf{u}_i\}).$$

In the ESP model, the atomic displacements are independently determined, and the bond

distances between atoms are defined from those. So, we can write the phonon Hamiltonian as $H_{pho}(\{\mathbf{u}_i\}) = \frac{K}{2} \sum_i |\mathbf{u}_i|^2$, where K is an elastic constant.

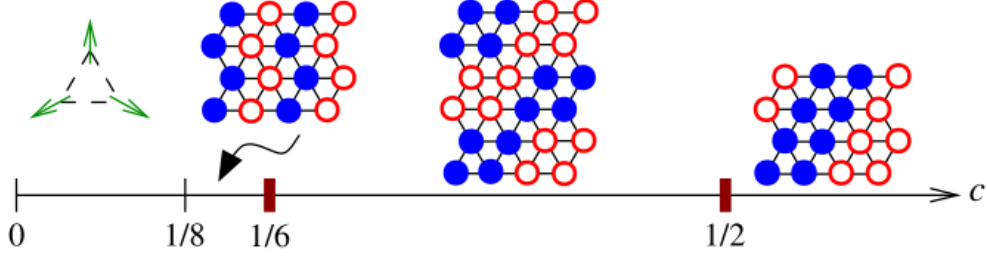


Figure 2.3 Zero-field phase diagram of the triangular lattice calculated by the ESP model. Filled and empty circles mean the direction of the spins (up or down). The figure is adapted from [Ref. 2.42].

By integrating out the lattice displacement \mathbf{u}_i , the effective spin Hamiltonian can be written as follows [Ref. 2.42],

$$H_{ESP} = J \left[\sum_{\langle ij \rangle} \mathbf{S}_i \cdot \mathbf{S}_j - cS^2 \sum_i \mathbf{F}_i^2 \right].$$

$$\mathbf{F}_i = \sum_{j \in N(i)} \frac{(\mathbf{S}_i \cdot \mathbf{S}_j)^2}{S^2} \mathbf{e}_{ij}, \quad c = \frac{\alpha^2 JS^2}{2K}$$

Here, c is a dimensionless spin-phonon coupling constant and \mathbf{F}_i is a dimensionless force on site i . $N(i)$ indicates the nearest-neighbor sites of the site i . The \mathbf{F}_i already implies that the spin-lattice coupling is favorable in this model. If spins are uniformly ordered and $\langle \mathbf{S}_i \cdot \mathbf{S}_j \rangle = const.$, then $\mathbf{F}_i = 0$ results in the Hamiltonian is as same as the simple

Heisenberg model. But, to minimize the Hamiltonian, \mathbf{F}_i tends to have non zero value, and it enforces the distortion of the lattice as the spins are ordered. Based on the H_{ESP} in a triangular lattice, the phase diagram of the magnetic ground state shown in Fig. 2.3 has been discussed in [Ref. 2.42].

2.4 Phonon Hamiltonian

Phonon is also a fundamental quasiparticle describing the collective behavior of lattice vibration. The simplest way to express the phonon Hamiltonian is the harmonic approximation without invoking any phonon-phonon, electron-phonon, or other interactions. The phonon Hamiltonian is simply written as follows,

$$H_{lat} = \sum_{l,d} \frac{\mathbf{P}_{l,d}^2}{2M_d} + \frac{1}{2} \sum_{l,d,l',d'} \mathbf{u}_{l,d} \Phi_{l,d}^{l',d'} \mathbf{u}_{l',d'}.$$

Here, $\mathbf{P}_{l,d}$ is a momentum operator for the d -th atom in the l -th unit cell. $\Phi_{l,d}^{l',d'}$ is an interatomic force-constant matrix with a dimension of 3×3 . $\mathbf{u}_{l,d}$ means the atomic displacement of the d -th atom in the l -th unit cell. The corresponding equation of motion for the H_{lat} is

$$M_d \ddot{\mathbf{u}}_{l,d} = - \sum_{l',d'} \Phi_{l,d}^{l',d'} \mathbf{u}_{l',d'}.$$

Solving this equation of motion based on the assumption of solutions to be formed by a superposition of normal modes with periodicity \mathbf{q} and frequency ω , we can get the following formula,

$$M_d \omega_{qv}^2 e_{qv d}^\alpha = \sum_{d', \beta} D_{\alpha\beta}(dd', \mathbf{q}) e_{qv d'}^\beta.$$

Here, $e_{qv d}^\alpha$ indicates the α -axis component of the eigenvector of the d -th atom with \mathbf{q} and band index v . And the $D_{\alpha\beta}(dd', \mathbf{q})$ is a dynamic matrix, which is a Fourier transform of the force-constant matrix. The dynamical matrix is defined as below,

$$D_{\alpha\beta}(dd', \mathbf{q}) = \frac{1}{\sqrt{M_d M_{d'}}} \sum_{l'} \Phi_{l, d}^{l', d'} e^{i\mathbf{q} \cdot [\mathbf{r}_{l'} - \mathbf{r}_l]}.$$

The density-functional theory (DFT) can usually calculate the interatomic force constant $\Phi_{l, d}^{l', d'}$. Based on the crystal structure setting, crystal symmetry, electron correlation, magnetic moment, and other parameters taking effects on atomic forces, the total energy is calculated until it converges. After determining final atomic positions based on the energy minimization, the force constants are calculated using the frozen phonon method. In $\text{Cd}_2\text{Os}_2\text{O}_7$, which will be discussed in Chapter 5, we used the electron correlation $U = 2.0$ eV, and an all-in-all-out magnetic ordering structure was considered. More importantly, we added spin-orbit coupling in the calculations to calculate the effect from $5d$ Osmium atoms. The example of calculations for $\text{Cd}_2\text{Os}_2\text{O}_7$ phonons is shown in Fig. 2.4.

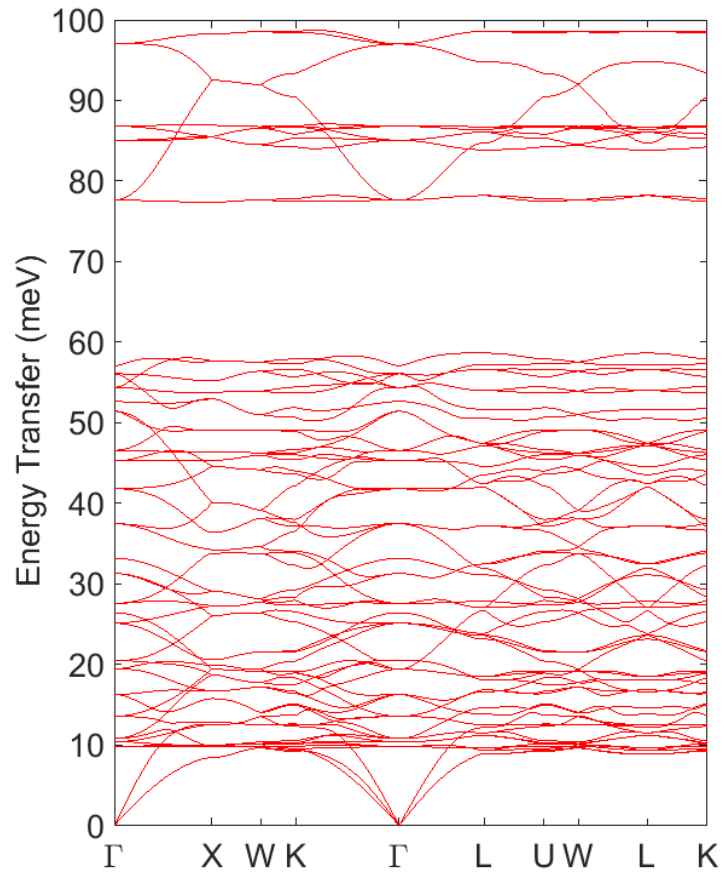


Figure 2.4 The calculated phonon dispersion relations of Cd₂Os₂O₇.

To obtain the phonon frequencies and eigenvectors from the force constants, we implemented the codes in PHONOPY [Ref. 2.43]. In the above calculation, we used the finite displacement method.

References

- [Ref. 2.1] T. Kim, K. Park, J. C. Leiner, and J.-G. Park, *J. Phys. Soc. Japan* **88**, 081003 (2019).
- [Ref. 2.2] J. Jeong, *Spin Dynamics in Multiferroic BiFeO₃: Interplay of Dzyaloshinskii-Moriya Interaction and Anisotropy*, Seoul National University, 2015.
- [Ref. 2.3] J. Oh, *Excitation Spectra of Triangular Antiferromagnet Hexagonal RMnO₃: Spontaneous Decays of Magneto-Elastic Excitation*, Seoul National University, 2017.
- [Ref. 2.4] K. Park, *Excitation Spectra of Triangular Lattice Antiferromagnets Using Inelastic Neutron & X-Ray Scattering*, Seoul National University, 2020.
- [Ref. 2.5] G. L. Squires, Scattering from magnetically ordered crystals, in *Introduction to the Theory of Thermal Neutron Scattering* (Cambridge University Press, Cambridge, n.d.), pp. 146–170.
- [Ref. 2.6] S. Toth and B. Lake, *J. Phys. Condens. Matter* **27**, 166002 (2015).
- [Ref. 2.7] A. L. Chernyshev and M. E. Zhitomirsky, *Phys. Rev. B* **79**, 144416 (2009).
- [Ref. 2.8] T. Holstein and H. Primakoff, *Phys. Rev.* **58**, 1098 (1940).
- [Ref. 2.9] A. V. Chubukov, S. Sachdev, and T. Senthil, *J. Phys. Condens. Matter* **6**, 8891 (1994).
- [Ref. 2.10] A. L. Chernyshev and M. E. Zhitomirsky, *Phys. Rev. Lett.* **97**, 207202 (2006).

- [Ref. 2.11] M. E. Zhitomirsky and A. L. Chernyshev, *Rev. Mod. Phys.* **85**, 219 (2013).
- [Ref. 2.12] W. Zheng, J. O. Fjærestad, R. R. P. Singh, R. H. McKenzie, and R. Coldea, *Phys. Rev. B* **74**, 224420 (2006).
- [Ref. 2.13] M. Mourigal, W. T. Fuhrman, A. L. Chernyshev, and M. E. Zhitomirsky, *Phys. Rev. B* **88**, 094407 (2013).
- [Ref. 2.14] S. Lee, A. Pirogov, M. Kang, K.-H. Jang, M. Yonemura, T. Kamiyama, S.-W. Cheong, F. Gozzo, N. Shin, H. Kimura, Y. Noda, and J.-G. Park, *Nature* **451**, 805 (2008).
- [Ref. 2.15] T. Chatterji, B. Ouladdiaf, P. F. Henry, and D. Bhattacharya, *J. Phys. Condens. Matter* **24**, 336003 (2012).
- [Ref. 2.16] J. Park, S. Lee, M. Kang, K.-H. Jang, C. Lee, S. V. Streltsov, V. V. Mazurenko, M. V. Valentyuk, J. E. Medvedeva, T. Kamiyama, and J.-G. Park, *Phys. Rev. B* **82**, 054428 (2010).
- [Ref. 2.17] S. Lee, A. Pirogov, J. H. Han, J.-G. Park, A. Hoshikawa, and T. Kamiyama, *Phys. Rev. B* **71**, 180413 (2005).
- [Ref. 2.18] Z. Fu, H. S. Nair, Y. Xiao, A. Senyshyn, V. Y. Pomjakushin, E. Feng, Y. Su, W. T. Jin, and T. Brückel, *Phys. Rev. B* **94**, 125150 (2016).
- [Ref. 2.19] T. Sarkar, K. Manna, S. Elizabeth, and P. S. Anil Kumar, *J. Appl. Phys.* **121**, 084102 (2017).
- [Ref. 2.20] J. Vermette, S. Jandl, and M. M. Gospodinov, *J. Phys. Condens. Matter* **20**, 425219 (2008).

- [Ref. 2.21] A. P. Litvinchuk, M. N. Iliev, V. N. Popov, and M. M. Gospodinov, J. Phys. Condens. Matter **16**, 809 (2004).
- [Ref. 2.22] H. Fukumura, S. Matsui, H. Harima, K. Kisoda, T. Takahashi, T. Yoshimura, and N. Fujimura, J. Phys. Condens. Matter **19**, 365239 (2007).
- [Ref. 2.23] H. Fukumura, N. Hasuike, H. Harima, K. Kisoda, K. Fukae, T. Yoshimura, and N. Fujimura, J. Phys. Condens. Matter **21**, 064218 (2009).
- [Ref. 2.24] M. N. Iliev, H.-G. Lee, V. N. Popov, M. V. Abrashev, A. Hamed, R. L. Meng, and C. W. Chu, Phys. Rev. B **56**, 2488 (1997).
- [Ref. 2.25] R. Basistyy, T. N. Stanislavchuk, A. A. Sirenko, A. P. Litvinchuk, M. Kotelyanskii, G. L. Carr, N. Lee, X. Wang, and S.-W. Cheong, Phys. Rev. B **90**, 024307 (2014).
- [Ref. 2.26] A. Ghosh, J. R. Sahu, S. V. Bhat, and C. N. R. Rao, Solid State Sci. **11**, 1639 (2009).
- [Ref. 2.27] J. D. Song, C. Fan, Z. Y. Zhao, F. B. Zhang, J. Y. Zhao, X. G. Liu, X. Zhao, Y. J. Liu, J. F. Wang, and X. F. Sun, Phys. Rev. B **96**, 174425 (2017).
- [Ref. 2.28] P. A. Sharma, J. S. Ahn, N. Hur, S. Park, S. B. Kim, S. Lee, J.-G. Park, S. Guha, and S.-W. Cheong, Phys. Rev. Lett. **93**, 177202 (2004).
- [Ref. 2.29] M. Poirier, F. Laliberté, L. Pinsard-Gaudart, and A. Revcolevschi, Phys. Rev. B **76**, 174426 (2007).
- [Ref. 2.30] M. Poirier, J. C. Lemyre, P.-O. Lahaie, L. Pinsard-Gaudart, and A. Revcolevschi, Phys. Rev. B **83**, 054418 (2011).
- [Ref. 2.31] C. dela Cruz, F. Yen, B. Lorenz, Y. Q. Wang, Y. Y. Sun, M. M.

- Gospodinov, and C. W. Chu, *Phys. Rev. B* **71**, 060407 (2005).
- [Ref. 2.32] S. Choi, H. Sim, S. Kang, K.-Y. Choi, and J.-G. Park, *J. Phys. Condens. Matter* **29**, 095602 (2017).
- [Ref. 2.33] J. Oh, M. D. Le, H.-H. Nahm, H. Sim, J. Jeong, T. G. Perring, H. Woo, K. Nakajima, S. Ohira-Kawamura, Z. Yamani, Y. Yoshida, H. Eisaki, S. W. Cheong, A. L. Chernyshev, and J.-G. Park, *Nat. Commun.* **7**, 13146 (2016).
- [Ref. 2.34] K. Park, J. Oh, K. H. Lee, J. C. Leiner, H. Sim, H. Nahm, T. Kim, J. Jeong, D. Ishikawa, A. Q. R. Baron, and J. Park, *Phys. Rev. B* **102**, 085110 (2020).
- [Ref. 2.35] S. Tóth, B. Wehinger, K. Rolfs, T. Birol, U. Stuhr, H. Takatsu, K. Kimura, T. Kimura, H. M. Rønnow, and C. Rüegg, *Nat. Commun.* **7**, 13547 (2016).
- [Ref. 2.36] K. Kodama, *Science* (80-.). **298**, 395 (2002).
- [Ref. 2.37] P. S. Häfliger, S. Gerber, R. Pramod, V. I. Schnells, B. dalla Piazza, R. Chati, V. Pomjakushin, K. Conder, E. Pomjakushina, L. Le Dreau, N. B. Christensen, O. F. Syljuåsen, B. Normand, and H. M. Rønnow, *Phys. Rev. B* **89**, 085113 (2014).
- [Ref. 2.38] A. L. Chernyshev and W. Brenig, *Phys. Rev. B* **92**, 054409 (2015).
- [Ref. 2.39] T. Kim, J. C. Leiner, K. Park, J. Oh, H. Sim, K. Iida, K. Kamazawa, and J.-G. Park, *Phys. Rev. B* **97**, 201113 (2018).
- [Ref. 2.40] K. Park, J. Oh, J. C. Leiner, J. Jeong, K. C. Rule, M. D. Le, and J.-G. Park, *Phys. Rev. B* **94**, 104421 (2016).

- [Ref. 2.41] D. L. Bergman, R. Shindou, G. A. Fiete, and L. Balents, Phys. Rev. B **74**, 134409 (2006).
- [Ref. 2.42] F. Wang and A. Vishwanath, Phys. Rev. Lett. **100**, 077201 (2008).
- [Ref. 2.43] A. Togo and I. Tanaka, Scr. Mater. **108**, 1 (2015).

Chapter 3

Experimental techniques

3.1 Inelastic neutron and X-ray scattering

Inelastic neutron scattering (INS) is a unique and well-developed experimental technique to measure spin dynamics in magnetic materials. Although the recently updated resonant inelastic x-ray scattering (RIXS) technique is also available for detecting magnons [Ref. 3.1], INS is still the best tool to examine a dispersion relation of magnetic excitations with a high resolution of few meV scales. Since the neutron has no charge, it can penetrate deep inside solids and approach the nuclei closer. So, INS can probe phonons as well, which is an essential property in condensed matter systems.

Non-resonant inelastic x-ray scattering (IXS) is also an established tool for investigating phonons in materials. This method can provide a good momentum resolution and negligible background signals. The other benefit of IXS is that it only measures non-magnetic signals from the spectra. As a result, we could entirely focus on phonons from this method. The advantage of IXS is that it is less dependent on sample conditions. Using neutrons, we need to consider several things to avoid irrelevant situations. For example, neutron scattering amplitude is high when the light atoms are involved in the target. It prevents you from getting the information that you want to observe. If some elements with a large neutron absorption rate are inside the target, the scattering cross-sections cannot distinguish the desired signals. Also, INS needs a large sample intrinsically to get visible intensity due to a limit of incident neutron flux. On the other hand, IXS can easily avoid

the mentioned cases.

3.1.1 Basic principles

To measure the excitations such as magnons or phonons experimentally, the probe's wavelength should be in the same order as the distances of atoms in solids. Besides, since magnons' and phonons' typical energy is the 1-100 meV energy scale, it is necessary to have a comparable resolution. As mentioned above, the probing technique also needs interaction with the nuclei or magnetic moments. Both INS and IXS techniques are suitable for solving those problems. The basic principles of inelastic scattering can be expressed as below.

$$\mathbf{Q} = \mathbf{k}_f - \mathbf{k}_i \neq 0$$

$$\hbar\omega = E_f - E_i = \frac{\hbar^2}{2m_n}(\mathbf{k}_f^2 - \mathbf{k}_i^2)$$

The elementary excitations reflect the characteristic features of the governing Hamiltonian. For that reason, the inelastic scattering technique is extensively used to deepen the understanding of the Hamiltonian. Based on the scattering theory, we directly observe the scattering cross-sections from INS and IXS. I briefly introduce the formulations of the inelastic scattering cross-sections for phonons and magnons.

In INS, the scattering cross-sections for phonons and magnons are different. Phonons are created when incident neutrons are scattered from nuclei of atoms. Magnons are created when spins of atoms scatter incident neutrons. So, different processes occur. The scattering cross-sections for phonons can be described as below [Ref. 3.2].

$$\left(\frac{d^2\sigma}{d\Omega dE'}\right)_{pho.} = \frac{k'}{k} \frac{(2\pi)^3}{2v_0} \sum_s \sum_{\tau} \frac{1}{\omega_s} \left| \sum_d \frac{\bar{b}_d}{\sqrt{M_d}} \exp(-W_d) \exp(i\boldsymbol{\kappa} \cdot \mathbf{d}) (\boldsymbol{\kappa} \cdot \mathbf{e}_{ds}) \right|^2$$

$$\times \langle n_s + 1 \rangle \delta(\omega - \omega_s) \delta(\boldsymbol{\kappa} - \mathbf{q} - \boldsymbol{\tau})$$

Here, k and k' are the momentum vectors of the incident and scattered neutrons. ω_s is the phonon energy for mode s . M_d is the mass of the atom at position d . \bar{b}_d is the average scattering length of the atom at position d . \mathbf{e}_{ds} is the polarization vector for the atom at position d and mode s . W_d is the Debye-Waller factor, which is defined as below,

$$W_d = \frac{\hbar}{4M_d N} \sum_s \frac{|\boldsymbol{\kappa} \cdot \mathbf{e}_{ds}|^2}{\omega_s} \langle 2n_s + 1 \rangle.$$

$\langle n_s + 1 \rangle$ and $\langle 2n_s + 1 \rangle$ can be considered as a function of temperature and described as following,

$$\langle n_s \rangle = \left(\exp\left(\frac{\hbar\omega_s}{k_B T}\right) - 1 \right)^{-1}$$

$$\langle n_s + 1 \rangle = \frac{\exp\left(\frac{\hbar\omega_s}{k_B T}\right)}{\exp\left(\frac{\hbar\omega_s}{k_B T}\right) - 1}, \quad \langle 2n_s + 1 \rangle = \frac{\left(\exp\left(\frac{\hbar\omega_s}{k_B T}\right) + 1\right)}{\left(\exp\left(\frac{\hbar\omega_s}{k_B T}\right) - 1\right)} = \coth\left(\frac{1}{2} \frac{\hbar\omega_s}{k_B T}\right)$$

As formulated, to obtain the finite scattering cross-sections, two conditions should be satisfied. One is $\omega = \omega_s$, and the other is $\boldsymbol{\kappa} = \mathbf{k} - \mathbf{k}' = \boldsymbol{\tau} + \mathbf{q}$. The first condition means that the amount of energy loss of neutrons should be the same as a phonon's energy, called energy conservation. The second condition also describes the conservation of momentum. For the non-resonant IXS case, we can only probe the phonons, and the scattering cross-sections can be expressed as similar to the above neutron case except for the scattering length b_d . It needs to be replaced with the atomic form factor $f(\mathbf{Q})$.

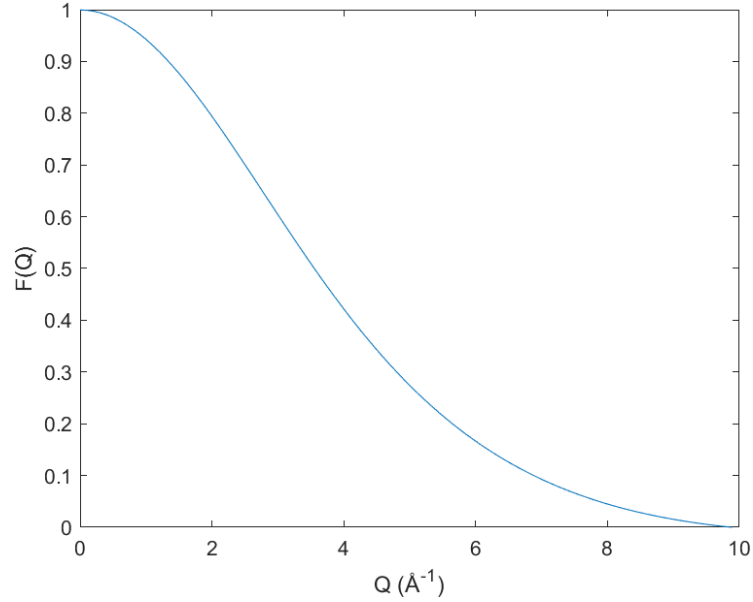


Figure 3.1 The magnetic form factor of Mn^{3+} .

In the case of magnon, the inelastic scattering cross-section is formulated as below,

$$\left(\frac{d^2\sigma}{d\Omega dE'}\right)_{mag.} = (\gamma r_0)^2 \frac{k'}{k} F^2(Q) \exp(-2W_Q) \sum_{\alpha,\beta} \left(\delta_{\alpha\beta} - \frac{Q_\alpha Q_\beta}{Q^2}\right) S^{\alpha\beta}(Q, \omega).$$

Here, γ is a positive constant of 1.913. r_0 is defined as $r_0 = \frac{\mu_0 e^2}{4\pi m_e}$. $F(Q)$ is called the magnetic form factor. It is a momentum and atom dependent quantity, and it decreases when Q becomes large. This is why the signals of magnons from INS are small when we take the spectra at high Q . An example of the magnetic form factor of Mn^{3+} is shown in Fig. 3.1. The $\exp(-2W_Q)$ is the Debye-Waller factor and the $\delta_{\alpha\beta} - \frac{Q_\alpha Q_\beta}{Q^2}$ is the polarization vector. $S^{\alpha\beta}(Q, \omega)$ is the dynamical structure factor, which can explain the spin correlation between atoms.

$$S^{\alpha\beta}(Q, \omega) = \frac{1}{2\pi} \sum_{r,r'} \int_{-\infty}^{\infty} e^{iQ \cdot (r' - r)} \langle S_{r'}^\alpha(0) S_r^\beta(t) \rangle e^{-i\omega t} dt$$

3.1.2 INS experiment at 4SEASONS in J-PARC

To measure the spin waves of HoMnO_3 , we used a 4SEASONS spectrometer in J-PARC. 4SEASONS is a direct geometry spectrometer and uses a thermal neutron chopper covering the range of 1-100 meV [Ref. 3.3]. In the direct geometry spectrometer, the momentum of the incident neutron is fixed. Thus, the neutrons with chosen incident energy are selected when it is passing through the chopper. The overall schematics for the 4SEASONS spectrometer is presented in Fig. 3.2.

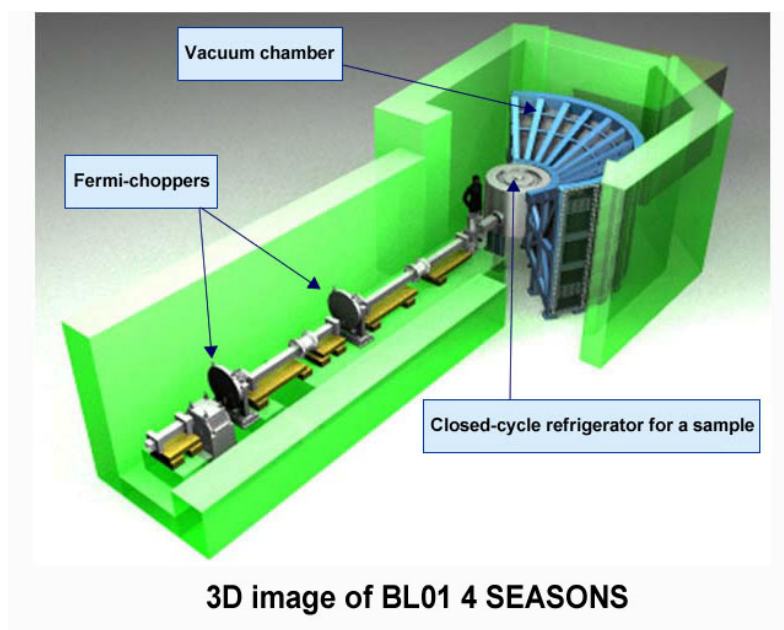


Figure 3.2 The schematics of the 4SEASONS spectrometer at J-PARC.

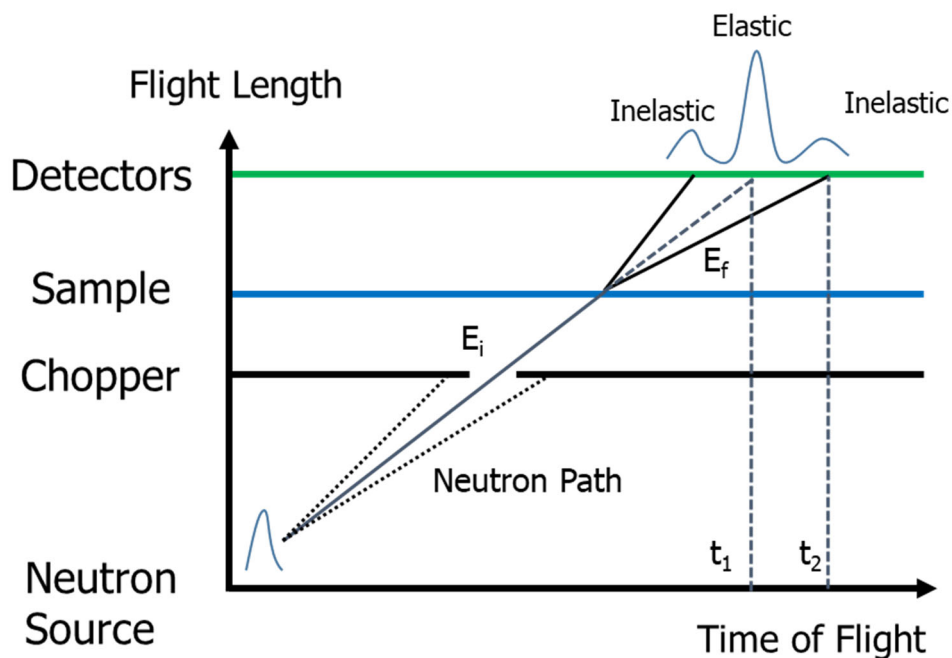


Figure 3.3 The schematics for describing the time-of-flight neutron scattering method.

4SEASONS spectrometer uses the so-called time-of-flight (ToF) method. Neutron beam is coming out from the source and the scattered by the sample. Detectors can accumulate the number of the neutron at non-zero energy transfers and momentum transfers. The ToF method is a robust way to obtain INS spectra for a wide range of momentum space. Once the neutron enters through the guide, the rotating chopper cuts the neutrons except for those with the desired velocity (i.e., energy). Then, the selected neutron is scattered by the sample. The two-dimensional detector array accumulates the number of scattered neutrons. Depending on the neutron flight's time and length, the neutron's energy or energy loss is determined. So, both elastic and inelastic scattering signals could be obtained.

Another technique, the so-called repetition rate multiplication (RRM) method,

was also used to efficiently get INS spectra [Ref. 3.4]. Based on this method, INS spectra at different incident neutron energy can be obtained simultaneously. As shown in Fig. 3.4, the chopper selects two energies within one rotation. The detectors can accumulate the signals since the number of neutrons arrived at different times. As illustrated in Fig. 3.4, there is no contamination from the other scattering process if the detectors' arrival time for the scattering of $E_{f(1)}$ is shorter than $t_{i(2)}$.

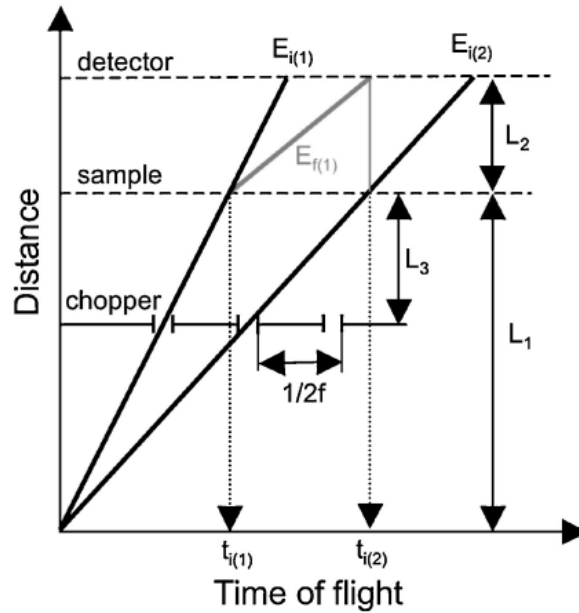


Figure 3.4 ToF diagram explaining the RRM method adapted from [Ref. 3.4].

Using the parameters for the 4SEASONS instrument, the multiple neutron energy regions can be determined if the chopper's frequency is fixed.

$$E_{i(1)} - E_{f(1)} = E_{i(1)} - A \left[2f \frac{L_2(L_1 - L_3)}{L_1} \right]^2$$

In our HoMnO_3 experiment, we fixed the chopper frequency at $f = 250$ Hz to obtain the

different data set for $E_i = 8.5, 12, 18, 30,$ and 60 meV.

For the INS experiment, we prepared a single crystal HoMnO_3 with a size of $5 \times 5 \times 22$ mm³ and a total mass of about 3 g. The sample was grown using an optical floating zone method by coworker Dr. H. Sim. The details for the sample growth can be found in [Ref. 3.5]. The single crystals are mounted in the holder made of almost pure aluminum to reduce background signals. The picture of the mounted sample at 4SEASONS is presented in Fig. 3.5.

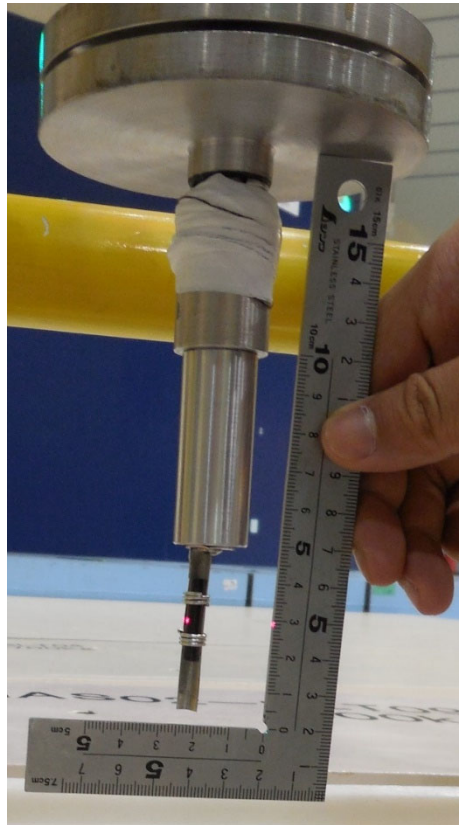


Figure 3.5 A photograph of the mounted HoMnO_3 sample at 4SEASONS.

Finally, we could carry out the INS experiment with the collaboration of coworkers Drs. K. Iida and K. Kamazawa. Before the actual INS experiment, we checked whether the sample alignment is correct or not. From the measurement of magnetic Bragg peaks, we could confirm that the sample was well-aligned, as shown in Fig. 3.6. After the confirmation, we conducted the INS experiment. For each scan, we had to choose the rotating angles, speeds, and steps for the sample, determining the data statistics and the region of allowed momentum transfers. INS results are explained in Chap. 4 in detail.

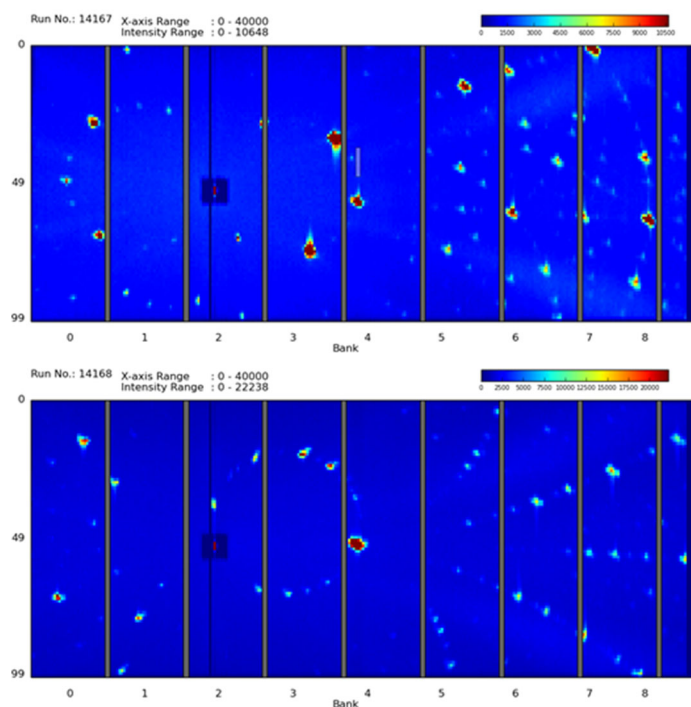


Figure 3.6 The Laue scattering patterns of HoMnO_3 . (Top) The $[220]$ plane. (Bottom) The $[002]$ plane.

3.1.3 IXS experiment at BL43LXU in SPring-8

We conducted an IXS experiment at BL43LXU [Ref. 3.6] in SPring-8 helped by coworkers Drs. A. Q. R. Baron and D. Ishikawa. The instrument at BL43LXU provides a high resolution of energy transfers and consists of several developed parts such as a 10-m scale spectrometer arm, analyzer crystals, and detector array. A schematic and a photograph of the beamline instrument are shown in Fig. 3.7.

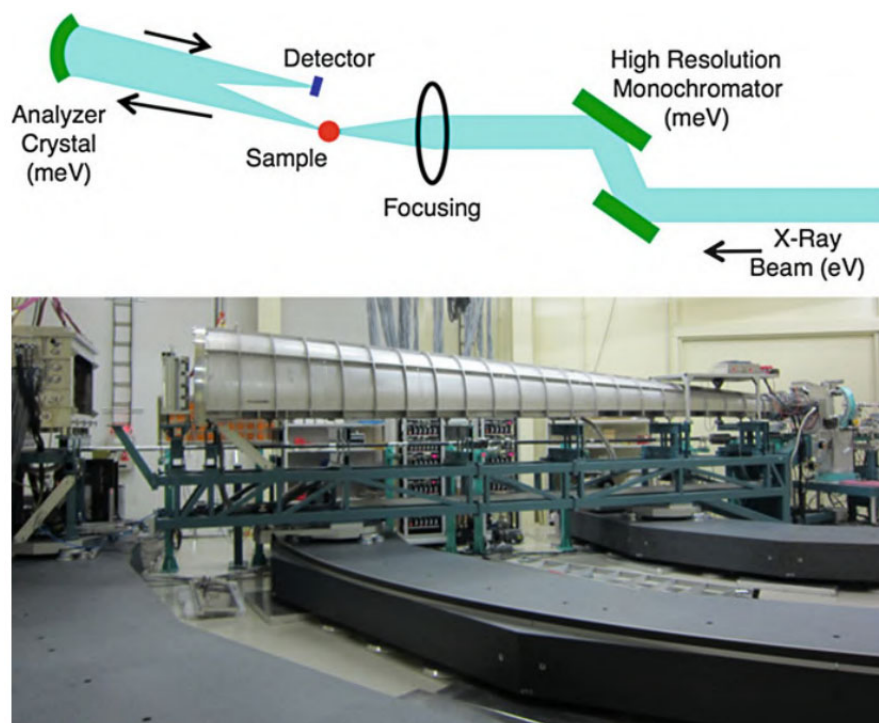


Figure 3.7 (Top) A schematic for the instrument. (Bottom) A photograph of the spectrometer arms, the analyzers, and the sample stage. The figure is adapted from [Ref. 3.7].

By using a high-resolution monochromator, the bandwidth of incident x-ray is reduced to

the meV energy scale. And it is scattered from the sample and passes through an analyzer and the spectrometer. The analyzer array is a type of two-dimensional array, and it is an efficient way to collect the IXS spectra at several different momentum transfers simultaneously [Ref. 3.7]. Before the actual experiment, we should first obtain the instrumental resolution. We measured the elastic peaks from the silicon with fixed x-ray energy of 21.75 keV. Backscattering using silicon (11 11 11) reflection was used to attain an energy resolution of 1.5 meV. The instrument resolution profiles at each detector are presented in Fig. 3.8.

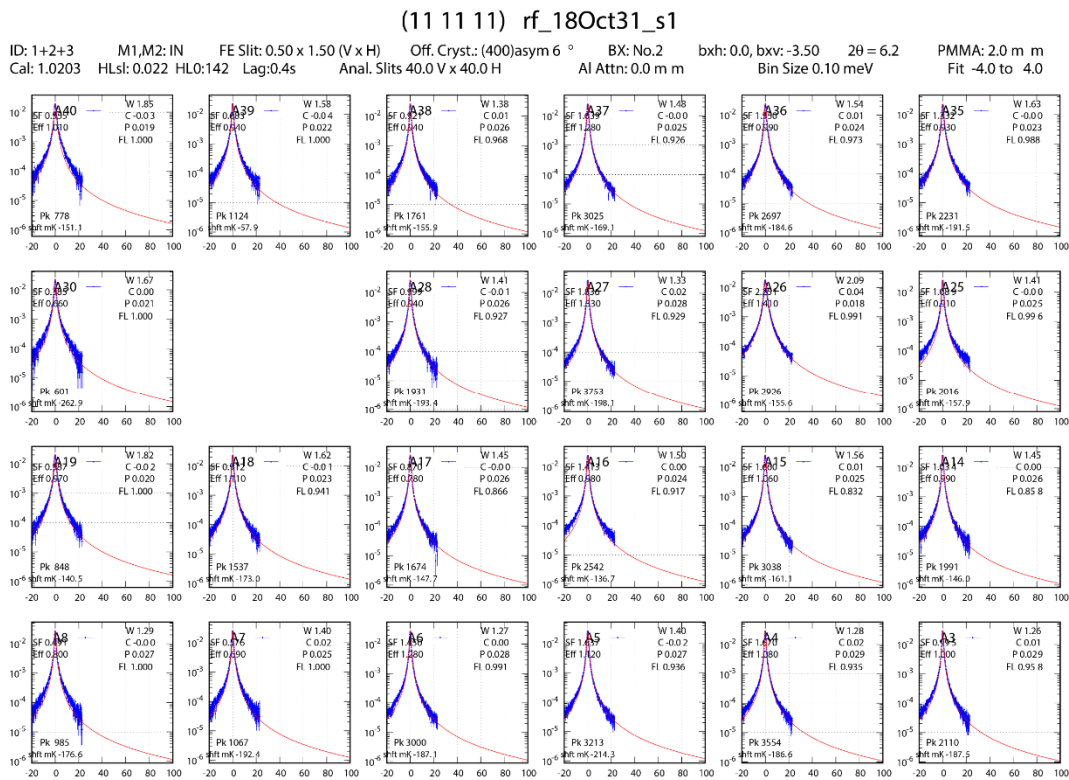


Figure 3.8 The measured Si (11 11 11) reflections at each detector, which describe the instrumental resolution of 1.5 meV.

As introduced in Sect. 3.1.1, the scattered cross-sections are proportional to the atomic form factor $f(\mathbf{Q})$. And the factor is dependent on the magnitude of the momentum transfer ($f(\mathbf{Q}) \propto |\mathbf{Q}|^2$). The orientation of a single crystal and the scattering geometry is important to get a visible spectrum. For the $\text{Cd}_2\text{Os}_2\text{O}_7$ IXS experiment, we mainly focused on the geometry that we can gather large intensity of the IXS spectra, mostly from the $[6\ 6\ 6]$, $[6\ 6\ 8]$, and $[8\ 6\ 6]$ Brillouin zones. The $[1\ 1\ 1]$ plane was aligned parallel to the incident x-ray beam. This geometry makes us obtain the large intensity of the IXS spectra. A photograph of the sample stage and the mounted sample are shown in Fig. 3.9.

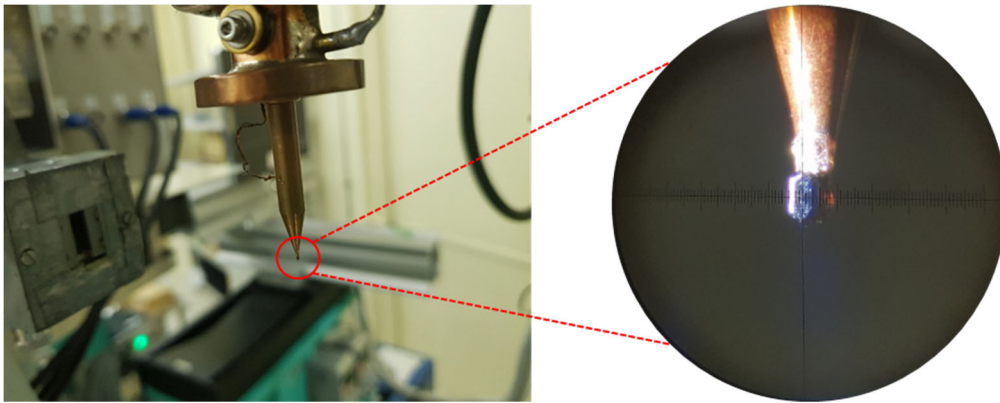


Figure 3.9 A photograph of (left) the sample stage and (right) the mounted sample. The surface of the sample shown in the figure is associated with the $[1\ 1\ 1]$ plane. The size of the sample is $0.7 \times 0.45 \times 0.5\ \text{mm}^3$ with a mass of about 0.9 mg.

To precisely set the sample geometry, we need to define the UB matrix. We can calculate the instrumental parameters of the four-circle-diffractometer from the UB matrix. It makes us obtain the IXS spectra at the desired momentum transfer and provides the possible range of momentum transfers within the instrumental environment. We used $(6\ 6$

6) and (8 4 4) Bragg peaks to define the UB matrix.

After the check all the conditions, we finally obtained the IXS spectra. The measurement procedure is as follows. First, we need to move the spectrometer arm for control two-theta to achieve the momentum transfer of interest. And then, we scan the incident beam's energy while holding the analyzer energy and position constant. One of the examples for the IXS data set is shown in Fig. 3.10. More detailed analyses and studies are explained in Chap. 5.

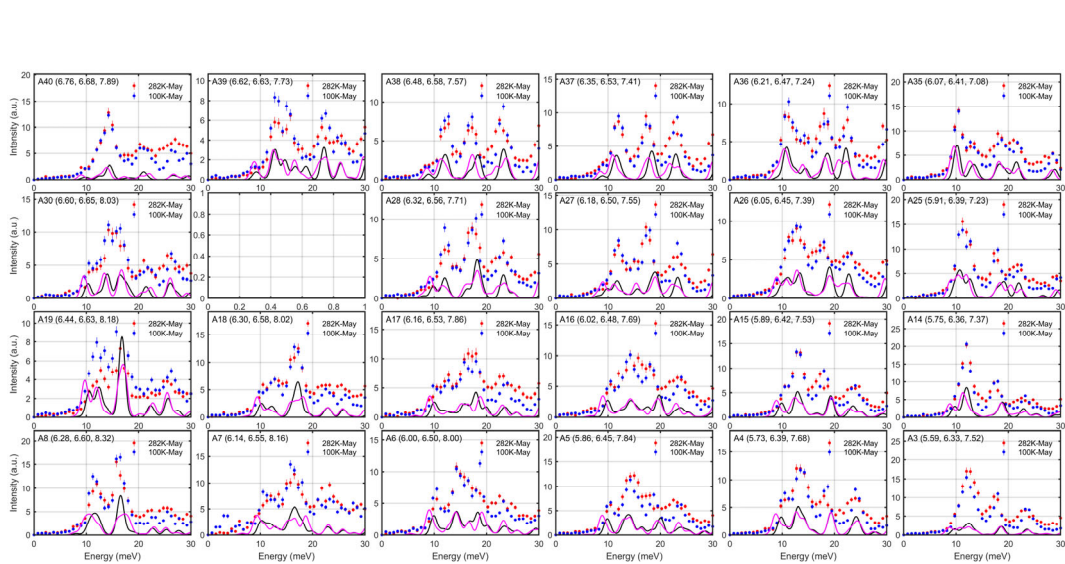


Figure 3.10 The IXS data set of $\text{Cd}_2\text{Os}_2\text{O}_7$ measured at BL43LXU spectrometer.

References

- [Ref. 3.1] S. Kang, K. Kim, B. H. Kim, J. Kim, K. I. Sim, J.-U. Lee, S. Lee, K. Park, S. Yun, T. Kim, A. Nag, A. Walters, M. Garcia-Fernandez, J. Li, L. Chapon, K.-J. Zhou, Y.-W. Son, J. H. Kim, H. Cheong, and J.-G. Park, *Nature* **583**, 785 (2020).
- [Ref. 3.2] G. L. Squires, in *Introduction to the Theory of Thermal Neutron Scattering* (Cambridge University Press, Cambridge, 2012), pp. 25–60.
- [Ref. 3.3] R. Kajimoto, M. Nakamura, Y. Inamura, F. Mizuno, K. Nakajima, S. Ohira-Kawamura, T. Yokoo, T. Nakatani, R. Maruyama, K. Soyama, K. Shibata, K. Suzuya, S. Sato, K. Aizawa, M. Arai, S. Wakimoto, M. Ishikado, S. Shamoto, M. Fujita, H. Hiraka, K. Ohoyama, K. Yamada, and C.-H. Lee, *J. Phys. Soc. Japan* **80**, SB025 (2011).
- [Ref. 3.4] M. Nakamura, R. Kajimoto, Y. Inamura, F. Mizuno, M. Fujita, T. Yokoo, and M. Arai, *J. Phys. Soc. Japan* **78**, 093002 (2009).
- [Ref. 3.5] H. Sim, *Structure Study on Multiferroic Materials: Hexagonal Manganites and $\text{PbFe}_{0.5}\text{Nb}_{0.5}\text{O}_3$* , Seoul National University, 2018.
- [Ref. 3.6] A. Q. R. Baron, *SPring-8 Inf. Newsl.* **15**, 14 (2010).
- [Ref. 3.7] A. Q. R. Baron, in *Synchrotron Light Sources and Free-Electron Lasers*, edited by E. J. Jaeschke, S. Khan, J. R. Schneider, and J. B. Hastings (Springer International Publishing, Cham, 2016), pp. 1643–1719.

Chapter 4

Renormalization of spin-excitations in triangular lattice antiferromagnet HoMnO_3

4.1 Hexagonal rare-earth manganites ($h\text{-RMnO}_3$)

Rare-earth manganites (RMnO_3) have several interesting properties to study, such as multiferroicity, noncollinear magnetic structure, frustration, and so on. Depending on the rare-earth ions, RMnO_3 has two types of crystal structure: one is an orthorhombic ($o\text{-RMnO}_3$), and the other is hexagonal geometry ($h\text{-RMnO}_3$). With $R = \text{Ho, Er, Y, and Lu}$, it has hexagonal symmetry and a 120° Néel order, which naturally introduces geometrical frustration to the system.

At the same time, $h\text{-RMnO}_3$ is a proper model system for studying two-dimensional triangular lattice antiferromagnet. Based on the crystal structure, Mn atoms are placed within the ab plane, and the planes are well separated from each other by rare-earth ions. Although the inter-plane exchange interactions exist, it is sometimes negligible since its order is about 0.2 % of intra-plane exchange interactions [Ref. 4.1]. Mn atoms are having super-exchange interactions with nearest-neighbor Mn atoms via oxygen atoms. A typical energy scale of the interaction is on an order of 10 meV, and the possible magnetic structures are plotted in Fig. 4.1.

In $h\text{-RMnO}_3$, there is another interesting issue of trimerization. The trimerization is a kind of lattice distortion that happened in the ab plane. The triangular lattice formed by Mn is contracted or expanded depending on the size of rare-earth ions.

This gives rise to the different exchange interactions, separating intra-trimer and inter-trimer exchange interactions.

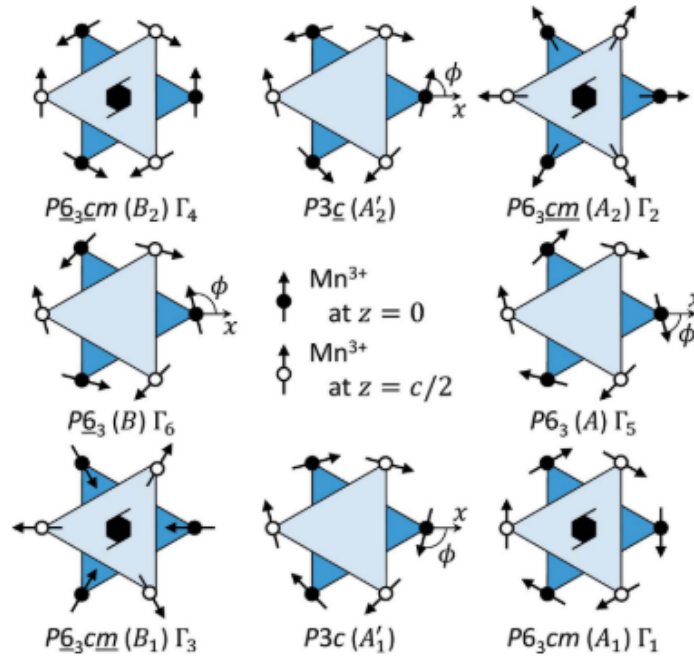


Figure 4.1 Magnetic structures in h - $RMnO_3$, adapted from [Ref. 4.2].

4.1.1 An ideal platform to study noncollinear magnetism

$HoMnO_3$ has been considered as a perfect platform to explore triangular lattice antiferromagnet without the trimerization effect and thus make analysis a lot simpler. The Mn^{3+} in $HoMnO_3$ mainly governs the magnetism, and the spin S is 2. The most characteristic feature in $HoMnO_3$ is that it has the smallest trimerization among h - $RMnO_3$ [Ref. 4.3]. If Mn position x is $1/3$, then it forms a perfect triangular lattice. Their neutron diffraction experiments revealed that Mn position x of $HoMnO_3$ is almost $1/3$ below 50 K, whereas x of $ScMnO_3$ or $YbMnO_3$ are apart from $1/3$. When the trimerization exists,

a minimum of four exchange interactions is needed to explain spin dynamics. So, HoMnO_3 has the merit of a study on magnetism in the ideal triangular lattice.

According to an inelastic neutron scattering (INS) study on HoMnO_3 , the nearest-neighbor exchange interaction J is found to be 2.44 meV, and the single-ion anisotropy D is obtained as 0.38 meV [Ref. 4.4]. The linear spin-wave theory (LSWT) results based on the fitted parameters J and D are in good agreement with the INS data. It is important to note that the Ho^{3+} ions also have magnetism. Based on the antiferromagnetic resonance and THz spectroscopy experiment, six crystal field excitations are observed, which is due to Ho^{3+} [Ref. 4.5, Ref. 4.6]. The energy scale of the crystal field excitations is about five meV. Although Ho has magnetism, it would take a small effect on magnetism for Mn^{3+} , especially in magnons, since the observed magnon modes for Mn^{3+} , which are placed from 10 to 20 meV, well separated from the crystal field excitations of Ho ions.

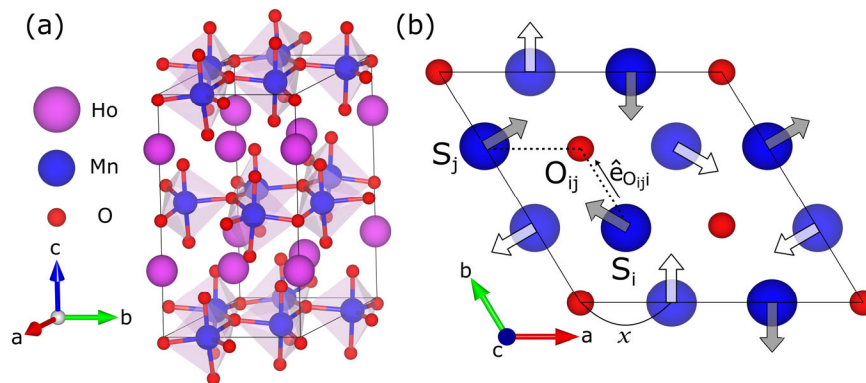


Figure 4.2 (a) Crystal and (b) magnetic structure of HoMnO_3 . Open (filled) arrows indicate the ordered magnetic moment at $z = 0$ ($z = 0.5$) plane. x indicates the Mn position.

4.1.2 Magnon-magnon interaction

As introduced in Chapter 2, magnon-magnon interaction exists intrinsically in noncollinear magnets. It is usually small to be observed by experiments. However, if the interaction is strong enough, anomalous features can appear in magnon dispersions. For example, $\text{Ba}_3\text{CoSb}_2\text{O}_9$, a spin 1/2 triangular lattice antiferromagnet, has a strong renormalization of magnon energies and a broadening of magnons due to the strong magnon-magnon interaction [Ref. 4.7, Ref. 4.8]. These features are usually enhanced in the spin 1/2 case as systemically investigated in theory [Ref. 4.9–Ref. 4.11].

Surprisingly, this kind of anomalous feature is also discovered in $h\text{-LuMnO}_3$, too [Ref. 4.1]. First, a roton-like minimum at the M point was observed in INS data, whereas the LSWT estimates a parabolic-like dispersion. Secondly, the magnon modes at 18 meV are flattened as compared to the expectation from the LSWT. Finally, there is an intrinsic linewidth broadening, and it is a momentum-dependent quantity. Based on these observations, it is expected to have a strong magnon-magnon interaction in HoMnO_3 as well. It also allows studying magnon-magnon interaction in a nearly ideal triangular lattice, making it easier to compare with the theoretical estimations.

4.1.3 Magnon-phonon coupling

As mentioned earlier, noncollinear magnets can have a coupling term between magnon and phonon operators. When this coupling is strong enough, magnons and phonons can repel each other, or they are hybridized with each other, producing magneto-elastic excitations [Ref. 4.12, Ref. 4.13]. The magneto-elastic excitations can be expressed by mixed magnon and phonon operators in the coupled Hamiltonian as formulated in Chapter 2. These terms are off-diagonal elements in the Hamiltonian matrix to modify the magnon or phonon energy. If these operators are combined as a cubic or higher-order term, it can also induce spontaneous decay of magneto-elastic excitations. Both theoretical and experimental examinations have been done in the INS study of (Y, Lu)MnO₃ [Ref. 4.12].

This kind of magnon-phonon coupling behavior can be found in other triangular lattice antiferromagnets, too. For example, both INS and IXS studies of LiCrO₂ found magneto-elastic excitations (or electromagnon) [Ref. 4.14]. In addition, CuCrO₂ also has similar excitations at around 12.5 meV based on the INS experiment [Ref. 4.15]. Both LiCrO₂ and CuCrO₂ are delafossite compounds with magnetic Cr³⁺ ions of $S = 3/2$. The magnetic structure is a helix structure with $\mathbf{Q} = (0.329, 0.329, 0)$ for CuCrO₂ and $\mathbf{Q} = (1/3, 1/3, 0)$ and $(-2/3, 1/3, 1/2)$ for LiCrO₂, which shows the noncollinear 120° ordering state in triangular lattice antiferromagnet. On the other hand, *h*-LuFeO₃ has no similar features originating from the magnon-phonon coupling. Although it has the same crystal and magnetic structure as *h*-RMnO₃, magnon-phonon coupling seems to be suppressed in *h*-LuFeO₃. The possible reason might be less overlap between magnon and phonon than *h*-RMnO₃, or large spin value $S = 5/2$, which suppress magnon-magnon interaction.

4.2 Spin excitations in HoMnO₃

4.2.1 INS data and fitting by using LSWT

As discussed in Section 4.1, HoMnO₃ is a promising material that can possess magnon-magnon interaction and magnon-phonon coupling. It is also a nearly ideal triangular lattice antiferromagnet. Therefore, it is an excellent platform to examine the strength of magnon-magnon or magnon-phonon interaction. We conducted INS experiments at 4SEASONS beamline of J-PARC using the time-of-flight neutron scattering technique to explore this issue.

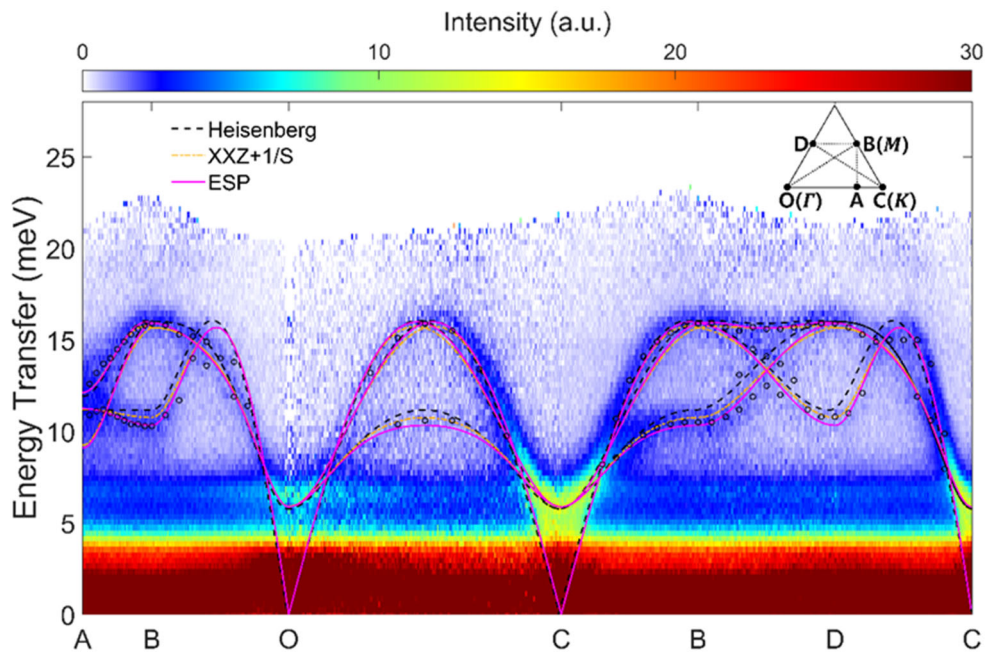


Figure 4.3 INS data for HoMnO₃ taken at 4 K. The energy of the incident neutron is 30 meV. Three model calculations are presented to compare the experimental data.

We used the Heisenberg model, and XXZ model with $1/S$ expansions, and the ESP model. (Details about models are described in the text) Black circles are fitted positions from INS spectra at each Q position. The inset indicates the Brillouin zones and the labels for the momentum positions.

INS data are shown in Fig. 4.3. The INS data are summed from $L = -3$ to 3 to have enough statistics of intensity. Since the interlayer exchange interaction is negligible here, there is no L dependency in data along the HK plane, which is the region of interest to us. There are clear three magnon modes placed from 10 to 18 meV. And several dispersion-less crystal field excitations exist at 1.7, 3.2, and 6.7 meV based on multiple peak fitting results. These energies are the same as found in other studies [Ref. 4.5, Ref. 4.6]. To explain the data, we calculated magnon dispersion using the conventional Heisenberg model with LSWT.

$$H_{\text{Heis}} = J \sum_{\langle ij \rangle} \mathbf{S}_i \cdot \mathbf{S}_j + D \sum_i (S_i^z)^2$$

J and D are nearest-neighbor exchange interaction and single-ion anisotropy parameters. Based on the best fit shown in Fig. 4.3, we could obtain $J = 2.44$ meV and $D = 0.38$ meV, which is the same as the previous INS study [Ref. 4.4].

4.2.2 Anomalous features in magnon dispersion

Despite the general match between experimental data and LSWT calculation, there are still some distinct features. The magnon mode at 12 meV along the AB direction have downward curvature. Also, at the B point, the energy was shifted by about 0.8 meV. In contrast, the LSWT calculations expect flat mode along the AB direction. This renormalization of magnon energy is not produced by adding further neighbor exchange interaction or exchange anisotropy, as shown in Fig. 4.4. This kind of renormalization in magnon energy can be considered a result of magnon-magnon interaction or magnon-phonon coupling. Both of these interactions should be included in the spin dynamics to explain the anomalous features.

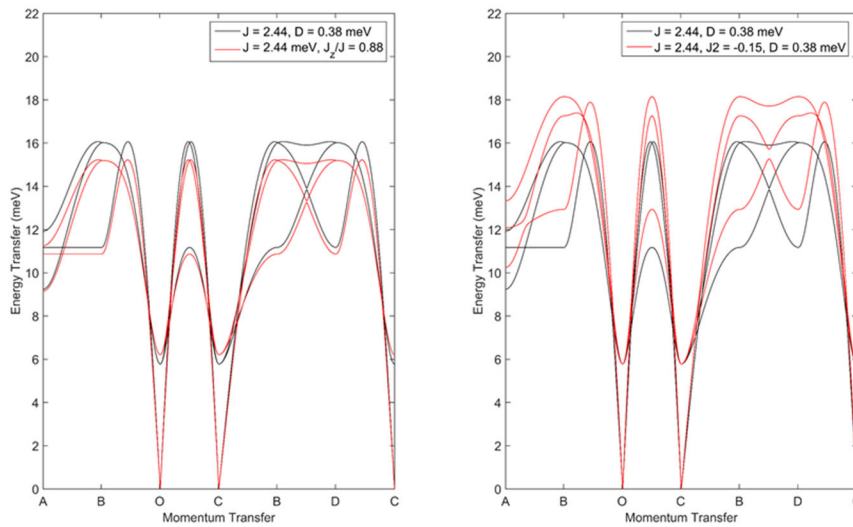


Figure 4.4 Comparing results between the simple Heisenberg model and the model adding (left) exchange anisotropy or (right) next nearest-neighbor exchange interactions. None of them explain the downward curvature along the AB direction.

Furthermore, one can see the blurred small intensity of the INS spectra from 20 to 30 meV, especially at B and D points, as shown in the color plot in Fig. 4.5. One can also see the non-negligible intensity (although the error bars are a bit large) at B, middle of O and C, and D points as plotted in constant E cut in Fig. 4.5. This can be regarded as a continuum state of magnons due to spontaneous decay. So, it is possible to have a visible magnon-magnon interaction in HoMnO_3 as similar to LuMnO_3 .

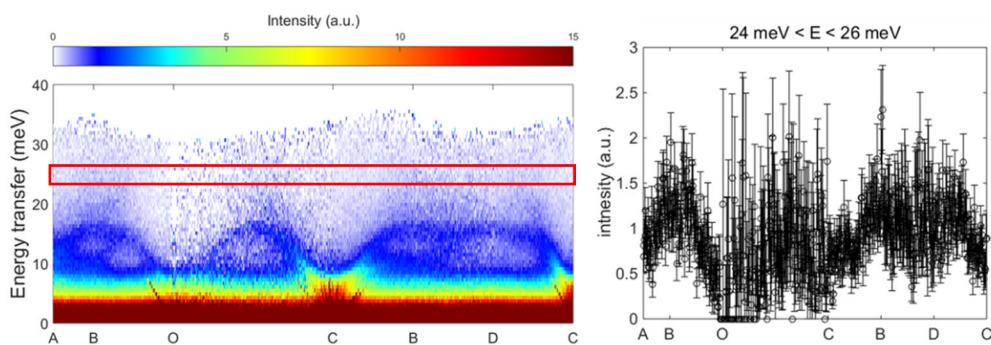


Figure 4.5 (Left) INS data taken at 4 K. The energy of the incident neutron is 60 meV. The momentum positions are the same as Fig. 4.3. The red box indicates the integration range for constant E cut. **(Right)** The integrated intensity of energy ranges from 24 to 26 meV.

4.3 Model fitting using quasiparticle interactions

4.3.1 XXZ+1/S expansion: magnon-magnon interaction

To theoretically investigate magnon-magnon interaction in HoMnO₃, we adapted the Heisenberg XXZ model with 1/S expansion, as described in [Ref. 4.10].

$$H_{\text{XXZ}+1/S} = J \sum_{\langle ij \rangle} \left[S_i^x S_j^x + S_i^y S_j^y + \Delta S_i^z S_j^z \right] + H_3$$

Here, the $\Delta = J_z/J$ indicates the exchange anisotropy (or two-ion anisotropy). When $\Delta < 1$, it can be considered as an easy-plane anisotropy that makes the 120° ordering state is stable in a triangular lattice antiferromagnet. The H_3 is the cubic term related to magnon-magnon interaction, as outlined in Chapter 2.

As shown in Fig. 4.3, the XXZ model can reproduce the downward curvature along the AB direction. To obtain the best fit to overall magnon energies, we used $J = 2.7$ meV and $\Delta = 0.88$. In this model, Heisenberg exchange interaction $J = 2.7$ meV is larger than those used in the above LSWT calculations $J = 2.44$ meV. This is because the magnon-magnon interaction term reduces the magnon energies. We need to consider the larger J to match the experimental results.

4.3.2 ESP model: magnon-phonon coupling

As mentioned in Section 4.1.3, the magnon-phonon coupling can also induce magnon energy renormalization. To include magnon-phonon coupling in spin Hamiltonian, we adapted the ESP model [Ref. 4.16, Ref. 4.17] as introduced in Section 2. This model

assumes a coupling between a single magnon and one dispersion-less optical phonon branch.

$$H_{\text{ESP}} = J \left[\sum_{\langle ij \rangle} \mathbf{S}_i \cdot \mathbf{S}_j - cS^2 \sum_i \mathbf{F}_i^2 \right] + D \sum_i (S_i^z)^2$$

$$\mathbf{F}_i = \sum_j \hat{e}_{O_{ij}} (\mathbf{S}_i \cdot \mathbf{S}_j) / S^2$$

Here, c is a dimension-less spin-phonon coupling constant defined as $c = \alpha^2 J S^2 / 2K$. K is an elastic constant (unit: energy), and α is an exchange-striction coefficient (unit: dimension-less) defined as $\alpha = \frac{d}{J} \frac{\partial J}{\partial r}$ and d is a bond distance between Mn and O. $\hat{e}_{O_{ij}}$ is the unit vector pointing from the Mn site j to the O site O_{ij} as shown in Fig. 4.2(b).

The ESP model also succeeded in reproducing the downward curvature of magnon modes along the AB direction. Based on the best fit, we could obtain $J = 2.53$ meV, $D = 0.38$ meV, and $c = 1/12$. J and D parameters seem to be reasonable value in comparison with the LSWT calculations. And $c = 1/12$ is also safe since the theoretical results estimate that if c is below $1/8$, then the 120° ordering state is stable.

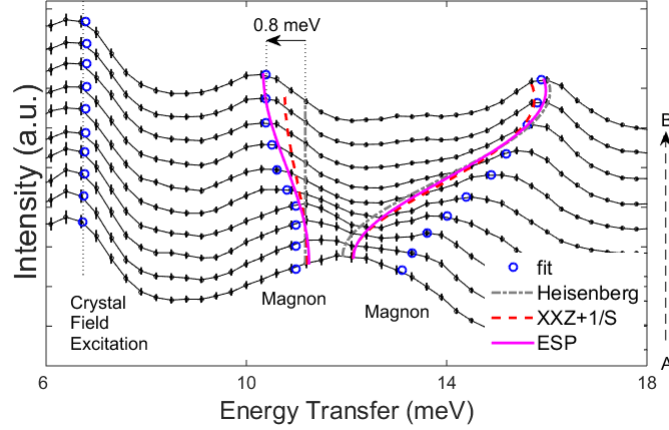


Figure 4.6 (Left) INS spectra along the AB direction. The calculated magnon energies using three different models are plotted. Blue circles indicate the fitted peak positions of each spectrum.

Figure 4.6 represents the detailed constant Q cuts and the theoretical calculations' results along the AB direction. Based on these analyses, we can reproduce the anomalous features using the Hamiltonian, including both magnon-magnon interaction and magnon-phonon coupling.

We also compare INS spectra's intensity at the B point with the calculated scattering cross-sections from the H_{XXZ} and H_{ESP} , as shown in Fig. 4.7. As our data show good agreement with the calculated intensity by the ESP model, we think that the ESP model explains well the spin dynamics in HoMnO_3 . Especially, the intensity ratio between two magnon peaks located at 10 and 16 meV is only reproduced by the ESP model. Besides, the overall integrated intensity is also well matched with the ESP model. The INS data's integrated intensity is obtained from the summation of two or three fitted peaks at each Q position. All calculated intensity shown in Fig. 4.7 is scaled by the same factor 0.6.

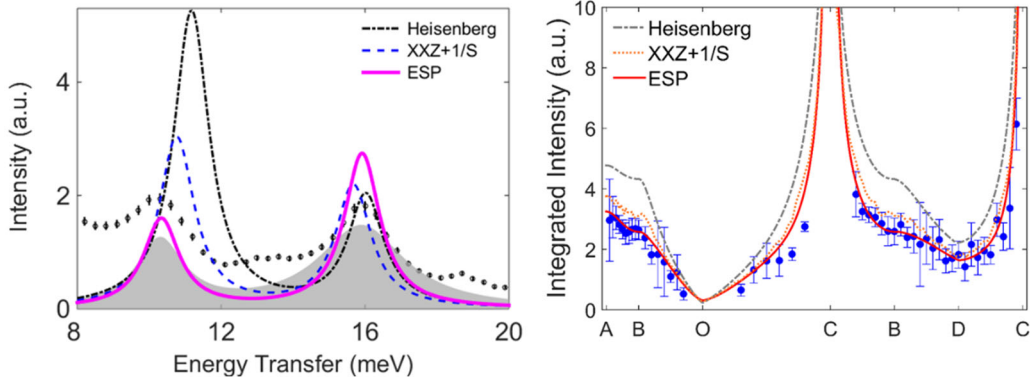


Figure 4.7 (Left) INS spectrum at the B point and the calculated intensity using three different models. The gray shaded area indicates the fitted magnon peaks without background signals. **(Right)** The integrated intensity along the high symmetric path in momentum space. The calculated intensity from three models is compared with the experimental data.

4.4 Discussion and summary

4.4.1 Dominant interaction in HoMnO_3

According to the agreement between experiments and calculations, the magnon-phonon coupling can be considered as the dominant interaction driving magnon's renormalization. One of the reasons is that the obtained spin-phonon coupling constant c is stronger than (Y, Lu) MnO_3 [Ref. 4.12]. Since they give the value of exchange-striction coefficient α , we need to convert c to α for exact comparison. As we defined earlier, $c = \alpha^2 J S^2 / 2K$ and if we know the elastic constant K , we can convert it to exchange-striction coefficient. Based

on the ultrasonic wave experiments [Ref. 4.18, Ref. 4.19] and DFT calculations for YMnO_3 [Ref. 4.12], we could estimate that K is approximately 10 eV. It gives that $\alpha_{\text{Ho}} = 12.8$, which is larger than $\alpha_{\text{Y,Lu}} = 8$ [Ref. 4.12]. The other evidence is that the observed diffuse signal was placed at around 18 meV. This might be the magneto-elastic excitations resulting from the hybridization of magnons and phonons in HoMnO_3 . This kind of magneto-elastic excitations is similar to the observed one in CuCrO_2 [Ref. 4.15] and (Y, Lu) MnO_3 [Ref. 4.12].

We also found some evidence for the suppression of magnon-magnon interaction. First, the FWHM of magnon peaks located at 16 meV for the B point is found to be 0.85 meV in HoMnO_3 , which is much narrower than the observed FWHM of 3.5 meV in LuMnO_3 [Ref. 4.1]. Since the FWHM of magnon is directly related to the magnon lifetime, the broader peaks indicate a short lifetime due to the decay. Based on this fact, the magnon-magnon interaction in HoMnO_3 is smaller than LuMnO_3 . Another evidence is that we observed the weak two-magnon continuum signals. In the XXZ model, the continuum intensity at 25 meV energy transfer is expected to be 3.4% of intensity for the single-magnon; which is too small to be visualized in data. As shown in Fig. 4.5, the spectral weight for the energy transfer of 25 meV shows the weak intensity. This can be understood by theoretical results that estimate the suppression of magnon decay when the anisotropy is large. In theory, if the anisotropy $\Delta < 0.92$, then the magnon decay is prohibited [Ref. 4.10]. This is the consistent result with the experimental observations.

4.4.2 Summary

We have investigated the magnon-magnon interaction and magnon-phonon coupling in HoMnO_3 using INS experiments. Since HoMnO_3 realizes an ideal two-dimensional triangular lattice, we could compare the INS data with the theoretical calculations of three different models. Using the Heisenberg model, the XXZ model with $1/S$ expansions, and the ESP model, it can quantitatively compare the effects of magnon-magnon interaction or magnon-phonon coupling. The anomalous downward curvature along the AB direction can be explained by both the XXZ and ESP models. However, based on the comparison between the calculated intensity and the experimental data, we think that the ESP model works better to interpret the data. Also, we quantified the exchange-striction coefficient α and found that HoMnO_3 has a larger value of $\alpha_{\text{Ho}} = 12.8$ than $(\text{Y, Lu})\text{MnO}_3$. Based on all the analysis, we can conclude that in HoMnO_3 , the magnon-phonon coupling is highly dominant, whereas the magnon-magnon interaction is suppressed.

References

- [Ref. 4.1] J. Oh, M. D. Le, J. Jeong, J. Lee, H. Woo, W.-Y. Song, T. G. Perring, W. J. L. Buyers, S.-W. Cheong, and J.-G. Park, *Phys. Rev. Lett.* **111**, 257202 (2013).
- [Ref. 4.2] H. Sim, J. Oh, J. Jeong, M. D. Le, and J.-G. Park, *Acta Crystallogr. Sect. B Struct. Sci. Cryst. Eng. Mater.* **72**, 3 (2016).
- [Ref. 4.3] X. Fabrèges, S. Petit, I. Mirebeau, S. Pailhès, L. Pinsard, A. Forget, M. T. Fernandez-Diaz, and F. Porcher, *Phys. Rev. Lett.* **103**, 067204 (2009).
- [Ref. 4.4] O. P. Vajk, M. Kenzelmann, J. W. Lynn, S. B. Kim, and S.-W. Cheong, *Phys. Rev. Lett.* **94**, 087601 (2005).
- [Ref. 4.5] J. Liu, Y. Gallais, M.-A. Measson, A. Sacuto, S. W. Cheong, and M. Cazayous, *Phys. Rev. B* **95**, 195104 (2017).
- [Ref. 4.6] X. Fabrèges, S. Petit, J.-B. Brubach, P. Roy, M. Deutsch, A. Ivanov, L. Pinsard-Gaudart, V. Simonet, R. Ballou, and S. de Brion, *Phys. Rev. B* **100**, 094437 (2019).
- [Ref. 4.7] J. Ma, Y. Kamiya, T. Hong, H. B. Cao, G. Ehlers, W. Tian, C. D. Batista, Z. L. Dun, H. D. Zhou, and M. Matsuda, *Phys. Rev. Lett.* **116**, 087201 (2016).
- [Ref. 4.8] S. Ito, N. Kurita, H. Tanaka, S. Ohira-Kawamura, K. Nakajima, S. Itoh, K. Kuwahara, and K. Kakurai, *Nat. Commun.* **8**, 235 (2017).
- [Ref. 4.9] A. L. Chernyshev and M. E. Zhitomirsky, *Phys. Rev. Lett.* **97**, 207202 (2006).

- [Ref. 4.10] A. L. Chernyshev and M. E. Zhitomirsky, Phys. Rev. B **79**, 144416 (2009).
- [Ref. 4.11] M. E. Zhitomirsky and A. L. Chernyshev, Rev. Mod. Phys. **85**, 219 (2013).
- [Ref. 4.12] J. Oh, M. D. Le, H.-H. Nahm, H. Sim, J. Jeong, T. G. Perring, H. Woo, K. Nakajima, S. Ohira-Kawamura, Z. Yamani, Y. Yoshida, H. Eisaki, S. W. Cheong, A. L. Chernyshev, and J.-G. Park, Nat. Commun. **7**, 13146 (2016).
- [Ref. 4.13] K. Park, J. Oh, K. H. Lee, J. C. Leiner, H. Sim, H. Nahm, T. Kim, J. Jeong, D. Ishikawa, A. Q. R. Baron, and J. Park, Phys. Rev. B **102**, 085110 (2020).
- [Ref. 4.14] S. Tóth, B. Wehinger, K. Rolfs, T. Birol, U. Stuhr, H. Takatsu, K. Kimura, T. Kimura, H. M. Rønnow, and C. Rüegg, Nat. Commun. **7**, 13547 (2016).
- [Ref. 4.15] K. Park, J. Oh, J. C. Leiner, J. Jeong, K. C. Rule, M. D. Le, and J.-G. Park, Phys. Rev. B **94**, 104421 (2016).
- [Ref. 4.16] D. L. Bergman, R. Shindou, G. A. Fiete, and L. Balents, Phys. Rev. B **74**, 134409 (2006).
- [Ref. 4.17] F. Wang and A. Vishwanath, Phys. Rev. Lett. **100**, 077201 (2008).
- [Ref. 4.18] M. Poirier, F. Laliberté, L. Pinsard-Gaudart, and A. Revcolevschi, Phys. Rev. B **76**, 174426 (2007).
- [Ref. 4.19] M. Poirier, J. C. Lemyre, P.-O. Lahaie, L. Pinsard-Gaudart, and A. Revcolevschi, Phys. Rev. B **83**, 054418 (2011).

Chapter 5

Spin-orbit coupling effect on spin-phonon coupling in $\text{Cd}_2\text{Os}_2\text{O}_7$

5.1 $5d$ pyrochlore oxide $\text{Cd}_2\text{Os}_2\text{O}_7$

5.1.1 Properties related to spin-orbit coupling

To understand various strong-correlation phenomena such as Weyl semimetals and topological insulators [Ref. 5.1], understanding SOC is essential. In transition metals, $4d$ and $5d$ transition metal compounds generally have relatively strong SOC compared to $3d$ transition metal compounds, and the varying strength of these SOC can modify both the electronic and magnetic ground states of the materials. For instance, if the spin and orbital degrees of freedom are strongly coupled, then a spin-orbital entangled state is the actual ground state, often found in iridates [Ref. 5.2].

$\text{Cd}_2\text{Os}_2\text{O}_7$ is one of the candidates having strong SOC due to the presence of Os atom. The crystal structure of $\text{Cd}_2\text{Os}_2\text{O}_7$ is a pyrochlore lattice with the space group of $Fd\bar{3}m$ with the lattice parameter $a = 10.1604 \text{ \AA}$ [Ref. 5.3]. The electronic configuration of an Os atom is $5d^3$ corresponding to spin $S = 3/2$ and orbital angular momentum $L = 0$. It is noteworthy that the electronic ground state of $\text{Cd}_2\text{Os}_2\text{O}_7$ is $S = 3/2$, which assumes that the SOC does not affect the ground state. According to a previous study on resonant inelastic X-ray scattering (RIXS) [Ref. 5.4], no spin-orbit excitons originated from the transition between $j_{\text{eff}}=1/2$ and $3/2$ state. It implies that the electronic ground state is not the spin-

orbital entangled state. Therefore, SOC is negligible in the electronic ground state. Meanwhile, a recent RIXS study suggested that $\text{Cd}_2\text{Os}_2\text{O}_7$ may exhibit some $5d^4$ electron configuration characters [Ref. 5.5]. Furthermore, an earlier theoretical study found a trigonal distortion in a OsO_6 octahedron, and it induces a sizable single-ion anisotropy (SIA) [Ref. 5.6].

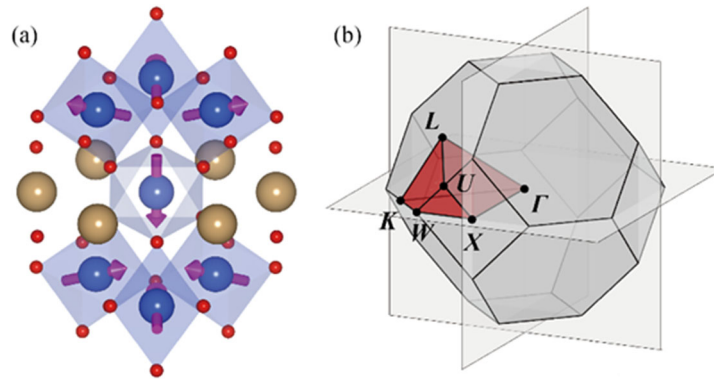


Figure 5.1 (a) The crystal and magnetic structures of $\text{Cd}_2\text{Os}_2\text{O}_7$. The arrows indicate the magnetic moment ordering. (b) The first Brillouin zone of the pyrochlore lattice.

In $\text{Cd}_2\text{Os}_2\text{O}_7$, mainly the Os^{5+} ion is responsible for magnetism since the Cd^{2+} ion is non-magnetic. The magnetic structure of $\text{Cd}_2\text{Os}_2\text{O}_7$ is the all-in-all-out (AIAO) state [Ref. 5.4, Ref. 5.7] with the Néel temperature $T_N = 227$ K, as shown in Fig. 5.1(a). Interestingly, the electronic band is also changed from metal to insulator at the magnetic ordering temperature, i.e., the MIT occurs. The MIT in $\text{Cd}_2\text{Os}_2\text{O}_7$ has been studied for a long time from the first discovery [Ref. 5.8]. People debate the origin of the MIT, and a Slater-type

transition was firmly suggested [Ref. 5.9]. The more careful examinations find out that the possible mechanism can be a Lifshitz-type MIT [Ref. 5.10,Ref. 5.11].

So far, theoretical and experimental studies have been conducted on the AIAO ordering state in $\text{Cd}_2\text{Os}_2\text{O}_7$. Some theoretical results using first-principle and many-body quantum-chemistry calculations suggest that the AIAO ordering state becomes stable due to a large SIA that is induced by strong SOC [Ref. 5.6,Ref. 5.12]. N. A. Bogdanov et al. found that a trigonal distortion in an OsO_6 octahedron causes an easy-axis anisotropy of 6.8 meV. The direction of the easy-axis is the local [111] axis. From the experimental results, it was also confirmed that the anisotropy value is comparable to the nearest neighbor Heisenberg exchange interaction. Based on the observation of two-magnon scattering in Raman spectroscopy, T. M. H. Nguyen et al. revealed that SIA is a similar energy scale with the Heisenberg exchange interaction [Ref. 5.13]. In addition, the RIXS studies revealed that the spin-flip excitations exist in the spectrum, and the large SIA is required to explain the spectrum [Ref. 5.4,Ref. 5.5]. The spin Hamiltonian can be expressed as

$$\mathbf{H}_{\text{spin}} = J \sum_{\langle ij \rangle} \mathbf{S}_i \cdot \mathbf{S}_j + \sum_{\langle ij \rangle} \mathbf{D}_{ij} \cdot \mathbf{S}_i \times \mathbf{S}_j + K \sum_i (\mathbf{S}_i \cdot \mathbf{n}_i)^2,$$

where J , \mathbf{D} , and K are the Heisenberg interaction, the Dzyaloshinskii-Moriya interaction, and the SIA. The \mathbf{n}_i is a unit vector pointing toward the local [111] axis. According to the best fit for the two-magnon continuum observed in Raman spectra, $J = 5.1$, $K = -5.3$ meV, and $\mathbf{D} = \sim 1/3$ of J were obtained [Ref. 5.13].

5.1.2 Unconventional spin-phonon coupling

The observed large SIA in $\text{Cd}_2\text{Os}_2\text{O}_7$ is suggested as an essential ingredient for the spin-phonon (SP) coupling in $\text{Cd}_2\text{Os}_2\text{O}_7$. Using IR optical spectroscopy, a strong renormalization of IR-active phonons is observed [Ref. 5.14]. This renormalization occurs at the magnetic transition temperature. The renormalization originates from either magnetic ordering or electronic band change. C. H. Sohn et al. argued that the primary mechanism for the SP coupling is the large SIA. Based on their crystal electric field calculations, the crystal field change from each phonon mode can simulate the energy renormalization for corresponding phonon modes. This type of SP coupling was first reported by C. H. Sohn et al. [Ref. 5.14], and it is considered as an unconventional SP coupling. A well-known mechanism of usual SP coupling can be explained in the form of the exchange-striction [Ref. 5.15], magneto-striction [Ref. 5.16, Ref. 5.17], or magnon-phonon coupling [Ref. 5.18–Ref. 5.21]. In $\text{Cd}_2\text{Os}_2\text{O}_7$, the SIA is the main driving force for the SP coupling, which is a distinctive origin.

Since the SP coupling is mediated by the large SIA, SOC should have an essential role in the SP coupling of $\text{Cd}_2\text{Os}_2\text{O}_7$. Because the SIA is highly related to the effect of SOC. However, most studies on effect of SOC have focused on magnetism or electronic bands. The relationship between SOC and lattice dynamics in $5d$ transition metal oxides is rarely studied. And there are limitations to getting momentum dependence on phonons from optical spectroscopy. Therefore, we investigated phonons in $\text{Cd}_2\text{Os}_2\text{O}_7$ over the wide range of momentum space using IXS, which can provide further information on phonons. Furthermore, in density-functional theory (DFT), we can vary strength of SOC and the

electron correlation U . Therefore, it is interesting to conduct a theoretical study on the effect of SOC on the phonon modes, and compare the results with the experimental data.

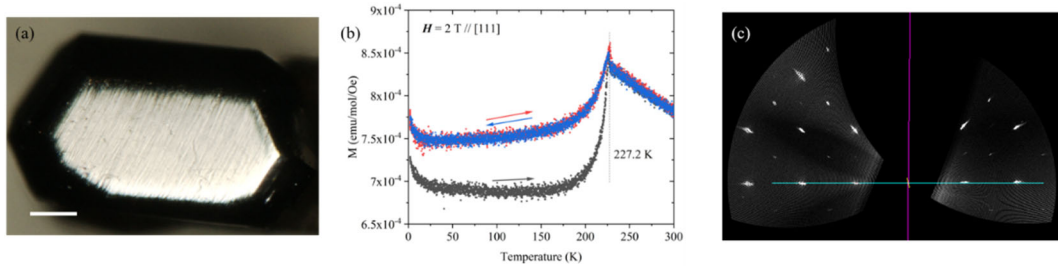


Figure 5.2 (a) The photograph of the single crystal used in the IXS experiment. The white scale bar indicates a length of 100 μm . (b) The magnetic susceptibility of $\text{Cd}_2\text{Os}_2\text{O}_7$ single crystal as a function of temperature. (c) The single-crystal X-ray diffraction result for the $[H0L]$ plane.

5.2 IXS experiments and DFT calculations

5.2.1 Renormalization of phonons

High-quality $\text{Cd}_2\text{Os}_2\text{O}_7$ single crystals were synthesized by the group of Prof. Z. Hiroi at Institute for Solid State Physics, University of Tokyo, Japan. They used the chemical transport method to prepare the single crystals [Ref. 5.11]. Prior to our X-ray experiments, we characterized every crystal through single-crystal X-ray diffraction and magnetic susceptibility measurements, as shown in Fig. 5.2. The magnetic ordering temperature (T_N) observed in the susceptibility data is ~ 227 K, which is the same as that reported in a previous study [Ref. 5.11]. The IXS experiments were performed with Dr. D. Ishikawa and

Dr. A.Q.R. Baron at the Quantum Nano Dynamics beamline, BL43LXU [Ref. 5.22], of the RIKEN SPring-8 Center. The details of the IXS experiments are summarized in Chap. 3. In this experiment, we fixed the X-ray energy to 21.75 keV and used a two-dimensional array of analyzers to gain the IXS spectra at different momentum positions simultaneously. The energy resolution of the spectra is found to be approximately 1.5 meV. We used slits of dimensions 40×40 mm and the scattered beam path was 8.9 m from the sample position, which corresponds to a momentum resolution of $(0.048, 0.011, 0.049) \text{ \AA}^{-1}$. Further, we also verified the $(6\ 6\ 6)$ Bragg peak and confirmed that the FWHM of the peak is 0.04° , which demonstrates high quality of the sample.

Based on the geometry of the sample alignment, we could access the momentum space mainly in the $(6\ 6\ 6)$, $(6\ 6\ 8)$, and $(8\ 6\ 6)$ Brillouin zones. To investigate the SP coupling, we collected IXS spectra at 282 and 100 K, which is well above and below the T_N . The phonon spectra taken at four \mathbf{Q} points (X, W, K, and U), which is corresponding to the zone boundaries, are shown in Fig. 5.3(a-d) as examples. All the spectra were measured at 100 K. We observed acoustic phonon modes and several optical phonon modes at energy transfers of up to 35 meV. The signals above the energy transfer of 35 meV are sufficiently low to recognize phonons. This can be understood that since the IXS cross-sections are inversely proportional to energy, the intensity of phonons for higher energies is required much longer acquisition times than we consumed in the experiments.

To compare the experimental results, we performed DFT calculations. The solid red lines in Fig. 5.3 represent the calculated IXS cross-sections based on the DFT calculation. For an appropriate comparison of the experimental results, we considered the

intensity corrections from the Bose factor and the Debye–Waller factor. The linewidth used in the convolution of the calculated spectra is fixed at 1.6 meV, which is similar to the instrumental resolution. As shown in Fig. 5.3, the theoretical calculations are in good agreement with the observed IXS spectra. Based on the best fit, we obtained electron correlation energy $U = 2.0$ eV and the scaling factor for SOC of 1.0. These values are consistent with the values reported in the literature [Ref. 5.10, Ref. 5.12]. The phonon dispersion curves are plotted in Fig. 5.3(e), which generally provides a good comparison between calculations and experiments.

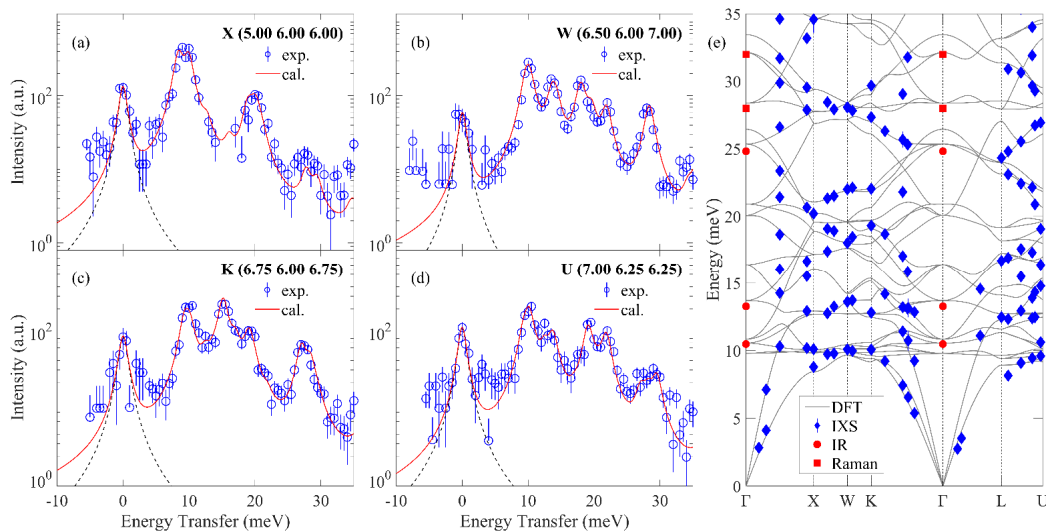


Figure 5.3 (a–d) The IXS spectra taken at four Q positions as labeled. All spectra were obtained at 100 K. The black dashed line is the instrumental resolution profile of the elastic peak. **(e)** Phonon dispersions obtained using IXS and the DFT calculations. Red circles and squares represent the observed phonons from Raman and IR spectroscopies, adapted from [Ref. 5.13] and [Ref. 5.14].

We observed energy shifts for some optical phonons from the IXS spectra above and below the magnetic transition. Since the optical spectroscopy studies [Ref. 5.13, Ref. 5.14] intrinsically probe phonons at near the zone center, the information from the IXS spectra obtained over the full Brillouin zone is extremely useful for understanding the SP coupling in $\text{Cd}_2\text{Os}_2\text{O}_7$. The IXS spectra obtained at 282 and 100 K with $\mathbf{Q} = \text{W}$ (6.50 6.00 7.00) are presented in Fig. 5.4(a).

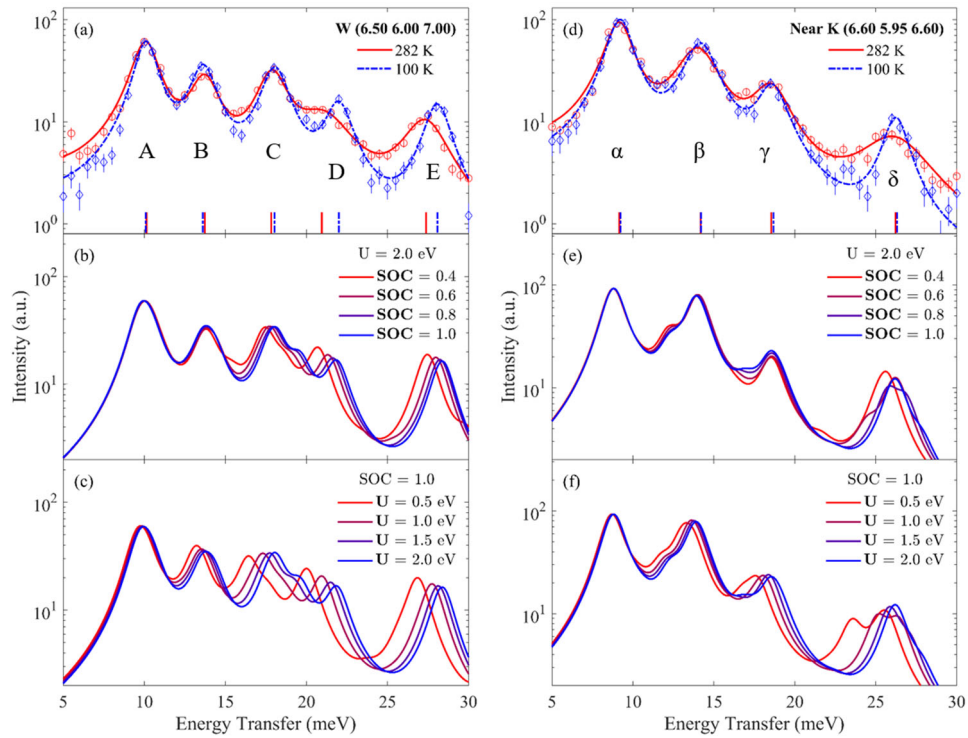


Figure 5.4 (a, d) The IXS spectra taken at 282 and 100 K at $\mathbf{Q} = \text{W}$ (6.50 6.00 7.00) and near K (6.60 5.95 6.60). The vertical bars under the spectra indicate the fitted peak positions. **(b, e)** The calculated IXS spectra that are based on DFT calculations by varying the strength of SOC. **(c, f)** The calculated IXS spectra that are based on the

DFT calculations by varying U values.

In Fig. 5.4(a), five phonons, labeled as A–E in the increasing order of energies, can be seen. Upon magnetic transition, the peaks D and E are shifted toward higher energies, whereas no changes in the positions of the three peaks A, B, and C are observed. Moreover, in Fig. 5.4(d), at another Q position, near K (6.60 5.95 6.60), four peaks labeled as α , β , γ , and δ are observed. No notable energy shifts, except for the broadening of the peak δ , can be observed. It is known that there is no structural transition over the temperature range of 100–282 K. The observed phonon energy shifts can be originated from the SP coupling.

It is possible that just a change in lattice parameter can induce a change in phonon energy without lowering any crystal symmetry through the phase transition. The Grüneisen parameter γ_G can be used to quantify the phonon energy change by the temperature effect. Unfortunately, we could not find the experimentally determined Grüneisen parameter for $\text{Cd}_2\text{Os}_2\text{O}_7$. Instead, we would refer to the pyrochlore hafnates [Ref. 5.23]. According to the reported value, γ_G for $\text{Y}_2\text{Hf}_2\text{O}_7$ is mode-dependent, and its average value is approximately 6. From this information, we anticipate a volume change of approximately 2.6 \AA^3 at a temperature between 300 and 100 K for $\text{Cd}_2\text{Os}_2\text{O}_7$. If we assume that the γ_G value for $\text{Cd}_2\text{Os}_2\text{O}_7$ is similar to that for $\text{Y}_2\text{Hf}_2\text{O}_7$, then phonon energy change $\Delta\omega$ can be approximated as follows:

$$\Delta\omega = \gamma_G \frac{\omega_{300K}}{V_{300K}} \Delta V = 0.015\omega_{300K}.$$

However, observed phonon energy shift in peak D is 4.79 %, which is much larger than the shift of 1.5 % from the lattice parameter change. So, we assume that the primary origin for the phonon energy shift is not the lattice parameter change with temperature. Furthermore,

the possibility of electron–phonon coupling has already been discussed in a previous study [Ref. 5.14], which argued that the phonon change from the electron–phonon coupling is small enough to be neglected.

Based on the observed energy shift, the SP coupling has a mode dependence at a finite Q position. As mentioned, the phonon peaks D and E in the IXS spectra are highly related to the vibrations of the magnetic Os atoms, according to the eigenvector calculated by the DFT calculations. Hence, this is another evidence of the SP coupling. As the IXS spectra measured at near K shows no visible energy change, we consider that it is the first and direct evidence of the SP coupling with the visible momentum dependence.

Another important observation is the linewidth change of the peaks D and E, as shown in Fig. 4(a, d). The peaks D and E measured at 100 K are fitted using Lorentzian functions, and the FWHM of the peaks are found to be 1.68 and 1.79 meV, respectively, which is similar to the energy resolution of 1.5 meV for the instrument we used in the IXS experiment. However, above the transition temperature, the obtained linewidths of the peaks are 4.59 and 2.56 meV, which are larger than expected if we consider only thermal broadening effects. Indeed, this broadening effect should be related to either the electron–phonon coupling or the SP coupling. But as discussed earlier in a previous study [Ref. 5.14], the linewidth change seems to be originated from the SP coupling, and not from the electron–phonon coupling. Taken together, the SP coupling is thought to be a more reliable origin of the observed broadening in both IR and IXS experiments.

5.2.2 SOC effect on the phonons

As introduced earlier, we performed the DFT calculations with the help of Dr. C. H. Kim. First-principle calculations were performed using DFT + U with the Perdew–Burke–Ernzerhof (PBEsol) exchange-correlation functional implemented in VASP [Ref. 5.14]. The AIAO magnetic structure was applied to the DFT calculations using noncollinear DFT formalism. The frozen phonon method was used for the phonon calculation using PHONOPY [Ref. 5.24]. As the input parameters, i.e., $U = 0.5, 1.0, 1.5,$ and 2.0 eV, were chosen to consider the local Hubbard interaction in Os atoms. We also varied the scaling factor of the SOC from 0.4 to 1.0 in the DFT calculations. The scaling factor 1.0 means that we fully consider SOC in the calculations, whereas the scaling factor below 1.0 indicates that we scale down SOC strength during the calculations. For example, the scaling factor 0.5 means that we artificially reduced SOC strength as half compare to the value when we fully consider SOC. Note that the scaling factor is not an exact unit of eV.

Before examining the effects of SOC on phonons as a function of SOC strength, it is important to note that the current DFT calculations without including any other interaction terms are in good agreement with the IXS data obtained at 100 K, i.e., SP coupled state. This implies that the DFT calculations already captured the SP coupling in $\text{Cd}_2\text{Os}_2\text{O}_7$. Since the anharmonic or higher-order interactions (e.g., phonon–phonon or magnon–phonon [Ref. 5.18]) are not included in the current calculations, the consideration of SOC and noncollinear magnetic structure during the calculations are considered as the entire origin of the excellent agreement between experiment and calculations. Furthermore, the magnon–phonon coupling effect is estimated to be small for the range of observed

phonon energies. According to their spin Hamiltonian [Ref. 5.13], the magnons in $\text{Cd}_2\text{Os}_2\text{O}_7$ are placed from 60 to 100 meV. This suggests that a large gap of 35 meV exists between the phonons and magnons, and their interaction is expected to be small [Ref. 5.21].

When the U and the SOC scaling factors are varied, the mode dependency of the energy shift is clearly demonstrated in our calculations. As shown in Fig. 5.4(b, c) and Fig. 5.4(e, f), the calculated IXS cross-sections for a different set of U and SOC exhibit different behaviors. When SOC is scaled from 0.4 to 1.0, the peaks D and E are shifted, whereas the positions of the peaks A, B, and C remained. However, if we vary U from 0.5 to 2.0 eV, then the peaks B, C, D, and E change accordingly. If we define the energy renormalization $\Delta E/E_0 = |(E_{282K} - E_{100K})|/E_{100K}$, the $\Delta E/E_0$ of the peaks A and D are found to be 0.42 % and 4.79 %, respectively. The $\Delta E/E_0$ induced by changing U from 0.5 to 2.0 eV are 2.02 % and 8.08 % for the peaks A and D, respectively. Further, the $\Delta E/E_0$ induced by changing the SOC strength from 0.4 to 1.0 are found to be 0.63% and 4.79%. The similarity of the energy renormalization between the experiments and the calculations indicates that varying SOC explains the mode dependency as well as the renormalization value. Furthermore, in the case of the IXS spectra at near K point (Fig. 5.4(e, f)), scaling SOC moves only the peak δ , while changing U moves the peaks β , γ , and δ . Based on these analyses, we found that scaling the SOC strengths affect phonons; this observation is similar to the experimental findings.

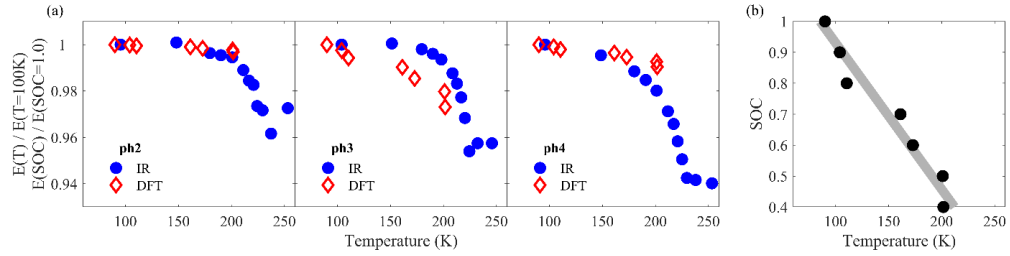


Figure 5.5 (a) Energy renormalization of three IR-active phonons adapted from [Ref. 5.14]. The calculated energy renormalization for the three phonons from the DFT calculations matches the temperature dependence of three phonons simultaneously. (b) The nearly linear relationship between SOC and temperature obtained from the best fit in Fig. 5.5(a).

It is also confirmed that the temperature dependence and the SOC strength dependence of IR-active phonons are similar, as shown in Fig. 5.5(a). When we scale down the SOC strength, then the energy of the IR-active phonons is reduced, which is similar to the experimental observations. Note that the data and the labels for three phonons are adapted from the [Ref. 5.14]. To obtain the best fit, we matched the three IR phonon energies simultaneously using the SOC strength dependency of the phonon energy. As a result, an approximately linear relationship between SOC and temperature is obtained, as shown in Fig. 5.5(b). Thus, we assume that SOC can effectively explain the temperature dependence of the SP coupling.

5.3 Discussion and summary

5.3.1 A common feature of temperature and SOC effect

One can assume that a direct comparison between temperature and SOC would be inappropriate because the SOC is the intrinsic property in materials and cannot be considered as a temperature-dependent quantity. All the calculations in this study were performed at zero temperature, which does not include any temperature effect. We would like to emphasize that scaling the SOC strength can still be an effective way to interpret the temperature effects of the SP coupling in $\text{Cd}_2\text{Os}_2\text{O}_7$. The energy renormalization $\Delta\omega_\sigma$ from the SP coupling can be explained by the SIA K in the $\text{Cd}_2\text{Os}_2\text{O}_7$ case, and it is expressed as follows [Ref. 5.14].

$$\Delta\omega_\sigma = \sum_i \frac{\partial^2 K}{\partial \mathbf{u}_{i,\sigma}^2} \langle (\mathbf{S}_i \cdot \mathbf{n}_i)^2 \rangle$$

Here, $\mathbf{u}_{i,\sigma}$ is the atomic displacement with an atom index i and band index σ . The $\frac{\partial^2 K}{\partial \mathbf{u}_{i,\sigma}^2}$ term is directly related to the SP coupling constant, and it is dependent on the phonon modes that include vibration of the Os atoms. In addition, the SIA K is assumed to be proportional to the square of SOC [Ref. 5.25]. Scaling the SOC strength in the calculations can directly affect the $\frac{\partial^2 K}{\partial \mathbf{u}_{i,\sigma}^2}$ term. Thus, a reduction in the SOC strength decreases the coupling constant. Moreover, it induces phonon energy renormalization, as observed experimentally. From the temperature viewpoint, the $\langle (\mathbf{S}_i \cdot \mathbf{n}_i)^2 \rangle$ term is a temperature-dependent quantity. The spin fluctuations decrease when the temperature increases above the magnetic transition temperature. Therefore, $\Delta\omega_\sigma$ should decrease as a result. Changing K by scaling

the strength of SOC and changing the magnetic moment fluctuation by changing the temperature has the same effect on $\Delta\omega_\sigma$.

5.3.2 Summary

In summary, we performed an experimental investigation of phonons over the full Brillouin zone in $\text{Cd}_2\text{Os}_2\text{O}_7$ using IXS. We found a clear mode dependence of phonon energy renormalization. The IXS spectra of the SP-coupled phase ($T < T_N$) were well captured through DFT calculations using $U = 2.0$ eV and considering full SOC. After manipulating both U and SOC in the DFT calculations, the observed mode-dependent SP coupling was obtained by mainly varying the SOC, and not U . Furthermore, we found that the SOC can practically explain the temperature effect of the SP coupling in $\text{Cd}_2\text{Os}_2\text{O}_7$. In conclusion, we would like to emphasize that SOC is the fundamental factor in describing the SP coupling in $\text{Cd}_2\text{Os}_2\text{O}_7$. These results can be applied further to other compounds that exhibit strong spin-lattice coupling or SP coupling.

References

- [Ref. 5.1] W. Witczak-Krempa, G. Chen, Y. B. Kim, and L. Balents, *Annu. Rev. Condens. Matter Phys.* **5**, 57 (2014).
- [Ref. 5.2] B. J. Kim, H. Jin, S. J. Moon, J.-Y. Kim, B.-G. Park, C. S. Leem, J. Yu, T. W. Noh, C. Kim, S.-J. Oh, J.-H. Park, V. Durairaj, G. Cao, and E. Rotenberg, *Phys. Rev. Lett.* **101**, 76402 (2008).
- [Ref. 5.3] J. Reading and M. T. Weller, *J. Mater. Chem.* **11**, 2373 (2001).
- [Ref. 5.4] S. Calder, J. G. Vale, N. A. Bogdanov, X. Liu, C. Donnerer, M. H. Upton, D. Casa, A. H. Said, M. D. Lumsden, Z. Zhao, J. Q. Yan, D. Mandrus, S. Nishimoto, J. Van Den Brink, J. P. Hill, D. F. McMorrow, and A. D. Christianson, *Nat. Commun.* **7**, 11651 (2016).
- [Ref. 5.5] J. G. Vale, S. Calder, N. A. Bogdanov, C. Donnerer, M. M. Sala, N. R. Davies, D. Mandrus, J. van den Brink, A. D. Christianson, and D. F. McMorrow, *Phys. Rev. B* **101**, 14441 (2020).
- [Ref. 5.6] N. A. Bogdanov, R. Maurice, I. Rousochatzakis, J. Van Den Brink, and L. Hozoi, *Phys. Rev. Lett.* **110**, 127206 (2013).
- [Ref. 5.7] J. Yamaura, K. Ohgushi, H. Ohsumi, T. Hasegawa, I. Yamauchi, K. Sugimoto, S. Takeshita, A. Tokuda, M. Takata, M. Udagawa, M. Takigawa, H. Harima, T. Arima, and Z. Hiroi, *Phys. Rev. Lett.* **108**, 247205 (2012).
- [Ref. 5.8] A. W. Sleight, J. L. Gillson, J. F. Weiher, and W. Bindloss, *Solid State Commun.* **14**, 357 (1974).
- [Ref. 5.9] D. Mandrus, J. R. Thompson, R. Gaal, L. Forro, J. C. Bryan, B. C.

- Chakoumakos, L. M. Woods, B. C. Sales, R. S. Fishman, and V. Keppens, *Phys. Rev. B* **63**, 195104 (2001).
- [Ref. 5.10] C. H. Sohn, H. Jeong, H. Jin, S. Kim, L. J. Sandilands, H. J. Park, K. W. Kim, S. J. Moon, D. Y. Cho, J. Yamaura, Z. Hiroi, and T. W. Noh, *Phys. Rev. Lett.* **115**, 266402 (2015).
- [Ref. 5.11] Z. Hiroi, J. Yamaura, T. Hirose, I. Nagashima, and Y. Okamoto, *APL Mater.* **3**, 41501 (2015).
- [Ref. 5.12] H. Shinaoka, T. Miyake, and S. Ishibashi, *Phys. Rev. Lett.* **108**, 247204 (2012).
- [Ref. 5.13] T. M. H. Nguyen, L. J. Sandilands, C. H. Sohn, C. H. Kim, A. L. Wysocki, I.-S. Yang, S. J. Moon, J.-H. Ko, J. Yamaura, Z. Hiroi, and T. W. Noh, *Nat. Commun.* **8**, 251 (2017).
- [Ref. 5.14] C. H. Sohn, C. H. Kim, L. J. Sandilands, N. T. M. Hien, S. Y. Kim, H. J. Park, K. W. Kim, S. J. Moon, J. Yamaura, Z. Hiroi, and T. W. Noh, *Phys. Rev. Lett.* **118**, 117201 (2017).
- [Ref. 5.15] M. Mochizuki, N. Furukawa, and N. Nagaosa, *Phys. Rev. Lett.* **105**, 37205 (2010).
- [Ref. 5.16] E. R. Callen and H. B. Callen, *Phys. Rev.* **129**, 578 (1963).
- [Ref. 5.17] E. Callen and H. B. Callen, *Phys. Rev.* **139**, A455 (1965).
- [Ref. 5.18] J. Oh, M. D. Le, H.-H. Nahm, H. Sim, J. Jeong, T. G. Perring, H. Woo, K. Nakajima, S. Ohira-Kawamura, Z. Yamani, Y. Yoshida, H. Eisaki, S. W. Cheong, A. L. Chernyshev, and J.-G. Park, *Nat. Commun.* **7**, 13146 (2016).

- [Ref. 5.19] T. Kim, J. C. Leiner, K. Park, J. Oh, H. Sim, K. Iida, K. Kamazawa, and J.-G. Park, *Phys. Rev. B* **97**, 201113 (2018).
- [Ref. 5.20] T. Kim, K. Park, J. C. Leiner, and J.-G. Park, *J. Phys. Soc. Japan* **88**, 81003 (2019).
- [Ref. 5.21] K. Park, J. Oh, K. H. Lee, J. C. Leiner, H. Sim, H. Nahm, T. Kim, J. Jeong, D. Ishikawa, A. Q. R. Baron, and J. Park, *Phys. Rev. B* **102**, 85110 (2020).
- [Ref. 5.22] A. Q. R. Baron, *SPring-8 Inf. Newsl.* **15**, 14 (2010).
- [Ref. 5.23] K. M. Turner, D. R. Rittman, R. A. Heymach, C. L. Tracy, M. L. Turner, A. F. Fuentes, W. L. Mao, and R. C. Ewing, *J. Phys. Condens. Matter* **29**, 255401 (2017).
- [Ref. 5.24] A. Togo and I. Tanaka, *Scr. Mater.* **108**, 1 (2015).
- [Ref. 5.25] D. Dai, H. Xiang, and M.-H. Whangbo, *J. Comput. Chem.* **29**, 2187 (2008).

Chapter 6

Summary and Outlook

6.1 Summary

I discussed two main projects through my thesis: (1) Magnon-phonon coupling in HoMnO_3 and (2) Spin-phonon coupling in $\text{Cd}_2\text{Os}_2\text{O}_7$. Both compounds are highly expected to have large spin-lattice coupling from the previous results. So, it is expected that the magnons and phonons might have distinct behavior from normal states. Therefore, the details of the study on excitation spectra like phonons and magnons are needed. Conducting two experimental techniques, INS at 4SEASONS in J-PARC and IXS at BL43LXU in SPring-8, it is possible to examine what features arise from the couplings for each material.

In HoMnO_3 , the magnon dispersions at the low temperature were successfully obtained, and several anomalous features appear that LSWT cannot explain. The downward curvature of the low energy magnon branch and the global energy renormalization are in good agreement with the ESP model, including magnon-phonon coupling. The low diffusive intensity above the single-magnon branches suggests that the magnon-magnon interaction is suppressed in HoMnO_3 . Notably, the ESP model can explain the intensity ratio between the magnons. So, the magnon-phonon coupling is regarded as the dominant interaction in HoMnO_3 .

The phonon dispersions were successfully obtained based on the second project, the investigation of phonons in $\text{Cd}_2\text{Os}_2\text{O}_7$. The phonon renormalization and its mode dependency were found as similar to the previous IR spectroscopy study. The momentum

dependence of such spin-phonon coupling is also confirmed based on the IXS spectra at different momentum positions. We also provide the effect of SOC on the phonons, and the reduction of SOC reproduce the mode and momentum dependence of the phonon renormalization well. The temperature dependence of the IR-active phonons is also in good agreement with the expectation of SOC dependence. Based on these results, SOC can be regarded as the main ingredient of the spin-phonon coupling in $\text{Cd}_2\text{Os}_2\text{O}_7$.

Materials	S	Type of magnetic Hamiltonian	Features	Mechanism
h-LuFeO_3	$5/2$	Heisenberg XXZ with easy-plane anisotropy	no anomalous features	—
h-RMnO_3	2	Heisenberg XXZ with easy-plane anisotropy	energy renormalization hybridized mode and its decay downward shift at M point	exchange-striation single-ion magneto-striation
ACrO_2	$3/2$	Heisenberg	hybridized mode downward shift at M point	exchange-striation type magnon-phonon coupling
$\text{Ba}_3\text{CoSb}_2\text{O}_9$	$1/2$	Heisenberg XXZ	strong energy renormalization intrinsic linewidth broadening large and broad continuum	magnon-magnon interaction
Cs_2CuCl_4	$1/2$	Heisenberg	strong energy renormalization intrinsic linewidth broadening large and broad continuum	magnon-magnon interaction spinon continuum

Table 6.1 A summary table for the experimentally investigated triangular lattice antiferromagnet materials. It is adapted from [Ref. 6.1].

Based on these results and the previous studies on magnon-phonon coupling, I participated in writing a review paper [Ref. 6.1]. In this review, the hybridization and decay of magnetic excitations in triangular lattice antiferromagnet are mainly discussed. Several theoretical works on developing formalism of magnon-magnon interaction and magnon-phonon coupling Hamiltonian are summarized. Besides, experimental evidence of the magnon-phonon coupling and magnon-magnon interaction are reviewed. Here, I adapted

one summary table of experimental findings in several triangular lattice antiferromagnet systems, as shown in Table 6.1.

6.2 Outlook

During my Ph. D. course, how the magnon-phonon or spin-phonon coupling affects the collective excitations and how we can understand by specific models were studied. This research is slightly concentrated on the fundamental aspects. The applicability of the magnon-phonon coupling is also important to spintronic fields [Refs. 6.2–6.4]. For example, suppose magnons can have the phonon characters by forming the magneto-elastic excitations. In that case, these hybridized excitations can move more swiftly through the medium than the usual magnons. The delivering velocity of the information using the magneto-elastic excitations can be more efficient.

This potential applicability and the understanding of the couplings still need to be studied in the fundamental viewpoints. The magnon-phonon coupling or the magnon-magnon interaction in antiferromagnetic metal are not well-understood yet. There are some attempts to examine the magnon-phonon coupling or magnon-magnon interaction in metal, such as Mn_3Sn [Ref. 6.5] and CrB_2 [Ref. 6.6]. The observed intrinsic broadening of the magnons can be originated from both the magnon-magnon interaction or the interaction between magnons and conduction electrons. However, the full examination is limited due to the lack of information on how we can distinguish the effects of the magnon-magnon interaction and the metallic state separately. The theoretical methods still need to be developed to understand the mechanism widely.

The quantum fluctuation may give some distinct features on the magnon-phonon coupling. Indeed, the magnon-magnon interaction is elevated up when the spins are $1/2$. The multiple continuum state from the decay of the magnons in $\text{Ba}_3\text{CoSb}_2\text{O}_9$ is also discovered, totally different from the known properties [Refs. 6.7 & 6.8]. In principle, the magnon-phonon coupling can also spontaneously decay and make a continuum state. As a result, some new properties like the multiple continuum state of the magneto-elastic excitations are also possibly observed.

The magnon-phonon coupling physics can be expanded in other lattice structures, too. So far, this coupling is widely studied in triangular lattice antiferromagnet. The noncollinear structure can be found in many cases, for example, kagome lattice and pyrochlore lattice. Especially, the AIAO ordering structure is present in pyrochlore lattice. Unfortunately, the INS experiment is not possible for $\text{Cd}_2\text{Os}_2\text{O}_7$, and the phonons with higher energy are not detected due to low signals. So, the magnon-phonon coupling features are not detected from the present IXS study. Since the evidence of the magnon-magnon interaction is suggested in $\text{Yb}_2\text{Ti}_2\text{O}_7$ [Ref. 6.9], it is also a highly desired platform to study such couplings.

References

- [Ref. 6.1] T. Kim, K. Park, J. C. Leiner, and J.-G. Park, *J. Phys. Soc. Japan* **88**, 081003 (2019).
- [Ref. 6.2] M. Xu, J. Puebla, F. Auvray, B. Rana, K. Kondou, and Y. Otani, *Phys. Rev. B* **97**, 180301 (2018).
- [Ref. 6.3] H. Man, Z. Shi, G. Xu, Y. Xu, X. Chen, S. Sullivan, J. Zhou, K. Xia, J. Shi, and P. Dai, *Phys. Rev. B* **96**, 100406 (2017).
- [Ref. 6.4] S. C. Guerreiro and S. M. Rezende, *Phys. Rev. B* **92**, 214437 (2015).
- [Ref. 6.5] P. Park, J. Oh, K. Uhlířová, J. Jackson, A. Deák, L. Szunyogh, K. H. Lee, H. Cho, H.-L. Kim, H. C. Walker, D. Adroja, V. Sechovský, and J.-G. Park, *Npj Quantum Mater.* **3**, 63 (2018).
- [Ref. 6.6] P. Park, K. Park, T. Kim, Y. Kousaka, K. H. Lee, T. G. Perring, J. Jeong, U. Stuhr, J. Akimitsu, M. Kenzelmann, and J.-G. Park, *Phys. Rev. Lett.* **125**, 027202 (2020).
- [Ref. 6.7] S. Ito, N. Kurita, H. Tanaka, S. Ohira-Kawamura, K. Nakajima, S. Itoh, K. Kuwahara, and K. Kakurai, *Nat. Commun.* **8**, 235 (2017).
- [Ref. 6.8] R. Verresen, R. Moessner, and F. Pollmann, *Nat. Phys.* **15**, 750 (2019).
- [Ref. 6.9] J. D. Thompson, P. A. McClarty, D. Prabhakaran, I. Cabrera, T. Guidi, and R. Coldea, *Phys. Rev. Lett.* **119**, 057203 (2017).

Appendix A

Studies on Verwey transition in Fe₃O₄ nanoparticle

In this chapter, I would like to address my works on Fe₃O₄ nanoparticles during my degree. Fe₃O₄ is a famous material in various fields due to its interesting physical properties. The most extensive studies have been done to understand the Verwey transition in this material [Ref. A.1]. Various physical properties, such as magnetization, lattice structure, heat capacity, resistivity, and so on, change at the Verwey transition temperature ($T_v \sim 124$ K) [Ref. A.2]. It is natural to think that the Verwey transition is a complex phenomenon in which several degrees of freedom may correlate with each other. Since the first discovery of the transition by E. J. Verwey in 1939 [Ref. A.1], many researchers tried to catch the origin and mechanism of the transition. Recently, Prof. J. P. Attfield suggests that the main driving force is the orbital ordering, which has peculiar patterns called trimeron [Ref. A.3].

What I focus on in this study is how the Verwey transition change in nanoscale. The former member of the group, Dr. Jisoo Lee, already found that the Verwey transition shows different behavior from the bulk case [Ref. A.4]. The T_v is dependent on the size of the nanoparticles, as shown in Fig. A.1. Furthermore, if we go down to 7 nm size, the Verwey transition is no longer observed due to the Blocking temperature.

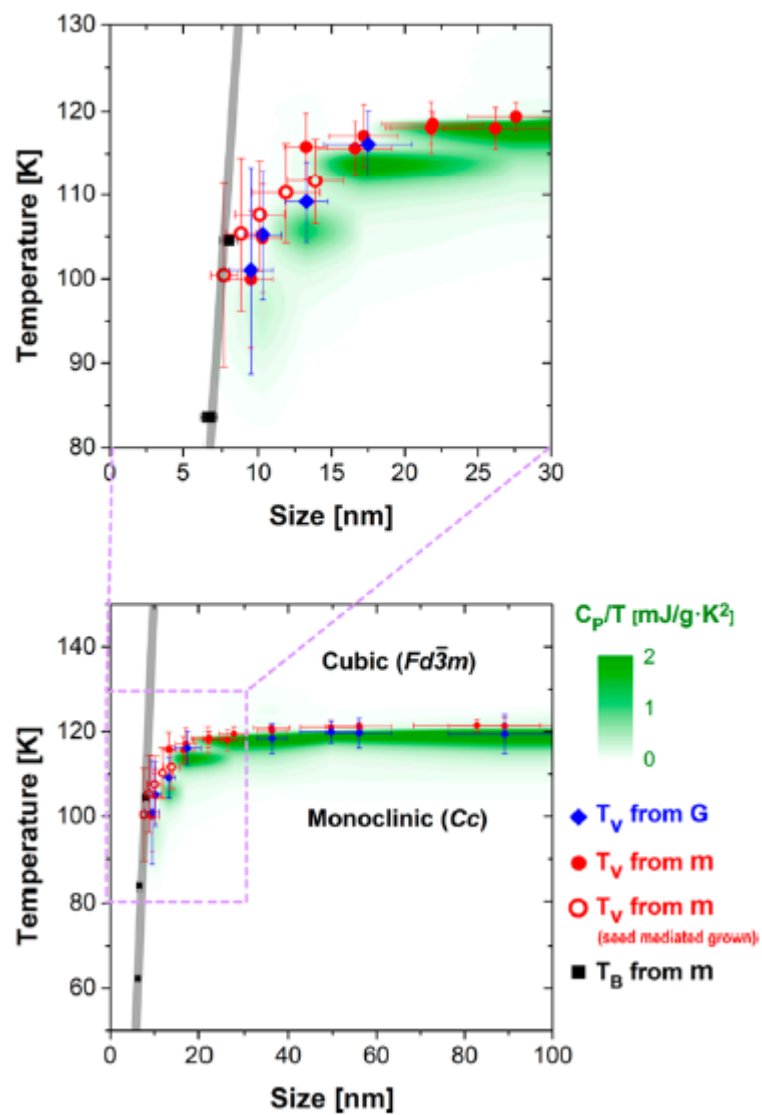


Figure A.1. Size dependence of T_v , which is adapted from [Ref. A.4].

We also found that there is a large deviation from the bulk observed in thermal hysteresis of the transition. The thermal hysteresis width is size-dependent, and its behavior

is similar to the size dependence of coercivity, which indicates the correlation between spin and charge degrees of freedom [Ref. A.5]. I will discuss these results in the next section.

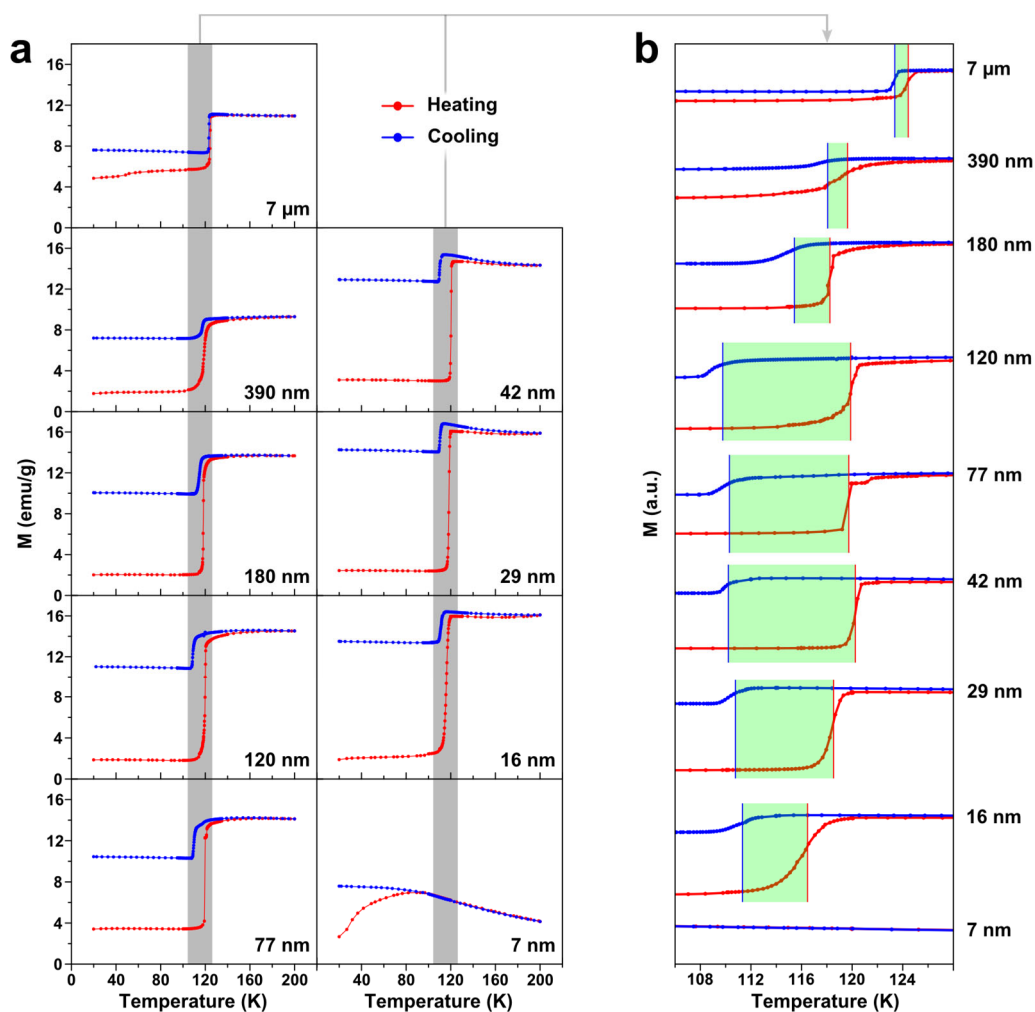


Figure A.2 (a) Magnetization measurements for several Fe₃O₄ nanoparticles with various sizes. The red(blue) curves are measured upon the heating(cooling) process. **(b)** The enlarged area plots for the thermal hysteresis. The green-colored regions indicate the thermal hysteresis width, which can be defined as the difference between T_v for the heating and cooling process.

A.1 Large thermal hysteresis of Verwey transition in Fe_3O_4 nanoparticle

Verwey transition is known as a first-order transition. It means that there should be a thermal hysteresis in the transition. For the bulk case, the thermal hysteresis width is found to be approximately 1 K. We found that the thermal hysteresis becomes large when the size is reduced down to nanometer scale.

We investigated the thermal hysteresis of Verwey transition in various sized samples by measuring magnetization as shown in Fig. A.2. The 7 μm sized sample can be regarded as the bulk case, and other sample sizes from 7 to 390 nm are synthesized by using the same method in the ref. The 7 μm sized sample shows the conventional thermal hysteresis width ~ 1 K, but the width becomes large when the size of the sample decreases. We found that the width reaches the maximum value of 11 K at 120 nm size. Below 120 nm, the width decreases as the size reduces.

Not only the magnetization but also the nuclear magnetic resonance (NMR) spectroscopy observed the large thermal hysteresis of Verwey transition too. As shown in Fig. A.3, if we track the NMR spectrum measured from 130 K to 80 K and 80 K to 130 K, then the usual peak splitting due to Verwey transition was observed at two different temperatures, whether it is cooling or heating. For more details on the peak splitting, please see the [Ref. A.6]. For the bulk (7 μm) case, the thermal hysteresis width is found to be 1 K. For the nanometer scale, the thermal hysteresis width increases up to 10 K for 42 nm as similar to the magnetization results. Since the NMR spectroscopy can probe the local magnetic field inside the material, we could think that these results show the microscopic evidence of Verwey transition as well as the existence of the thermal hysteresis.

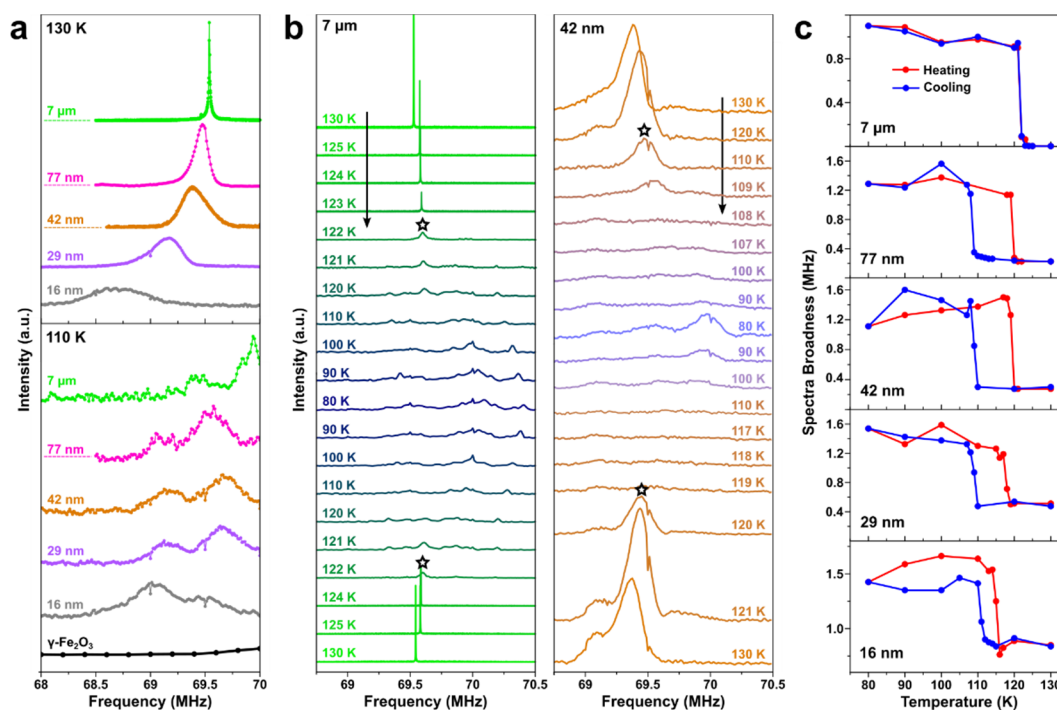


Figure A.3 (a) NMR spectra for several nanoparticle samples, including bulk case measured at 130 and 110 K (above and below T_V). **(b)** The temperature dependence of the NMR spectra for bulk (7 μm) and 42 nm case. **(c)** The temperature dependence of the spectral broadness for each sample.

As the magnetization and NMR spectra probe the spin part of Verwey transition, we need to verify that the thermal hysteresis should be observed in the lattice part of Verwey transition. To investigate the above thermal hysteresis in a lattice point of view, we carried out X-ray diffraction (XRD) measurements upon heating and cooling. We picked (440) Bragg peak to probe the Verwey transition, which provides visible change through the

transition. As shown in Fig. A.4(a-b), the enlarged thermal hysteresis of Verwey transition was also confirmed by the XRD measurements.

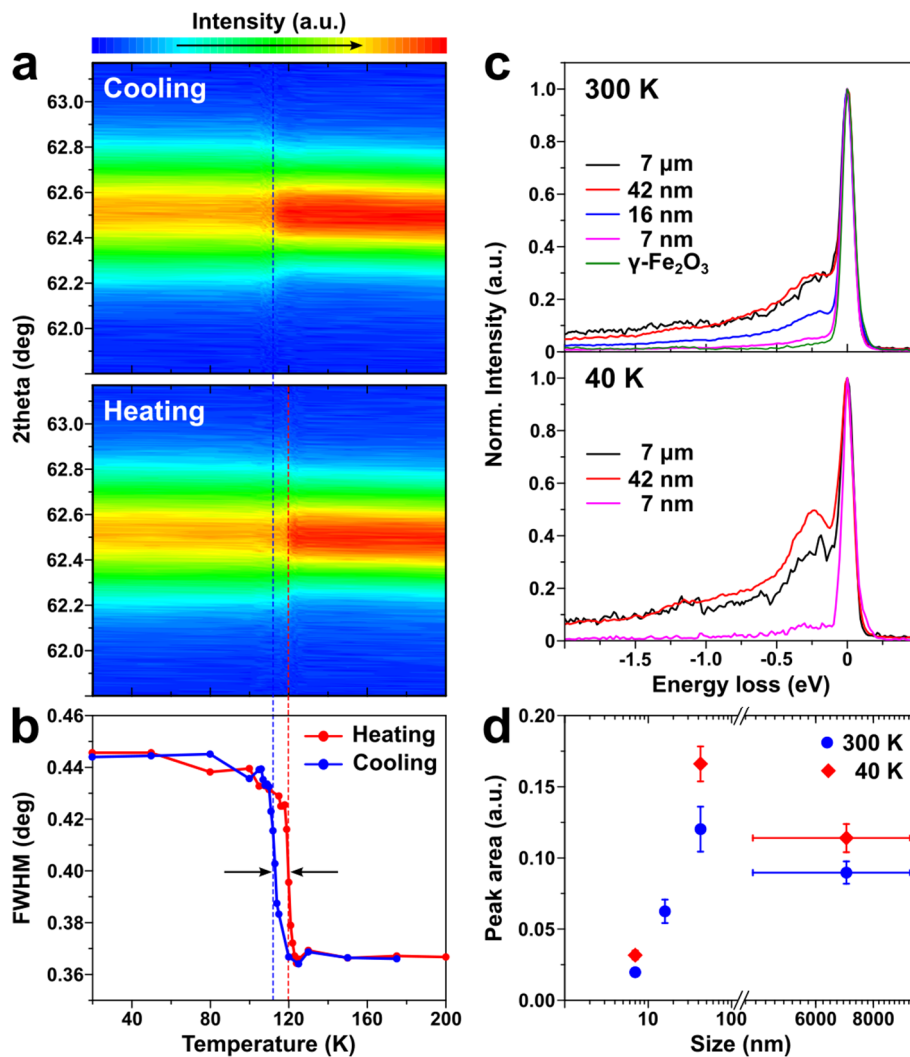


Figure A.4 (a) The color plots for the temperature dependence of (440) Bragg peak. (b) The temperature dependence of the FWHM of (440) XRD peak. (c) RIXS spectra for several nanoparticles measured at 300 and 40 K. (d) Obtained peak area of magnetic polaron for each sample at 300 and 40 K.

We also investigate the magnetic polaron in Fe_3O_4 nanoparticles using resonant inelastic X-ray scattering (RIXS) experiments. Using near Fe L_3 -edge and σ polarization, we observed the polaronic excitation centered at 200 meV energy transfer. The polaron was recently discovered by Prof. D. J. Huang's group, and its origin is related to orbital ordering [Ref. A.7]. As similar to the bulk case, we could not find any temperature dependence of the polaron in nanoparticles. Instead, the peak area shows the size dependence and almost vanishes when the size goes down to 7 nm. This may be related to the suppression of T_v in 7 nm-sized nanoparticle.

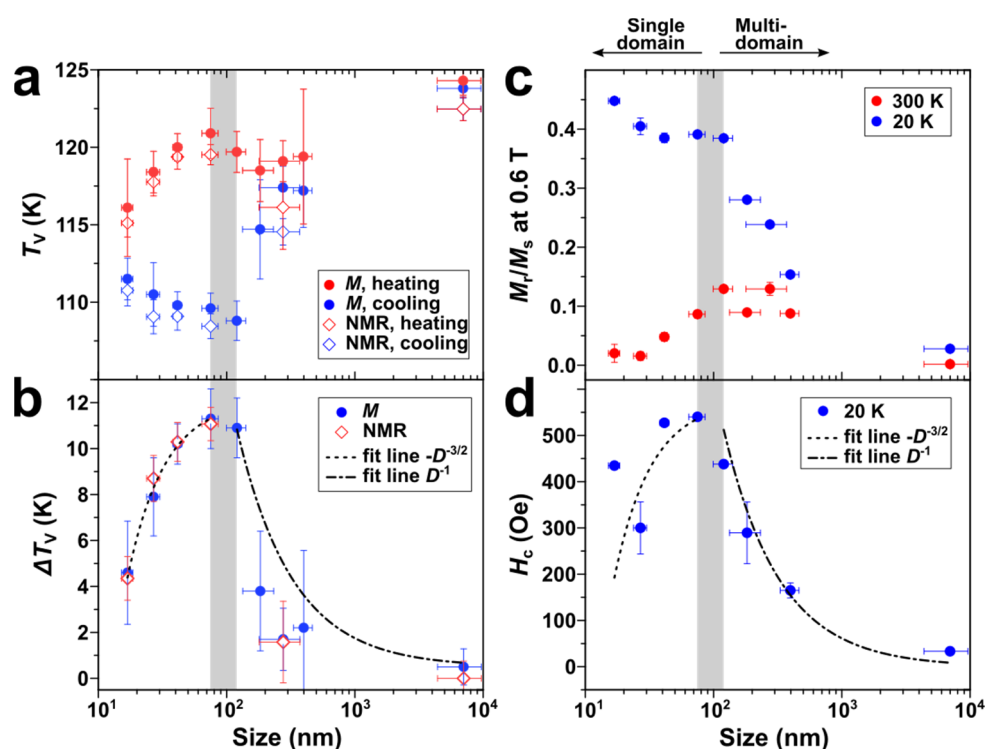


Figure A.5 (a) The observed T_v when the sample is heating and cooling. (b) The thermal hysteresis width (ΔT_v) as a function of nanoparticle size. (c) The ratio between remnant and saturated magnetization for each samples. (d) The measured coercive field as a function of size.

Taken all the data we measured, we could summarize the size dependence of the thermal hysteresis of Verwey transition. As shown in Fig. A.5, the clear size dependence of the thermal hysteresis width ΔT_v was obtained. Above 120 nm, the ΔT_v decreased and was successfully fitted by the polynomial equation (proportional to D^{-1}). Below the 120 nm, the ΔT_v also decreases, but it was fitted by the different equation (proportional to $-D^{-3/2}$). As plotted in Fig. A.5 (d), the size dependence of the ΔT_v is similar to the size dependence of coercive field H_c . The size dependence of H_c in ferromagnetic material is well-known behavior [Ref. A.8] and it is exactly the same with the observations. The critical radius of 120 nm tells us that the magnetic domain can be a single domain below 120 nm, and a multi-domain structure can be formed above 120 nm. Since H_c reflects the kinetic stability of magnetization reversal and ΔT_v has the same meaning for Verwey transition (charge / orbital ordering), we think that the spin and charge degrees of freedom correlate with each other, and it naturally appears in the size dependence of the ΔT_v and H_c .

In summary, we investigated the thermal hysteresis of Verwey transition in Fe_3O_4 nanoparticles by using several measurements such as magnetization, NMR spectra, XRD patterns, and RIXS spectra. We found that there is a strong similarity between the size dependence of the ΔT_v and H_c , which indicates the strong coupling between spin and charge degrees of freedom.

References

- [Ref. A.1] E. J. W. VERWEY, *Nature* **144**, 327 (1939).
- [Ref. A.2] F. Walz, *J. Phys. Condens. Matter* **14**, R285 (2002).
- [Ref. A.3] M. S. Senn, J. P. Wright, and J. P. Attfield, *Nature* **481**, 173 (2012).
- [Ref. A.4] J. Lee, S. G. Kwon, J.-G. Park, and T. Hyeon, *Nano Lett.* **15**, 4337 (2015).
- [Ref. A.5] T. Kim, S. Lim, J. Hong, S. G. Kwon, J. Okamoto, Z. Y. Chen, J. Jeong, S. Kang, J. C. Leiner, J. T. Lim, C. S. Kim, D. J. Huang, T. Hyeon, S. Lee, and J.-G. Park, *Sci. Rep.* **8**, 5092 (2018).
- [Ref. A.6] S. Lim, B. Choi, S. Y. Lee, S. Lee, H.-H. Nahm, Y.-H. Kim, T. Kim, J.-G. Park, J. Lee, J. Hong, S. G. Kwon, and T. Hyeon, *Nano Lett.* **18**, 1745 (2018).
- [Ref. A.7] H. Y. Huang, Z. Y. Chen, R.-P. Wang, F. M. F. de Groot, W. B. Wu, J. Okamoto, A. Chainani, A. Singh, Z.-Y. Li, J.-S. Zhou, H.-T. Jeng, G. Y. Guo, J.-G. Park, L. H. Tjeng, C. T. Chen, and D. J. Huang, *Nat. Commun.* **8**, 15929 (2017).
- [Ref. A.8] J. M. D. Coey, Chap. 11 Magnetic materials, in *Magnetism and Magnetic Materials* (Cambridge University Press, 2001), pp. 374–438.

국문초록

HoMnO₃ 와 Cd₂Os₂O₇ 에 대한
마그논-포논 결합 연구

김태훈

물리천문학부 물리학전공

서울대학교 대학원

응집물질물리학에서 고체 내의 기본적인 자유도 간의 상호작용은 흔히 나타나는 필수적인 현상이다. 대부분의 경우 이런 상호작용들이 존재하기 때문에 각각의 메커니즘과 그에 따른 결과들을 규명할 필요성이 있다. 스핀-격자 결합은 하나의 예로서 고체 내 스핀과 격자 자유도 간의 결합을 말한다. 1950년대부터 연구가 시작된 오래된 개념이지만 아직 완전히 이해되지 못하고 있다.

스핀-격자 결합의 한 부분인 마그논-포논 결합 (magnon-phonon coupling) 에 대한 연구가 중성자 및 엑스선 기술 발달에 의해 활발히 이루어지고 있고 특히 RMnO₃ 나 ACrO₂ 등의 물질이 연구되었다. 두 물질 모두 비선형 자기구조를 가지는 삼각격자 자성체이다. 이론적으로 비선형 자기구조에서 마그논-포논 결합이나 마그논-마그논 상호작용 (magnon-magnon interaction) 이 일어날 것으로 예상된다. 이러한 연구에서 이미 마그논-포논 결합 및 마그논-마그논 상호작용에 의해 나타나는 여러 이상

현상들이 실험적으로 관측되었지만, 두 상호작용을 정량적으로 비교하는 데에 한계가 드러나고 있다.

본 학위논문의 첫 부분에서는 비탄성 중성자 산란 실험을 통하여 HoMnO_3 의 마그논 분산 관계를 측정하고, 이를 통해 마그논-포논 결합 및 마그논-마그논 상호작용에 기인하는 이상현상들을 관측한 연구를 다룬다. 또한 세 가지의 다른 이론적 모델을 이용하여 두 상호작용 중 어떤 부분이 더 영향을 주는지 규명한다. 간단한 선형 스핀파 이론으로 대부분의 마그논을 설명할 수 있지만, 마그논-포논 결합 모델을 이용한 계산으로 마그논 에너지 재규격화 현상과 마그논 분산관계를 완전히 이해할 수 있다. 특히, 측정되는 신호의 세기까지 일치하는 것으로 볼 때, 마그논-포논 결합이 HoMnO_3 에서 더 지배적인 것으로 판단된다.

마그논-포논 결합을 설명할 때에 흔히 쓰이는 메커니즘으로 exchange-striction 모델이 있다. 하지만 스핀-궤도 결합 (spin-orbit coupling) 이 강할 경우 다른 메커니즘으로 스핀-격자 결합이 나타날 수 있다. 5d 전이 금속 산화물 중의 하나인 $\text{Cd}_2\text{Os}_2\text{O}_7$ 에서 강한 자기 이방성으로 인해 나타나는 스핀-포논 결합 (spin-phonon coupling) 이 관측되었다. 광학적 분광법으로 측정한 포논에서 자기 상전이 전후로 포논의 에너지가 급격하게 변한다. 주요 메커니즘으로는 강한 스핀-궤도 결합으로 인해 나타나는 자기 이방성으로 확인되었다. 광학적 분광법은 포논 분산관계를 측정하는데 한계가 있으므로, $\text{Cd}_2\text{Os}_2\text{O}_7$ 의 스핀-포논 결합을 완전히 이해하는데 어려움이 존재한다.

본 학위논문의 두 번째 부분에서는 비탄성 엑스선 산란을 이용하여

$\text{Cd}_2\text{Os}_2\text{O}_7$ 의 포논을 넓은 운동량 및 에너지 공간에서 측정하여 분석한 내용을 다룬다. 또한 제일원리 이론을 통해 계산한 포논과 비교하여 스핀-궤도 결합에 따른 영향을 알아보았다. 제일원리 계산을 통해 얻은 포논들이 저온에서 측정된 포논과 일치하였음을 확인하였다. 그리고 스핀-궤도 결합의 세기를 이론적으로 조절함에 따라 실험적으로 관측된 포논의 온도 의존성을 설명할 수 있었다. 따라서 스핀-궤도 결합이 $\text{Cd}_2\text{Os}_2\text{O}_7$ 에 나타나는 스핀-포논 결합에서 중요한 요소임을 확인하였다.

주요어: 스핀-격자 결합, 마그논-포논 결합, 스핀-포논 결합, 비탄성 중성자 산란, 비탄성 엑스선 산란, 육방정계 망간 산화물, pyrochlore 산화물.

학 번: 2015-20325

Acknowledgement (감사의 글)

This thesis could not have been finished without all the helps and supports from many people. I would like to express my gratitude to supervisor Prof. Je-Geun Park. He taught me how to do research and gave me a deep insight to lead the projects. He also provided many opportunities for participating several beamline experiments and it was helpful to me to spread my experiences widely. I thank him for his confidence in me.

I would like to thank my scattering team leaders, Dr. Jonathan C. Leiner, Prof. Ki Hoon Lee, and Dr. Jaehong Jeong for their kind supports. They gave me a lot of practical comments on experiments as well as analysis. I would like to thank my thesis committees, Prof. Hongki Min, Yong-il Shin, Dohun Kim, and Pengcheng Dai for examining the thesis and giving me helpful advices.

The research projects explained in the thesis could be succeeded by kind supports from many collaborators. I would like to thank all of the scattering team members, Dr. Joosung Oh, Dr. Kiso Park, and Pyeongjae Park, who carried out experiments with me and helped the analysis. I would also thank Dr. Kazuki Iida, Dr. Kazuya Kamazawa, Dr. Alfred Q. R. Baron, and Dr. Daisuke Ishikawa for their efforts to complete the experiments at J-PARC and SPring-8. I also want to give my gratitude to Dr. Choong Hyun Kim for his insightful and theoretical comments. I would thank Dr. Hasung Sim and Prof. Zenji Hiroi for providing high quality of single crystals to enable me to do experiments successfully. I also thank collaborators for the Fe₃O₄ project, Dr. Soon Gu Kwon, Dr. Jisoo Lee, Dr. Sumin Lim, Jaeyoung Hong, Prof. Taeghwan Hyeon, Prof. Soonchil Lee, Z. Y. Chen, Dr. H. Y.

Acknowledgement

Huang, Dr. J. Okamoto, Prof. Di-Jing Huang, Dr. Midori A. Patino, Prof. Yuichi Shimakawa, and Prof. J. Paul Attfield.

The members of emergent phenomena group made me feel comfortable while I study in the lab. I especially thank Dr. Seokhwan Yun for his general comments on my works. I also thank former members, Dr. Manh Duc Le, Dr. Darren C. Peets, Dr. Dongjik Kim, Dr. C. I. Satish, Dr. T.-Y. Tan, Dr. Seongil Choi, Dr. Ki-Young Choi, Dr. Marie Kratochvílová, Dr. Haeri Kim, Dr. Matthew Coak, Dr. Arvind Yogi, Dr. Tirthankar Chakraborty, Dr. Kaixuan Zhang, Dr. Hwanbeom Cho, Dr. Soonmin Kang, Seyyoung Jun, Sungmin Lee, Inho Hwang, Jisung Kwon, Erika Beard, Nahyun Lee, Youngeun Shin, Kyung-Su Kim, Ha-Leem Kim, Seunghyun Park, and Sangwoo Sim for their generous helps. I would like to thank current members, Suhan Son, Youjin Lee, Chaebin Kim, Junghyun Kim, Heejun Yang, Gi-Ung Park, Jingyuan Cui, and Dr. Jaena Park, who encouraged me, shared discussions, and gave a lot of supports during Ph. D. course.

I could never have achieved the Ph.D. degree without my family's love and encouragement. I would like to express my gratitude to my parents who always support and love me. I would also like to thank my sisters for her respect and support.